# Three-dimensional Nanostructures Fabricated by Stacking Pre-patterned Monocrystalline Silicon Nanomembranes



by

Corey Patrick Fucetola

S.B. Mathematics
Massachusetts Institute of Technology, 2004

B.S. Electrical Engineering and Computer Science
Massachusetts Institute of Technology, 2005

M.Eng. Electrical Engineering and Computer Science
Massachusetts Institute of Technology, 2007

SUBMITTED TO THE DEPARTMENT OF ELECTRICAL ENGINEERING AND COMPUTER SCIENCE
IN PARTIAL FULFILLMENT OF THE REQUIREMENTS FOR THE DEGREE OF

DOCTOR OF PHILOSOPHY IN ELECTRICAL ENGINEERING

AT THE
MASSACHUSETTS INSTITUTE OF TECHNOLOGY

SEPTEMBER 2013



Signature of Author: _____
Department of Electrical Engineering and Computer Science
August 16, 2013

Certified By: _____
Henry I. Smith
Professor of Electrical Engineering
Thesis Supervisor

Accepted By: _____
Professor Leslie A. Kolodziejski
Chair, Committee on Graduate Students
Department of Electrical Engineering and Computer Science

[THIS PAGE IS INTENTIONALLY LEFT BLANK]

# Three-dimensional Nanostructures Fabricated by Stacking Pre-patterned Monocrystalline Silicon Nanomembranes

by

Corey Patrick Fucetola

Submitted to the Department of Electrical Engineering and Computer Science
on August 16, 2013 in Partial Fulfillment of the
Requirements for the Degree of Doctor of Philosophy in
Electrical Engineering

## ABSTRACT

This thesis considers the viability of nanomembrane handling and stacking approaches to enable the fabrication of three-dimensional (3D) nano-structured materials. Sequentially stacking previously-patterned membranes to build up 3D nanostructures, e.g. photonic crystals, is a powerful technique that decouples serial patterning processes from 3D assembly, allows the incorporation of photonic devices into the material and facilitates in-process error inspection.

A technique identified to address the fundamental problems with stacking disjoined membranes, i.e. those populated with photonic devices, using water-based approaches was an outgrowth of methods to fabricate, handle and stack their connected counterparts. Initially, connected nanomembranes patterned in a thin layer of silicon on glass were released in hydrofluoric acid where surface tension caused them to float flat. Their fragility inspired novel handling and position manipulation techniques for layer-to-layer alignment. While exploiting surface tension allowed membranes to be stacked using water, drifting precluded precision placement. Although carrier substrates held them stationary, the membranes leaked water before Van-der Waals adhesion was overcome. To address such issues a novel method is introduced whereby a sublimable glue affixes membranes to a glass carrier, which is placed membrane-side down onto a receiving substrate and the glue is vaporized to detach the membranes, leaving them bound to the previous layer.

Thesis Supervisor: Henry I. Smith
Professor of Electrical Engineering and Computer Science

# Acknowledgments

The opportunity to develop my intellectual and professional capabilities amidst such excellent students, staff, post docs and professors has been especially rewarding. Many of these, both within the Nanostructures Laboratory and beyond, provided insights and expertise in teaching, diagnosing and debugging the underlying fabrication processes described herein. It is not possible to express enough how helpful these interactions were nor how thankful I am for all of your help.

My supervisor, Professor Henry I. Smith, inspired me to forge ahead into uncharted technological territory with his persistence, guidance, meticulous excitement and seemingly limitless drive. Drs. Euclid Moon, Lin-lee Cheong, Shabnam Ghadarghadr, Annie Wang, Javier Bravo, Amil Patel as well as Hank's grandson Duncan Smith-Freedman and undergraduate student Fatih Akyurek were instrumental to this work. Finally, Mark Mondol, Jim Daley and Dr. Tim Savas kept the tools working, the lab clean and the processes possible through their dedication and availability. I am deeply grateful for the help and support each of you provided

The beliefs that no problem is unsolvable, that an optimistic outlook precludes solving seemingly insurmountable tasks and that the right perspective will simplify all of my endeavors were instilled within me by my parents. Their love and guidance has helped me tremendously. However, being a dependable friend, mentor, classmate, supervisor, supervisee, colleague and collaborator, my brother has played a more critical role in my professional development while we've been here at MIT. Elizabeth, you were right to tell me not to listen to Peggy as she's a terrible editor. You are my rock, my love, my life and my best friend, our life together beckons.

# Table of Contents

# List of Figures

# Chapter 1. Introduction

This thesis describes the development of technologies for fabricating three-dimensional (3D) structures with nanoscale features, based on the stacking of pre-patterned membranes. Nanoscale features are almost always made on a substrate using the planar fabrication process (i.e. lithography followed by pattern transfer into or onto the substrate). This process is extremely powerful; however, it is planar, thus extending it to create 3D nanostructures is problematic.

Some examples of periodic 3D nanostructures include 3D photonic crystals [1], meta-materials, 3D holograms and tissue scaffolding. Three-dimensional dielectric photonic crystals are the application of interest in this thesis. Figure 1.1 depicts a 3D photonic crystal structure that consists of alternating patterns of rods and holes along with the associated band diagram for the optimized structure. In addition to the structure shown in Figure 1.1, 3D photonic crystals can be populated with devices (e.g. waveguides, lasers and high-Q cavities). To create a waveguide, a row of rods or holes is removed from the periodic lattice. If they are removed, frequencies within the bandgap can then propagate along the series of altered features. Additional examples of photonic crystal devices are coupled-resonant optical waveguides [2], mode-locked lasers [3], and Q-switchable cavities [4]. Each of these devices benefits from the confinement attained in 3D photonic crystals.

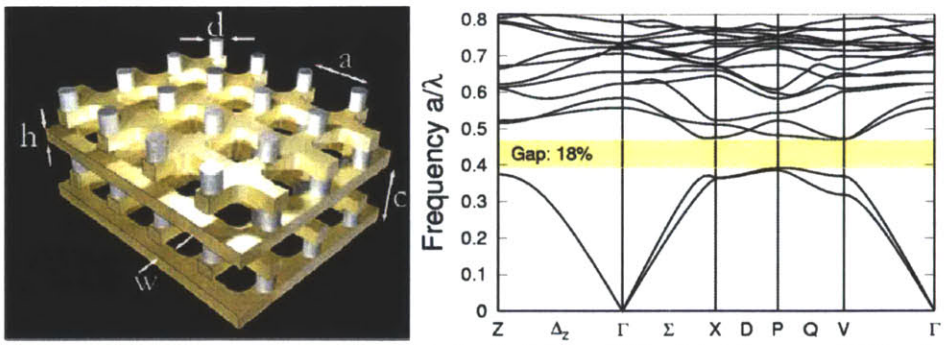


Figure 1.1 A three-dimensional photonic crystal (adapted from [5]). (a) 4 layers of this photonic crystal structure are shown, each of which consists of an array of holes and an array of rods of the same periodicity, 'a'. In each layer, the center of every rod is halfway between two of the four neighboring holes and successive layers are shifted by half a period in each direction. The relationships between 'a', 'c', 'd', 'h' and 'w' can be found in the reference - at a vacuum wavelength of $\lambda$=1550 nm the normalized frequency of $a/\lambda$=0.426 (see b) corresponds to dimensions: a = 660 nm, c = 700 nm, d = 194 nm, w = 158 nm, h = 161 nm (b) the dispersion diagram for the Brillouin zone shows the optical frequencies for which this silicon photonic crystal prohibits the propagation of incident light.

### a. **Approaches for fabricating 3D periodic nanostructures**

The fabrication process to make 3D nanostructures should allow for device integration, error inspection and scalability to large-area substrates. Various processes exist that have successfully yielded 3D nanostructures for specific applications. Generally, these approaches can be broadly classified as *"element-by-element, "all-in-one"* and *"layer-by-layer."* Examples of the *element-by-element* approach can be found in [5], [6] and [7]. Examples of the *all-in-one* approach can be found in [8], [9], [10], [11], [12], [13], [14], [15] and [16]. Examples of the *layer-by-layer* approach can be found in [17] and [18].

While these various approaches to 3D fabrication are exciting in their own right, each faces serious shortcomings. The *element-by-element* approaches are accurate but time-consuming and thus are difficult to scale to large areas. These approaches need to be "parallelized" in order to become practical. The *all-in-one* approaches are fast and can pattern large areas but the structures are prone to placement errors, substantially

limited in the out-of-plane direction and challenged by inspection of the bulk material. These approaches are limited in the overall thickness of the structures made and their ability to incorporate non-periodic structures. The *layer-by-layer* approach, which leverages existing planar-fabrication technologies, can incorporate devices, allow for error inspection during fabrication of each layer and be scaled to large-area substrates. It also requires precise alignment of individual layers and depends on the yield of every fabrication step. These approaches are limited by the serial nature of the planar-fabrication process. Conceivably, future 3D nanostructures could require hundreds to even thousands of layers. None of the approaches discussed so far addresses this requirement.

The main problem with the planar-fabrication process is that each fabrication step depends on the steps before it. As an example, if each round of planar fabrication had 99.3% yield and produced one layer of a 3D structure, then a 100-layer structure would be successfully fabricated 50% of the time. Consider instead, if the layers were fabricated and inspected individually so defective ones could be discarded prior to assembly, then perhaps the 3D nanostructure yield would be improved. This is a major advantage of and a driving force for pursuing the nanomembrane stacking paradigm described in this thesis.

b. **The nanomembrane-stacking paradigm**

The nanomembrane-stacking paradigm includes the fabrication of nanomembranes as well as approaches to control, manipulate and stack them. The planar-fabrication process can be used to pattern thin membranes but afterwards no

general process exists to assemble them into more complex structures. While the so-called "transfer-printing" process described in the techniques of [19], [20], [21], [22], [23] and [24] allows single nanomembranes to be held by (and deposited onto) host substrates it does not readily extend to stacking multiple membrane layers because the membrane's adhesion to the receiving substrate depends on its adhesion to the carrier substrate and detachment from the carrier can leave behind contaminants on the membrane.

There is no fundamental reason that nanomembranes cannot be stacked. In our group's first effort, free-standing silicon nitride nanomembranes that were tethered to a frame, were stacked [25]. The silicon nitride, with a photonic crystal pattern surrounded by a perforated edge of tethers, was released from the handle silicon by submersion in potassium hydroxide. The resulting tethered 1 $cm^2$ membranes were inspected in an optical microscope for defects so that any defective membranes could be ignored. Figure 1.2 depicts how to stack them to form the 3D structure: the entire free-standing silicon nitride membrane was brought down into contact to a mesa where it was Van-der Waals bonded. Once bonded, the membrane was separated from its accompanying frame by detaching it along the tethers. Then the next membrane was brought into contact and the process repeated.

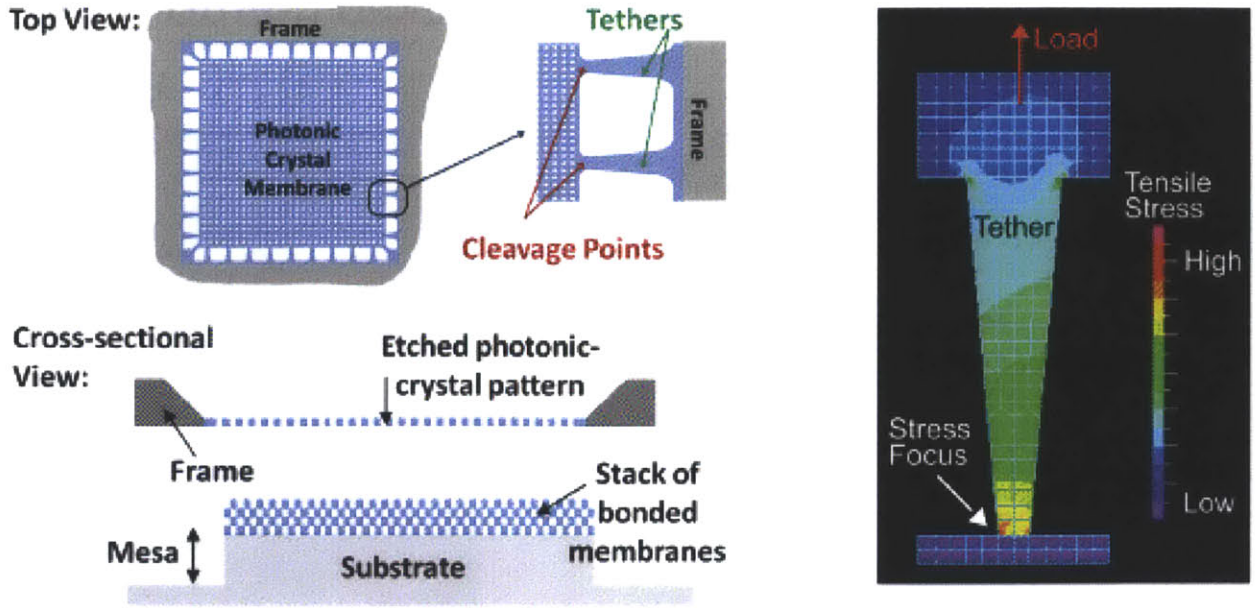


(a) (b)

Figure 1.2 The fabrication process to create silicon nitride photonic crystals (from [25]). (a) Illustrates two views of the free-standing silicon nitride membranes fabricated in [25]. Top-view: the free-standing membrane is supported by tethers to a frame of silicon nitride on un-etched silicon. Cross-section: the membrane is being brought down to a stack of previously detached membranes. (b) Illustrates the distribution of stress in a single tether within the perforated edge. As the membrane is contacted to the stack beneath and the frame is lowered further, the tethers stretch until they break at the stress focus

Silicon has larger refractive-index contrast than silicon nitride and air making it a more desirable dielectric for photonic crystals operating at telecomm wavelengths, however it is non-trivial to combine the approaches of [21], [22], [24] and [25] to enable stacking of single-crystal silicon membranes. This thesis describes the development of processes to stack silicon membranes patterned with nanostructured features, a.k.a. nanomembranes. As illustrated in Figure 1.3, nanomembranes that are either fully connected or composed of disjoined sections may ultimately need to be stacked up to realize photonic crystal devices.

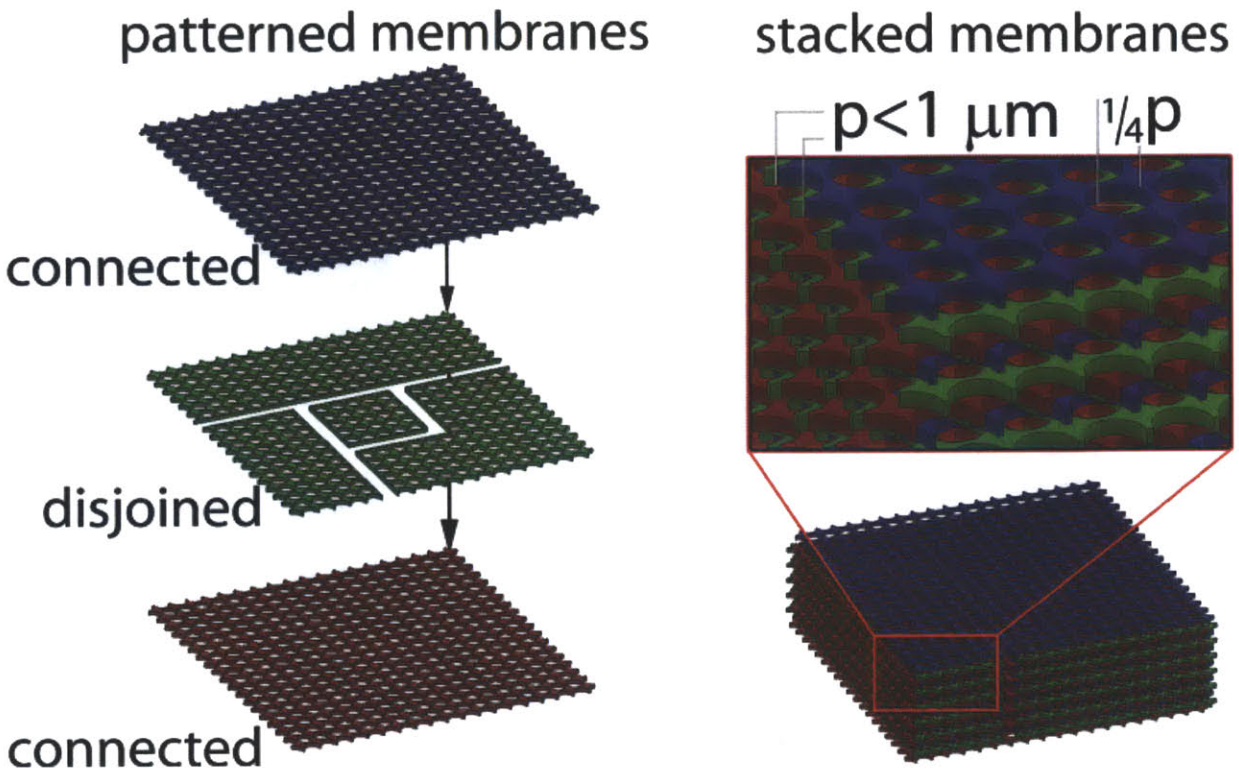


Figure 1.3 Stacking in the case of disjoined membranes. Clearly, stacking disjoined membranes presents a unique challenge. If the membranes were supported on an underlying carrier many issues could be circumvented.

A candidate process to stack disjoined membranes is presented in Figure 1.4 and Figure 1.5. Illustrated in Figure 1.4, bulk Si is bonded to a thin flex glass substrate using a special vaporizable bonding agent. Once bonded, the Si or other material would be thinned down to the requisite membrane thickness by any of several standard techniques (e.g. grinding & polishing, wet or dry etching, etc.). Then the plain membrane and flex glass would be patterned with the planar-fabrication process to include the disjoined patterns and relevant alignment marks.

As depicted in Figure 1.5, once patterned, the disjoined membrane and flex glass would be loaded onto a rigid glass carrier. Interferometric alignment [26] of the flex glass to the receiving substrate would be followed by intimate contact between the

membrane and underlying membrane stack achieved by bulging out the flex glass using air pressure. After intimate contact formed, the bonding agent would be sublimated eliminating the adhesion between the membrane and the flex glass.

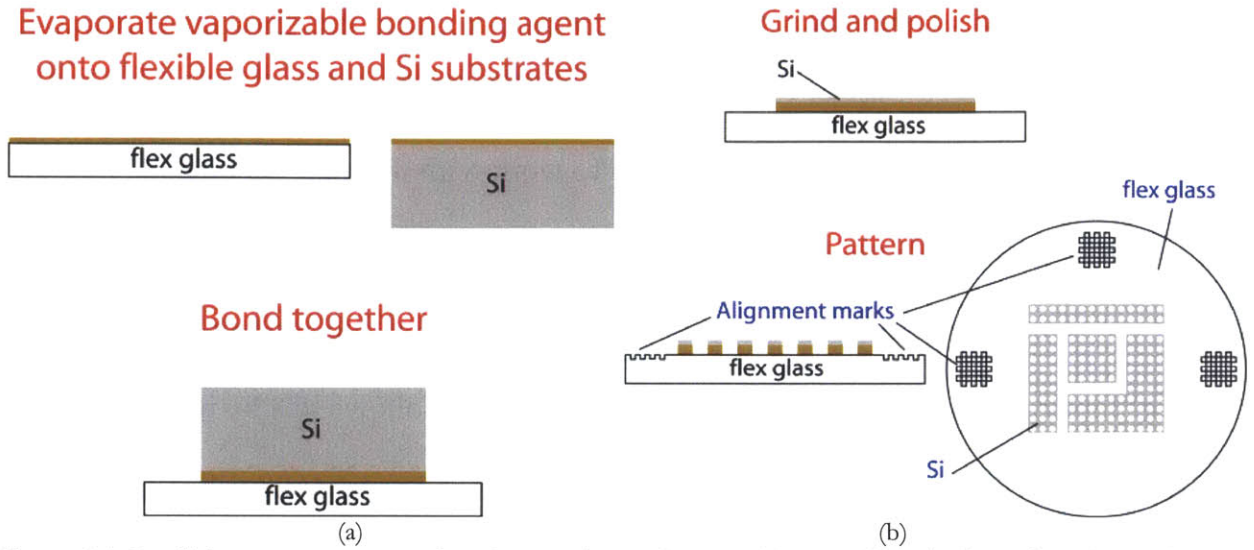


Figure 1.4 Candidate process to stack a disjoined membrane. (a) Initially a bulk wafer, shown here as silicon, is bonded to the flex glass with a special vaporizable bonding agent. (b) After the bulk wafer is thinned to form a membrane it is patterned along with the requisite alignment marks. The disjoined membrane is now completely supported by the vaporizable bonding agent.

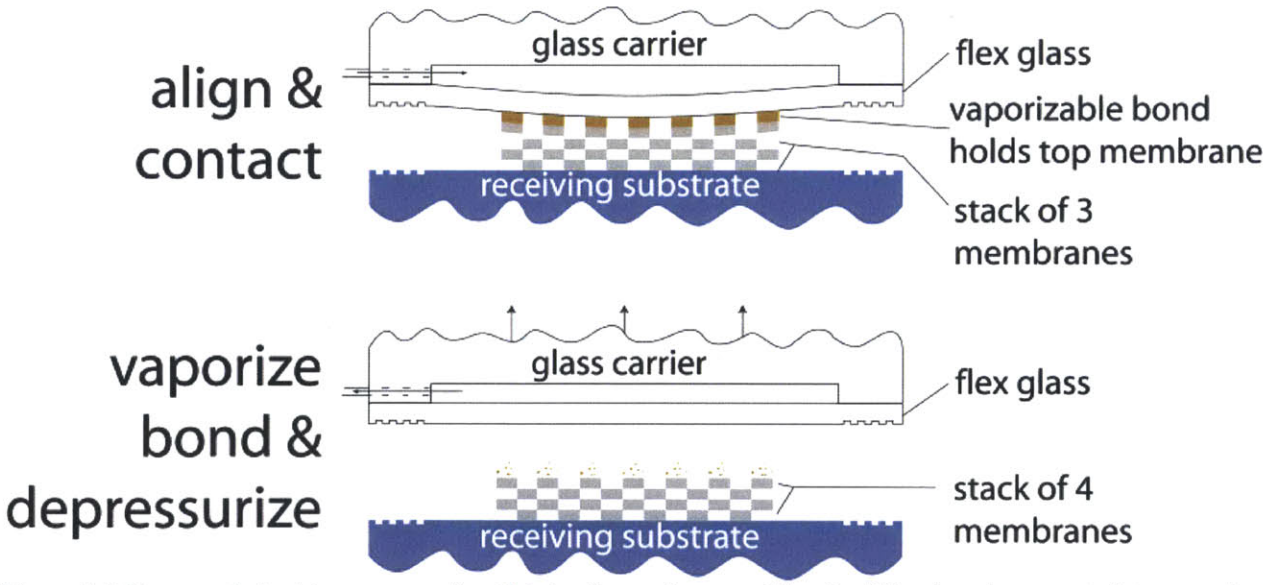


Figure 1.5 Proposed stacking process for disjoined-membranes. The flexible glass is mounted to a carrier and after it is aligned to the receiving substrate the flexible glass is bulged to contact the membrane to the underlying stack of membranes on the receiving substrate. Once in intimate contact, the bond is sublimated to eliminate the membrane's adhesion to the flex glass.

While this process grew out of this research it remains largely a topic for future work. One of its virtues is that none of the requisite steps are limited by existing technologies. However combining the steps would require more research. The conclusion of Chapter 4 presents some initial work resulting from a shortcut to this process that highlights a class of candidate adhesive materials and then Chapter 6 revisits these in the context of extending them to work with this new scheme.

Included in this thesis are methods to fabricate, manipulate, handle, control and stack ~1-cm-diameter connected silicon nanomembranes atop one another. Chapter 2 addresses fabrication of patterned membranes. Chapter 3 follows this by introducing methods to manipulate, handle and control membranes. Chapter 4 describes several membrane stacking approaches along with their limitations. Chapter 5 describes alignment techniques that should allow precision placement during stacking. Chapter 6 analyzes the fabrication and stacking approaches of Chapters 2-4 to explain their limitations, summarizes contributions to the field and identifies key improvements that would extend the current methodology. The bulk of this research focused on water-based stacking, and though not applicable to disjoined membrane stacking, many insights described herein informed the subsequent research that led to a viable stacking process.

# Chapter 2. Membrane Fabrication

Prior to releasing membranes, substrates were prepared through a number of fabrication steps. The simplest membrane fabrication process flow is in Figure 2.1 wherein the initial substrate is patterned to create the photonic structures and define the membrane shape after which the membrane is released.

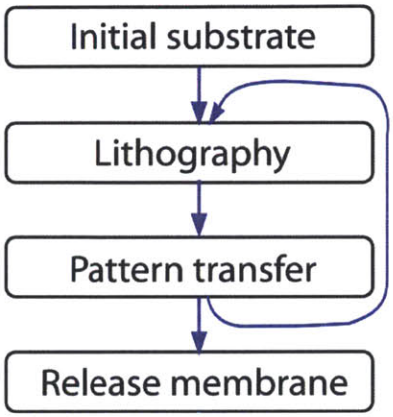


Figure 2.1 A process flow to release a membrane. Initial substrates undergo repeated planar fabrication steps to define the photonic structure and the shape of the photonic regions. After patterns are transferred into the initial substrate the membranes are released.

Similar to the approach in [25], but following the process flow in Figure 2.1, with SOI wafers instead of LPCVD $SiN_x$, free-standing silicon membranes were released by undercutting the top silicon layer of the SOI wafer with hydrofluoric acid. Sparing some details, several 1 $cm^2$ ~660-nm-pitch square grids of holes recorded into negative photoresist on an SOI wafer were transferred into the top silicon layer with reactive-ion-etching. These 1 $cm^2$ grids in silicon were surrounded by a *frame* of un-patterned silicon and the holes allowed in vapor-phase HF to release the patterned silicon from the buried $SiO_2$. Unfortunately, as shown in Figure 2.2 compressive stress in the top layer from the buried $SiO_2$ is relieved during the HF release causing the membranes to buckle. Clearly the process needed to be changed to eliminate these ripples.

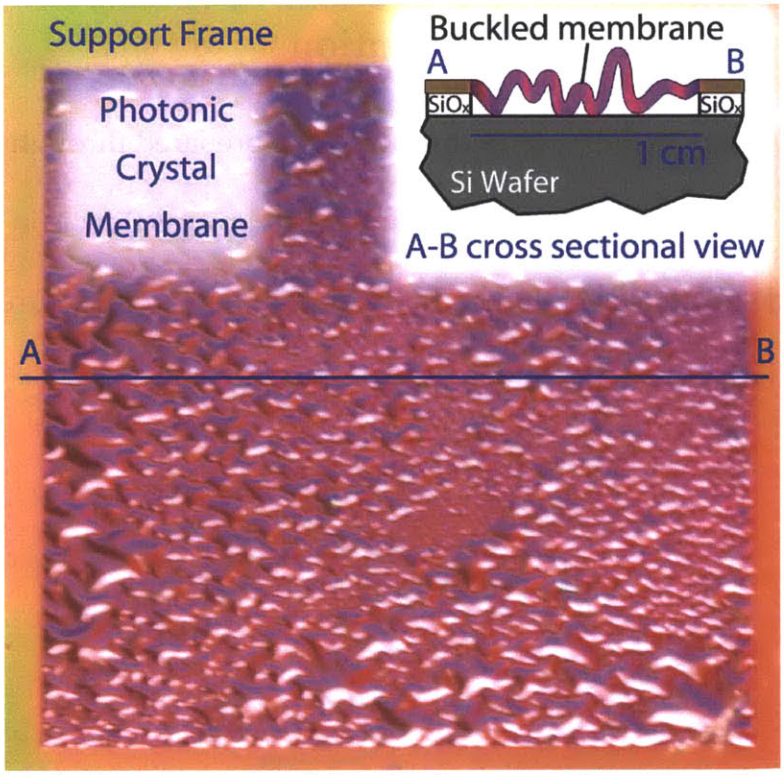


Figure 2.2 Buckled 1 cm² silicon membranes following the process from Figure 2.1. Each membrane is patterned with an array of holes on a 660 nm-pitch and is surrounded by a region of the un-patterned silicon device layer that constrains them around the edges. Light scattered from the patterned silicon highlights buckles that resulted from compressive stress relieved after the membrane released.

In another approach, instead of constraining the membranes by a frame of un-patterned silicon, the entire SOI wafer was patterned with a grid, cleaved into smaller samples and submerged into HF to release the patterned device layer into the HF. This was also unsuccessful because the device layer would settle onto the handle silicon where it remained attached, despite several attempts to get it to detach. While submerged, both HF and water were flowed across the surface in an attempt to peel it off the handle. Also, the sample was brought to the surface of the HF and surface tension was investigated as a means to detach the two, also to no avail. Since solvents wet the silicon, a sample was removed from HF, allowed to dry and submersed in isopropanol. Neither flowing isopropanol along the surface nor peeling with surface

tension had any effect; scotch tape would remove them but getting rid of the tape without damaging the membranes was problematic.

Clearly, the silicon membrane needs to release fully without adhering to the underlying handle, so a slight modification was made to the process flow. If, as illustrated in Figure 2.3, the membranes were attached to a glass substrate instead of a silicon handle wafer, then etching would proceed until the membrane detached from the glass.

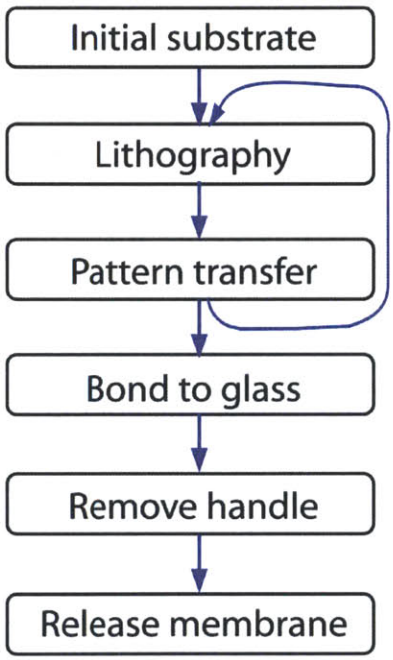


Figure 2.3 A more general process flow to fabricate and release membranes. Starting substrates (either silicon or SOI wafers) were patterned following the planar-fabrication process and then anodically bonded to a glass substrate. Then the silicon is thinned down to the desired thickness, either by grinding and polishing or by wet etching to remove the excess handle silicon. Finally, the silicon is released from the glass to form a membrane.

In this chapter initial substrates are considered, followed by lithographic methods and pattern transfer processes. Finally the fabrication process for making membranes is described in more detail.

a. **Starting substrate selection**

Two types of substrates were examined: silicon wafers and SOI wafers. SOI substrates were produced commercially by SOITEC with their so-called Smart-Cut™ process. While the thickness uniformity of the SOI substrates is desirable, during the Smart-Cut™ manufacturing process the oxide interlayer is reflow-bonded at ~1000°C [27], which, upon cooling, causes compressive stress in the (typically) 350-nm-thick top silicon layer. After release, stress leads to distorted patterns and large-scale buckling. In contrast, a silicon wafer that is first patterned and *then* bonded at ~400°C doesn't suffer this shortcoming, but grinding and polishing to the desired thickness presents additional challenges.

As a part of this thesis, a grinding and polishing apparatus was built to explore using silicon as the initial substrate – see Figure 2.4. This apparatus combined a grinding wheel (Buehler MetaServ® 250) on the bottom with a custom-built rotating wafer chuck. The rotating wafer chuck was composed of several stages designed to reduce thickness variation across the sample. The fluid delivery system supported two polycrystalline diamond suspensions (9 μm and 3 μm) and a non-crystallizing fused silica (20 nm) suspension that would drip onto the grinding wheel during polishing steps.

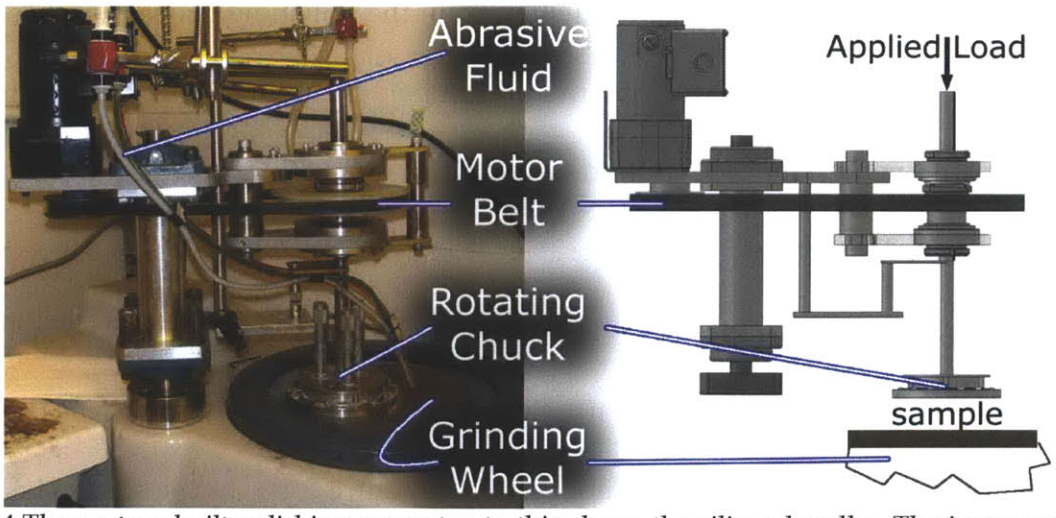


Figure 2.4 The custom-built polishing apparatus to thin down the silicon handle. The image on the left illustrates the apparatus, which is paired with its design on the right. The fluids used during polishing consisted of 9 μm, 3 μm and 20 nm slurries and propylene glycol lubricant. The motor belt drove the rotating chuck where the sample was mounted. Thus the sample was rotated, either with or against the grinding wheel. The wafer chuck was constrained by two tapered rotation bearings, but allowed to translate along the axis of rotation, where an applied load controlled grinding rates.

The process flow in Figure 2.3 was shortened initially to include only the anodic bonding and silicon removal steps. Then, to characterize the grinding and polishing process, samples were loaded into the polisher, ground and then polished until the silicon became transparent under fiber light illumination. The bonding process was carried out between 370 °C and 430 °C, where 1.6kV applied across the glass and silicon drove $Na^+$ to electrons at the silicon–glass interface. After 120s, the silicon and glass were bonded together and the silicon was ready to be ground and polished.

To grind the silicon, the silicon-on-glass substrate needed to be affixed onto the wafer chuck. To do so, the substrate was placed onto a hotplate above 70 °C where a pinkish-colored wax, Unibond 5.0 (from Universal Photonics), was melted on the glass. Then, the substrate and liquid-phase wax were placed onto the grinding wheel beneath the wafer chuck and the chuck was brought into contact with the wax, cooling it and affixing the wafer to the chuck, after which point the grinding process commenced.

The grinding process was distinguished from the polishing process in three ways. First, the abrasive was either 35 μm or 8 μm polycrystalline grains that were glued to grinding pads (Apex® Diamond Grinding Discs, Buehler), second, the working fluid is either a coolant (tap water) or lubricant (MetaDi® fluid, Buehler; aka. propylene glycol) and third a load was applied to the rotation axis of the wafer chuck[1]. Each step of the grinding process was timed and upon completion, the wafer chuck was lifted and swung into position over a fiber light (not shown in Figure 2.4). As the silicon became thinner, more light passed through the silicon and this was used to gauge the process. Given the absorption of silicon, transmission of red light became visible first, and as the silicon became thinner, shorter wavelengths also became visible. Once the silicon became sufficiently thin, it was polished.

In the polishing process, polycrystalline diamond suspensions dripped onto their respective polishing pads as the wafer was polished smooth. The process consisted of a sequence of steps from coarsest to finest grain suspension, which was repeated until the surface was smooth. In each step, as the MetaServ® 250 platen rotates, a suspension (MetaDi® Supreme Diamond Suspensions or MasterMet® 20 nm non-crystallizing fused silica suspension, Buehler) dripped from its fluid line onto the polishing pad, (Satyn MB for 9 μm and 3 μm and Chemia MB for 0.02 μm suspensions). Throughout every step, the flow rate of each suspension was set upstream by metering valves and remained

[1]The distance from the lever pivot to the axis was fixed at 12.5 cm leading to a load multiplier of 2.4 for the 1 kg, 2 kg or 3 kg weights hung at the end of the lever.

fixed throughout. As the silicon became smoother, obliquely incident light was used to identify scratches in the surface.

After a bit of trial and error by a visiting research scientist, Javier Bravo, several challenges to grinding and polishing the silicon layer to micrometer thickness became apparent. If the silicon thickness uniformity is critical, then the axis of rotation of the silicon needs to be parallel to the axis of rotation for the grinding wheel. Furthermore, the flatness and wobble of the grinding wheel should be less than the thickness of the silicon, which was difficult to achieve with 0.005" machine-shop tolerances (after correcting the wobble by placing shim stock between the platen and spindle, we measured the wobble of the platen with respect to a granite slab to be 0.0001"). Finally, the glass is not perfect and chucking it to the wafer holder doesn't guarantee that the silicon–glass interface is parallel to the grinding wheel. As a result of these nuances, the wafer chuck evolved several times to include: a micrometer tip-tilt stage, a self-adjusting flexure mount and a single-point pressure plate. Each stage was developed as needed to improve the thickness uniformity of the silicon device layers after polishing. After grinding without any of the stages the residual silicon on the glass handle would be asymmetric and off-center. With the tip-tilt stage included the residual silicon became centered and including the flexure mount acted to make the residue circular. The point-pressure mount could reduce the thickness variation of the silicon residue but remains as future work.

With the tip-tilt and flexure stages included, the process was further refined by a summer research student, Fatih Akyurek. He ground samples until red wavelengths

began transmitting through and then would polish them until the surface did not scatter fiber light.

In his work, grinding was done using either the 35-μm- or 8-μm-abrasive polycrystalline diamond discs, with the arm rotation either opposed, (+), to the rotation direction of the platen or along it, (-). The (-) direction was the predominant choice as it led to slower removal rates and less chipping of the edges, though the (+) direction was used a few times to remove material during the 35 μm steps. Once light transmitted though the silicon, polishing steps using 9 μm, 3 μm to 20 nm grit sizes were repeated.

Table 2.1 explains the parameters for the process steps we developed including the grit size, platen pad type, duration, wafer-chuck speed, platen speed and applied load for the most frequently chosen (aka 'best') configuration. Included are the related statistics, including the number, #, of times the step was carried out and the mean, μ, and standard deviation, σ, values for the related parameter.

After each step, the applied load was removed; the wafer chuck was lifted away from the platen and was then swung around to the fiber light for inspection. Step by step, as the silicon was ground thinner, the area of the silicon became smaller and more wavelengths transmitted through it. Eventually, upon illumination, the light reflecting from the Unibond wax that was covered by silicon looked the same pinkish color as light reflecting from the Unibond that was not covered by silicon and this was the point when the polishing process commenced. After each sequence of polishing steps, the surface was again illuminated, but this time the fiber light was incident at an oblique angle, to expose surface scratches in the silicon. Once the scratches were no longer

visible, the sample was removed from the wafer chuck and examined in sunlight, under a microscope and with the dektak profilometer. By repeating this polishing sequence Fatih produced a silicon layer approximately 5 um thick and 1" diameter.

| Step* | Abrasive P/N | Platen Pad P/N | Time (min) best #, (μ, σ) | Wafer-chuck Speed (%) best (μ, σ) | Platen Speed (rpm) best (μ, σ) | Applied Load (kg) best (μ, σ) |
|---|---|---|---|---|---|---|
| **Grind (+)** | 35 μm | Apex® 41-3708 | **40** 3, (42, 3) | **100** (100, 0) | **500** (500, 0) | **3** (3, 0) |
| **Grind (-)** | 35 μm | Apex® 41-3708 | **10** 32, (11, 16) | **30** (42.2, 31.4) | **500** (404, 133) | **2** (2.06, 1.18) |
| **Grind (-)** | 8 μm | Apex® 41-3908 | **5** 16, (9, 11) | **20** (21.3, 3.4) | **300** (315, 81) | **2** (2.18, 0.4) |
| **Polish (-)** | 9 μm 40-6633 | Satyn MB 41-10038 | **30** 29, (23, 26) | **30** (53.1, 34.8) | **300** (241, 117) | **3** (2.3, 0.97) |
| **Polish (-)** | 3 μm 40-6631 | Satyn MB 41-10038 | **60** 21, (43, 18) | **30** (36.2, 21.3) | **150** (190, 85) | **1** (1.3, 1.39) |
| **Polish (-)** | 20 nm 40-6380 | Chemia MB 41-10032 | **60** 69, (26, 24) | **30** (49.5, 33.8) | **150** (208, 91) | **0** (1.7, 1.26) |

Table 2.1 Parameters for the grinding and polishing process. Over the course of Fatih's work, different process parameter configurations were explored to grind and polish a 76.2 mm silicon wafer from 375 μm ± 25 μm thick to roughly 5 μm thick. The process is not well-defined and as a result, average values are tabulated. * The '(+)' or forward direction of rotation was opposite the direction of the MetaServ® platen and resulted in faster grinding rates; the '(-)' direction was used when slower removal rates were desired

Moreover, during the anodic bonding step, some regions of the substrates did not successfully bond and the air bubbles trapped between the silicon and glass tended to break through the silicon during the grinding step. These holes in the silicon were the locations where dektak measurements were carried out. Fatih explored the removal rate of the silicon for a sequence of 3 μm followed by 20 nm grit polishing steps on two different samples. For this, each step of the sequence was performed for 60 minutes intervals at 150 rpm platen speed, 30% (-) wafer chuck speed and no applied load. For each sequence the removal rate ranged between 0.169 μm to 1.26 μm per interval; for each sample, by measuring each step, he was able to produce silicon that was 1.36-μm

and 1.41-μm thick. It is possible that some of the glass was removed during polishing which would make the silicon even thinner than measured by the dektak.

Silicon thinned with this apparatus was thicker in the center than it was at the edges. While improvement of the thickness uniformity should be possible with the point-pressure mount (or acquisition of a suitable flat-lapping machine) the idea of thinning the silicon to micron-scale layer thickness was demonstrated. However, it was deemed more expedient to produce membranes of a uniform thickness from SOI wafers than optimize the grinding/polishing processes to produce the same.

b. **SOI substrate preparation, patterning and pattern transfer processes**

This section describes the planar fabrication steps that lead up to bonding the SOI substrates to glass. Explicitly, from Figure 2.3, these steps include lithography and pattern transfer. The lithography process drives both the substrate preparation and subsequent pattern transfer steps and so it is important to decide which lithographic process to use. One requirement for the process is that it be capable of printing large-area coherent patterns, consequently, contact printing or interference lithography (IL) were obvious candidates. It was more reliable to create large-area photonic structures using IL [28] because it readily creates large-area, spatially-coherent patterns without the use of a mask.

IL records periodic patterns into photoresist. These periodic patterns are generated by the interference of (at least) two beams of coherent light, which cause a standing wave to be recorded into photoresist. Theoretically, the period, $p$, of the

standing wave in the plane of the resist depends on the incident angle, $\theta$, and wavelength, $\lambda$, of the light in accordance with equation 1.

$$p = \frac{\lambda}{2 \sin \theta} \tag{1}$$

The standing-wave pattern recorded by the resist is complicated by the back-reflectance into the resist from the underlying materials, which can cause vertical standing waves up the resist wall that ultimately affects subsequent pattern transfer steps. In this work, the method described in [29] is chosen to minimize the vertical standing-wave during the IL steps. The essence of the process described in [29] is to insert films beneath the photoresist that minimize the back-reflectance into the photoresist and enable robust pattern transfer into the silicon membrane layer. The back-reflectance is minimized with an anti-reflection coating (ARC) of a designed thickness. Then, etch-stop layers of silicon oxide ($SiO_x$) are incorporated beneath the photoresist and beneath the ARC to improve the pattern transfer from the resist into the silicon. The individual film thicknesses were determined by the lithographic and pattern transfer process requirements and are specified in the appendix on fabrication.

In what follows are the process steps used to prepare samples for lithography, expose them to record periodic patterns in a layer of photoresist and transfer the patterns from the resist into the silicon membrane layer. The process parameters, e.g. film thicknesses; exposure wavelength, pitch, dose and reactive-ion etch times are left for the appendix.

### i Preparation for lithography

The first layer of the stack of films on top of the SOI wafer was either a spin-on glass (Dow Corning FOX-25) or evaporated $SiO_x$. FOX-25 was used if the process required a thick oxide layer: it was spun (typically thicker than 100 nm) and then annealed at 950 °C for 60 seconds in the rapid thermal processor (RTP). In most processes however 100 nm of evaporated $SiO_x$ was sufficient.

The second layer of the stack, an ARC (AZ Electronic Materials, Barli), was spun on top of the oxide and baked at 175 °C typically for 30 minutes in the oven (although on the hotplate 90 seconds at 175 °C worked equally well for process monitor wafers).

The third layer of the stack was evaporated $SiO_x$, which is hydrophilic. The various types of photoresist used throughout are hydrophobic, so an adhesion promoter Hexamethyldisilazane (HMDS) was applied prior to spinning the photoresist to help it adhere to the evaporated $SiO_x$. While there is no definite process for spinning HMDS (it is supposed to be deposited from a vapor phase) dripping it onto the wafer, waiting a minute, then spinning the wafer for 5 seconds worked, provided the spin bowl is cleaned of any residual HMDS prior to spinning the photoresist.

After application of HMDS, either a negative-tone resist (Ohka THMR-iN Chemically Amplified Resist, PS4) or a positive-tone resist (Sumitomo I-line DNQ Novolac Resist, PFI-88) was spun typically 180-nm-thick on top of the HMDS and baked at 90°C for 30 minutes in the oven.

Shipley 1813 (Rohm & Haas Electronic Materials, Microposit™ S1813™) photoresist was used when contact-printing large (~mm scale or larger) features, e.g.

when defining the membrane areas. This resist is also DNQ-Novolac resist that was baked at 110 °C for 90 seconds on the hotplate.

**ii Patterning**

A single interference lithography 'step' refers to the pattern that is recorded: a grating pattern results from a single exposure whereas a grid pattern requires at least two exposures. If the photoresist was PS4, then after lithography the sample underwent a post exposure bake at 110 °C for 30 minutes in the oven. This was unnecessary for a sample coated with PFI-88, which is not chemically amplified like PS4. After being exposed (and optionally, post-exposure baked), the samples that had PS4 or PFI-88 were developed by immersion into a 2.4% wt tetramethylammonium hydroxide (TMAH) solution (Rohm & Haas Electronic Materials, CD-26) followed by de-ionized water and a spin-dry step. For exposed Shipley 1813, development with MF321 (Rohm & Haas Electronic Materials, Microposit™, MIF 321) was followed by a de-ionized water rinse and a spin-dry step. Throughout, the development time remained fixed at 1 minute while the exposure dose was determined from monitor wafers.

**iii Pattern Transfer**

The pattern transfer process is fairly robust and involves reactive-ion etching (RIE) through the top $SiO_x$, ARC, bottom $SiO_x$ and into the silicon. The chamber was pumped down to an initial pressure of $10^{-5}$ Torr. After the base pressure was reached, the plasma was sparked at 20 mTorr for 5 s and then the pressure was reduced to 10 mTorr for the rest of the etch step. $SiO_x$ and FOX-25 were etched with 20 sccm $CHF_3$ at

a bias of 200 V (~0.25 nm/s) and ARC was etched in a mixture of 16 sccm Helium and 8 sccm $O_2$ gases at a bias of 250 V (~1nm/s).

Reactive-ion etching through the silicon layer was carried out in an HBr plasma in which bias voltage was controlled to maintain the directionality of the ionic species. The chamber was pumped to an initial pressure of $5x10^{-6}$ Torr and the HBr was flowed into the chamber at 20 sccm for 300 s. It was determined experimentally that this led to more repeatable etch rates though a scientific explanation of why it was necessary to flow the HBr gas remains unclear. Following this, the plasma was sparked at 20 mTorr and the pressure was typically reduced to either 2 mTorr or 10 mTorr for the remainder of the etch step. At 40 W and a bias of ~180 V, the silicon layer etched at ~0.15 nm/s with pressure set at 2 mTorr and ~0.26 nm/s with pressure set at 10 mTorr, whereas at 200 W and a bias of ~600 V the silicon layer etched at ~1 nm/s.

c. **Fabrication of photonic structures**

There are several photonic crystal structures that could be created in three dimensions. From the membrane stacking perspective these multi-layer structures may require some membrane layers to be patterned with at most one lithography step (i.e. a grid pattern of holes etched into the membrane). Alternatively, some layers may require at least two lithography steps which could lead to disjoined membrane layers (i.e. a grid pattern of holes that is cut by a waveguide) and/or partially connected membrane layers (i.e. a grid pattern of holes through the membrane with a superimposed grid pattern of rods partially etched into the silicon - see Figure 2.5). In the spirit of brevity, the fabrication recipes for these are deferred to Chapter 6.a.

### i The Roundy Structure: rods and holes

From a stacking viewpoint, the structure in Figure 1.1 can be broken into four membrane layers one of which is illustrated in Figure 2.5. Each layer has both a pattern of holes and a pattern of rods thus requiring two lithography steps. The first step would record a periodic array of holes into PS4, which would then be transferred into the silicon with RIE and the second step would record a periodic array of rods into PFI-88, which would also be transferred into the silicon with RIE.

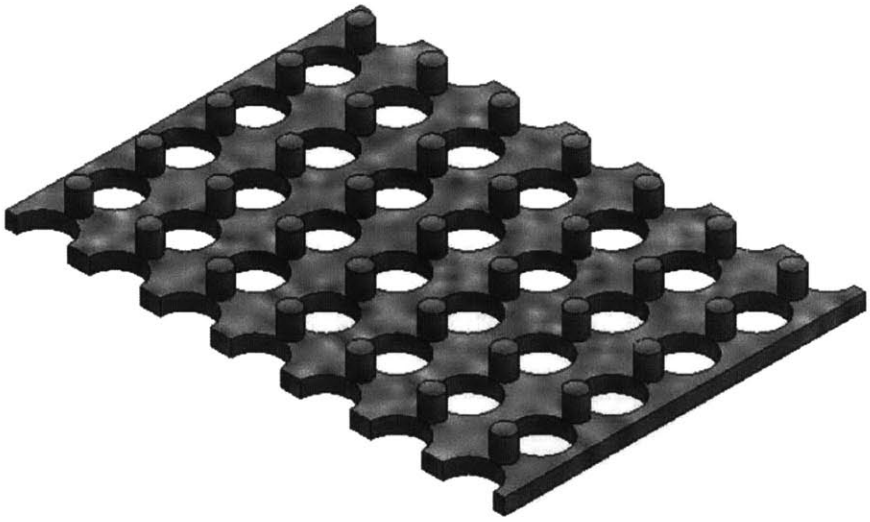

Figure 2.5 A single layer of the photonic structure shown in Figure 1.1. Within a given layer there are an array of rods and an array of holes requiring at least two separate lithography steps. The rods form a structure that is connected together by the underlying grid of holes.

The Lloyd's mirror interferometric lithography tool [28] was chosen for this demonstration because the in-plane period is fairly repeatable and it is robust to vibrations (it can even be made as a table top version [30]). The rigidly connected substrate and mirror surfaces are orthogonal and the axis defined by their intersection is perpendicular to the optical axis of the spatially-filtered 325-nm illumination system and aligned to the polarization of the incident laser light. One beam of light illuminates

both the mirror and the substrate and the beam redirected from the mirror creates stationary interference fringes on the substrate. Furthermore, by loading a pre-patterned grating into the tool and rotating the mirror-substrate chuck, a fringe pattern can be seen on a screen placed back at the spatial filter. Carefully rotating the chuck to minimize the number of fringes brings the stage rotation - and hence periodicity - into alignment for the second lithography step.

Figure 2.6 shows the photoresist stack design for the first lithography step to create a layer of holes in PS4 (recipe is deferred to the Appendix Table 6.3). On the left of the figure is a diagram of the film stack that corresponds to the graph on the right of the transmittance through the resist (upper curve) and back reflectance (lower curve) into the resist as a function of ARC thickness - at 250 nm the back-reflectance is 0.1%. A FDTD of the standing-wave intensity in the resist is overlaid onto the layer of PS4.

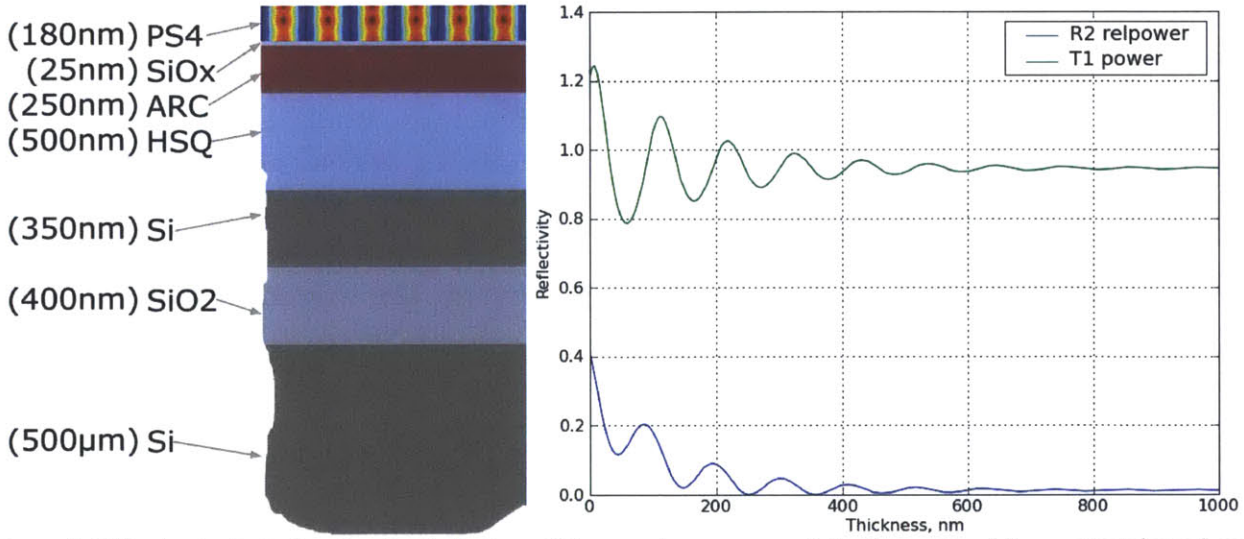


Figure 2.6 Photostack design for the hole-layer lithography process. (a) schematic of the material stack as designed for IL. Overlaid on the layer of PS4 is the intensity calculated for the film stack described in the figure. That the vertical standing-wave is negligible at this thickness of Barli is confirmed by plot of reflectivity in part (b), which has a reflectivity of 0.1%.

After patterning and pattern transfer processes the samples were cleaned in piranha and prepared for the second lithography step to produce the rods pattern. The stack design for this step is shown in Figure 2.7; again the recipe is deferred to Table 6.4. Notably, ARC was spun (and baked) twice to planarize the surface above the patterned FOX-25 layer for lithography. The $SiO_x$ interlayer was evaporated followed by application of HMDS and positive-tone PFI-88.

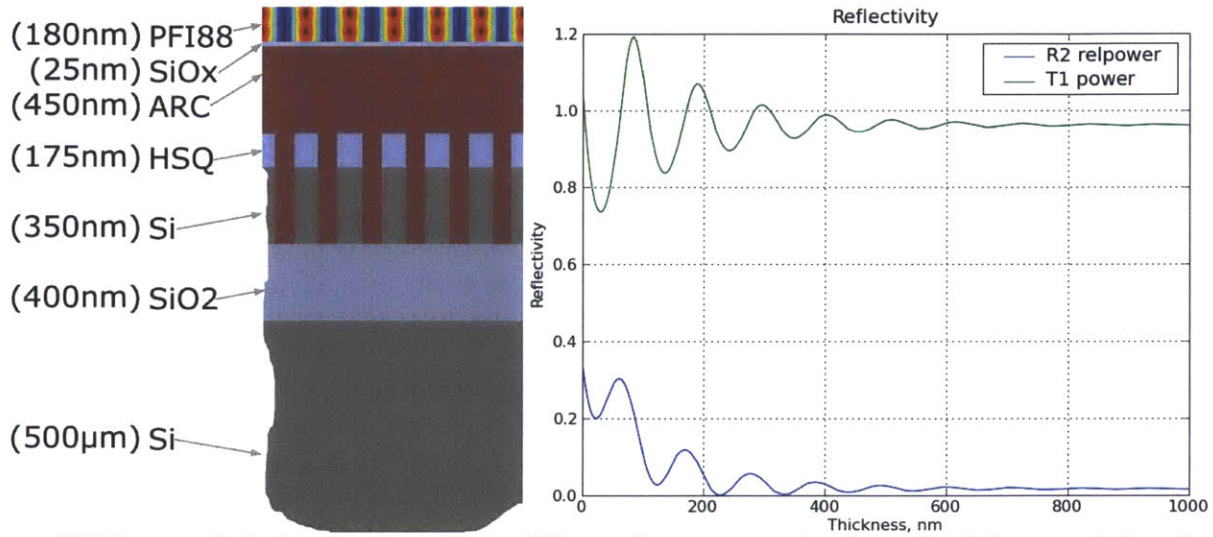


Figure 2.7 Photostack design for the rod-layer lithography process. a) schematic of the material stack as designed for IL. Superimposed on the layer of PFI-88 is the intensity calculated for the film stack defined in the figure. In theory a reflectivity of 2.6% occurs for this Barli thickness.

The Lloyd's mirror was aligned to the pitch of the holes using a monitor grating and was then intentionally shifted 2.5 mRad off alignment so the rods and holes would beat in and out of phase. After the second round of lithography and RIE the membrane was released in HF and allowed to settle onto the silicon handle. Shown in Figure 2.8 is the resulting cross-section and top view taken with the SEM inlens detector at 5kV and a working distance of 2mm. On the right hand image, the insets show the rods beating out of phase with the holes.

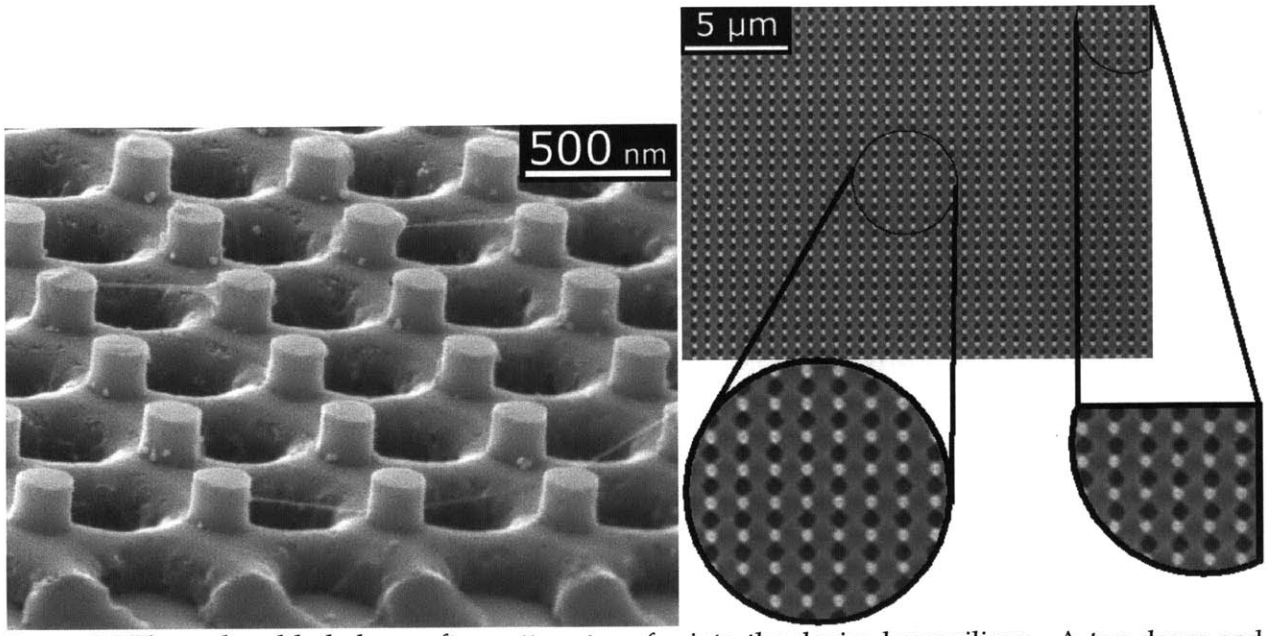


Figure 2.8 The rod-and-hole layer after pattern transfer into the device layer silicon. A top down and cross-sectional view of the patterned silicon layer after undercutting the buried oxide layer with hydrofluoric acid. The rods and holes were aligned using the moiré technique, and then intentionally misaligned by 2.5 mRad for demonstration purposes: in order that for the rods to walk less than 1 nm over 1 cm, the misalignment tolerance would reduce to 25 nRad. The eroded holes resulted from sputtering the HSQ mask during the hole-layer etch step.

Though, in this case, the angular shift during lithography was deliberate, for a large enough pattern some misalignment of the two exposures is inevitable. For example, if the periodicity of the holes was ⅔ of a micron and the rods were to shift by 1 nm over the entire 1 cm of a membrane, the corresponding angular error between lithography steps would be 25 nRad. Coherent-diffraction Lithography a novel lithographic approach was developed to reproducibly replicate periodic patterns.

**ii Pattern replication: Coherent Diffraction lithography**

The Lloyd's mirror is a convenient tool for generating periodic patterns. However, to produce the large areas of the photonic structure depicted in Figure 1.1, precise overlays of the rod and hole patterns is required. Thus a pattern replication technique, rather than pattern generation technique would be more appropriate. As a

part of this thesis, a coherent-diffraction lithography (CDL) tool [31] that relies on the Talbot effect [32] was implemented.

The Talbot effect describes the optical field emitted from a periodically patterned phase mask. This optical field takes the form of a standing wave in three-directions that depends on the wavelength of light and the pitch of the grating on the phase mask (assuming collimated, coherent light at normal incidence). For example, the photonic structure in Figure 1.1 operating at telecomm wavelengths would require replicating a periodic pattern having 660-nm pitch, hence the pitch of the phase mask would also need to be 660 nm. If the operating wavelength, $\lambda$, was 405 nm, then according to the grating equation (2) only the m= -1, 0 and +1 diffracted orders are transmitted.

$$\sin\theta_m = \frac{m\lambda}{p} \tag{2}$$

Explicitly, the intensity beyond the phase mask relates to the electric field as:

$$I \sim \left|E^2\right| = \left(E_{-1}e^{j\left(\omega t-\vec{k}_{-1}\cdot\vec{r}\right)} + E_0 e^{j\left(\omega t-\vec{k}_0\cdot\vec{r}\right)} + E_{+1}e^{j\left(\omega t-\vec{k}_{+1}\cdot\vec{r}\right)}\right)\left(E_{-1}e^{-j\left(\omega t-\vec{k}_{-1}\cdot\vec{r}\right)} + E_0 e^{-j\left(\omega t-\vec{k}_0\cdot\vec{r}\right)} + E_{+1}e^{-j\left(\omega t-\vec{k}_{+1}\cdot\vec{r}\right)}\right) \tag{3}$$

With a coordinate system in which the optical axis is along the z-direction the normalized intensity is, after a few steps of algebra (see Chapter 6.b for full derivation):

$$I^* \sim 1 + 2\alpha^2 + 2\alpha^2\cos\left(2Kx\right) + 4\alpha\cos\left(Kx\right)\cos\left(f\left(z\right)\right) \tag{4}$$

The first two terms do not include any spatial dependence, $K$ is the spatial frequency (i.e. ~$1/p$), $\alpha^2$ describes the diffraction efficiency and the final term contains an explicit z-dependence:

$$f(z)=\frac{2\pi}{\lambda}\left(1-\sqrt{1-\left(\frac{\lambda}{p}\right)^2}\right)z \tag{5}$$

When f(z) becomes an integer multiple of $\pi$ the argument to the last cosine in equation 4 describes the so-called "Talbot distance" in the z-direction where the normalized intensity has maximum contrast [31]. These distances, given in (6), deviate from the commonly referenced formula ($p^2/2\lambda$) which assumes paraxial rays.

$$z_{Talbot}=\frac{p^2}{2\lambda}\left(1+\sqrt{1-\frac{\lambda^2}{p^2}}\right) \tag{6}$$

The apparatus shown in Figure 2.9 makes use of the Talbot effect as follows. A resist-coated substrate and phase mask are inserted into the apparatus, positioned parallel to each other at a gap that is an integer multiple of the Talbot distance. Then, coherent 405-nm light from a solid-state laser is spatially-filtered and collimated to irradiate the phase mask. At every Talbot-plane, the optical field downstream of the mask encodes its periodicity which can then be recorded in the substrate's resist.

A phase mask having a 660-nm pitch irradiated by a 405-nm wavelength would have, according to equation 6, a Talbot plane every 1.92 μm. To position the mask above the substrate, Interferometric-spatial-phase Imaging [26] (ISPI) is used to measure the gap between the patterned face of the phase mask and the substrate beneath.

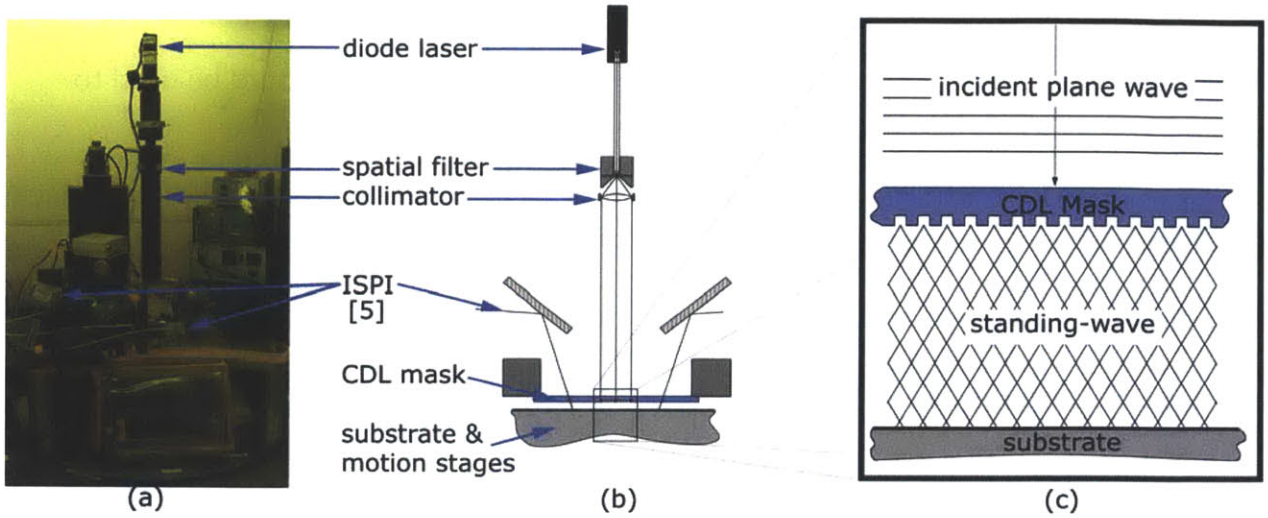


Figure 2.9 The Coherent-diffraction Lithography tool built as a part of this research. (a) system image as implemented. (b) schematic. Light from the diode laser is spatially filtered and collimated prior to irradiating a phase mask. Alignment scopes [26] provide feedback control to allow the mask to be positioned parallel to a substrate at a fixed gap. (c) the optical field beyond the mask forms a standing wave that can be recorded by a photosensitive substrate.

The ISPI alignment technique makes use of diffractive marks on the phase mask that are designed to both back diffract at the littrow angle and direct light, of a visible wavelength, down toward the substrate surface. Then upon reflection from the surface, the light that back diffracts from the ISPI marks on the mask interferes with the light reflected from the surface. This interference pattern can be interpreted as a measurement of the gap because a change in the distance corresponds to a change in the phase difference between the returning beam and the back-diffracted beam. Thus three ISPI markers incorporated into the phase mask define a plane which is made parallel to the wafer by matching the fringes patterns on each CCD. Within the ISPI scheme, it is also possible to measure the location of a pattern on the substrate with respect to the patterns on the phase mask, provided the marks on each, substrate and mask are in the beam path.

The requirement, that a pattern on the substrate needs to be fixed relative to the pattern of ISPI marks, motivated the creation of a master mask that could be used to contact print a fixed arrangement of ISPI marks onto the phase mask and onto the substrate (for pattern overlay). There was no need for overlay during a single lithography step so marks were only printed onto the phase mask. However if overlay was required, say for the structure in Figure 2.5, then the corresponding substrate marks would need to be included [33].

Figure 2.10 shows the layout of the ISPI marks that were created in a layer of chromium on a fused silica master mask. It included both patterns designed for 660-nm wavelength (Vis) or 1065-nm wavelength (IR) light though the IR marks were not used. On the left of Figure 2.10 are the locations on the master mask of the marks shown on the right. There are three marks for each corresponding wavelength and for redundancy three rings of markers were spaced at 0.5 cm radii, 1cm radii and 2cm radii.

Each mark on the right of the figure has the ability to measure the gap, 'z', and one in-plane direction either 'x' or 'y'. The marks are composed of periodic patterns that have a base pitch of $P_2$ =1 μm, which is designed to correspond to the littrow angle of the respective visible ISPI scope. Within each mark [33] are transverse chirp gapping features (T), focusing (F) features and angle tuning (A) features, in addition to grating pairs ($P_1P_3$) and checkerboards ($P_2$). Unlabelled marks were not designed for experiments described in this thesis.

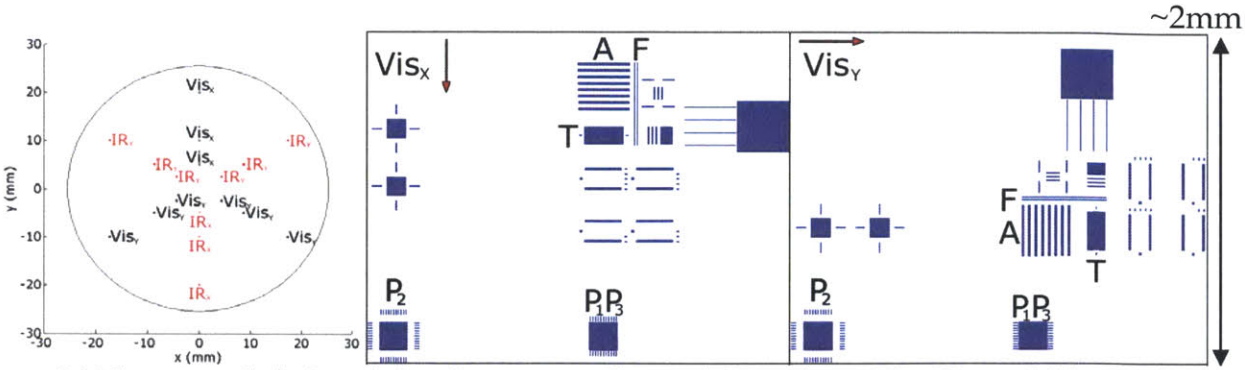


Figure 2.10 Layout and design of the alignment marks used throughout. The $Vis_x$ and $Vis_y$ marks are distributed evenly in 3 rings at 5mm, 1cm and 2cm radii on a 50.8-mm diameter mask. The IR marks were present but not used. The 'T' and '$P_1P_3$'/'$P_2$' features enable 6-axis relative positioning of the upper and lower substrates. The '$P_2$' features were similarly displaced from the '$P_1P_3$' in each mark so they could be printed and used to register a bottom substrate. Within each mark are additional features ('A' & 'F') that were used to align the microscopes. The signal from 'A' exhibits a v-shaped interferogram on the camera when the scope's mirror angles are set and the signal from 'F' become sharp when the microscope is in focus. Included in each design is an arrow that depicts the (in-plane) direction of incident light.

The F features are 50 µm-wide gratings at pitch $P_2$ that are aligned to the measurement direction of the ISPI scope. The incident light generates (from the mask) back-diffracted and (from the substrate) reflected bright lines on the scopes. To focus, the ISPI scope is moved closer to the mask until the width of the F features is narrowest. As the gap between upper and lower substrates is reduced the spacing between the resulting signals from the F features decreased to ultimately overlap at which point the T features come into range.

The T features are based on three 45 µm × 300 µm checkerboard patterns arrayed side-by-side. The pitch of each checkerboard in the measurement direction is $P_2$; in the orthogonal direction the pitch is chirped, the outer ones between 1.1 µm and 0.9 µm along the 300 µm length and the middle checkerboard is chirped in reverse between 0.9 µm to 1.1 µm. An example fringe pattern from one of the T marks is shown in Figure 2.15. Together these marks define a plane that is made parallel to the substrate when

fringe patterns between the different T features match. Then, with the analysis software written by Euclid E. Moon, the fringe pattern can be converted into a gap measurement.

In Figure 2.11 are the designs of both the $P_1P_3$ and $P_2$ marks. The $P_1P_3$ marks are a pair of gratings, each 110 μm × 220 μm arrayed side-by-side, where $P_1$ is 25 nm less than $P_2$ = 1 μm and $P_3$ is 25 nm more than $P_2$. The grating vector (defined as perpendicular to the grating lines) of each grating is orthogonal to the in-plane measurement direction for that mark. The $P_2$ feature, a 220 μm × 220 μm pure checkerboard at the base pitch, is located 1.63 mm from the $P_1P_3$ feature.

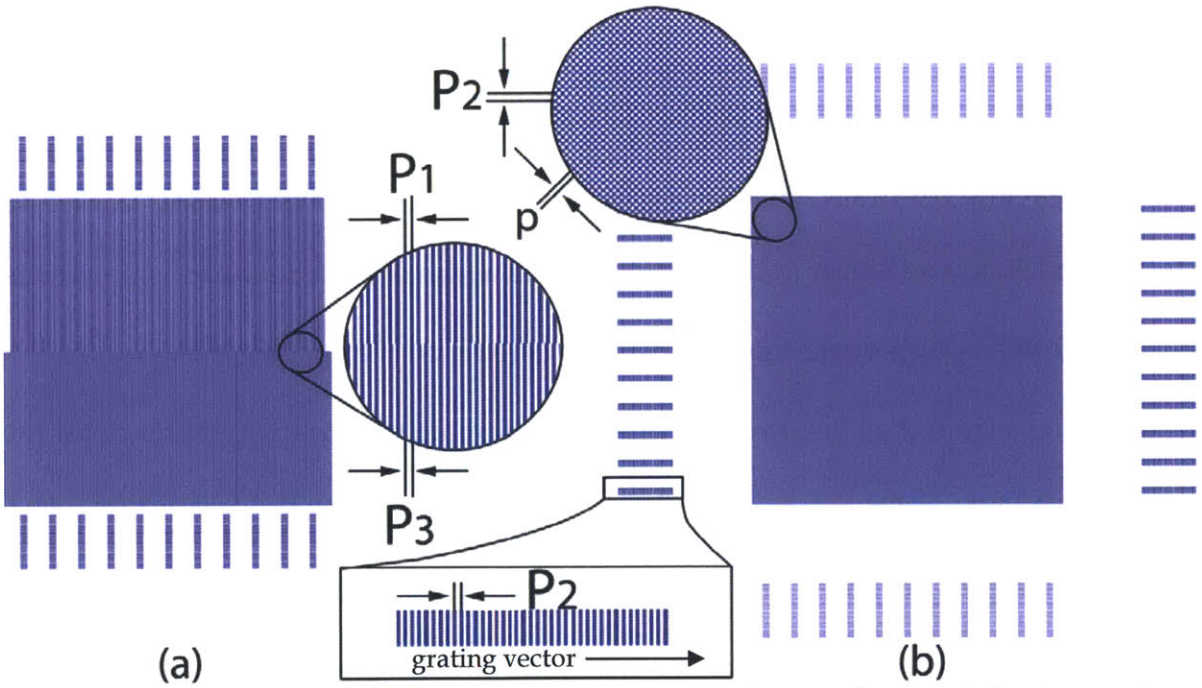


Figure 2.11 The $P_1P_3$ and $P_2$ marks. (a) shows the layout of the $P_1P_3$ feature of the $Vis_x$ mark. The different periods are labeled in the inset and are $P_1$=975nm, $P_2$=1000nm and $P_3$=1025nm. The short period of the '$P_2$' feature is labeled as '$p$' and takes the value $p=\sqrt{2}P_2$.

In addition, surrounding the $P_1P_3$ and $P_2$ features are arrays of 5 μm wide by 50 μm long grating 'bars' (see rectangular inset) with grating vector aligned to the in-plane measurement direction of the ISPI scope, which are designed to provide a fixed reference between the fringes generated from the $P_1P_3$ mark overlaid over $P_2$ features.

These features were exposed by our collaborators at Purdue, using their e-beam system. The process detail is described in the appendix, however, the pattern in polymethylmethacrylate (PMMA) was wet-etched into a layer of Cr and then this mask was then used to pattern conformal masks. These 0211-glass masks were coated with 25 nm Cr and photoresist. The pattern in PFI-88 was transferred by RIE into the Cr.

The conformable mask was then used to pattern the phase mask. Borosilicate glass, a close thermal match to Si, was chosen since it is transparent to 405 nm light. However, the borosilicate was smaller diameter and thicker than the flexible daughter masks, so a vacuum fixture was made (Figure 2.12) to hold the Borosilicate on three 6-80 ball-tipped set screws while simultaneously sealing the edge of the Borosilicate to the vacuum chamber. By lifting the borosilicate on the set screws and applying vacuum the flexible daughter mask was pulled into contact with the borosilicate without breaking. In addition to the vacuum system, inside the radius of the set screws was a window in the fixture to allow verification of intimate contact.

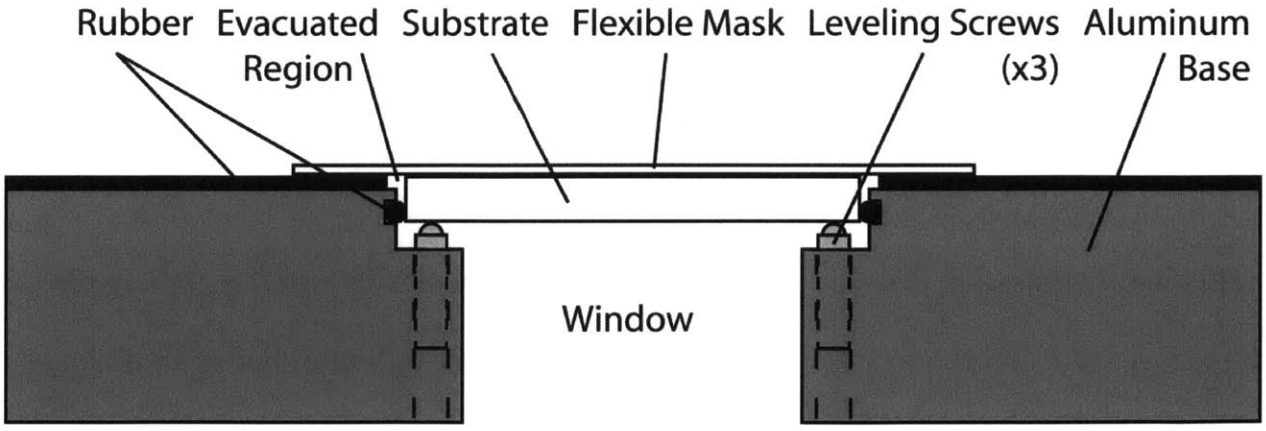


Figure 2.12 The vacuum stage. A rubber o-ring seals the 5-mm thick borosilicate substrate around its edge and a rubber sheet inserted between the aluminum base and flexible daughter mask seals the evacuated region allowing the flexible mask to be intimately contacted to the borosilicate substrate during contact lithography exposures.

The borosilicate CDL-mask was coated with a trilayer stack. However, due to its transparency an additional thick (>500nm) layer of ARC was spun on the backside to reduce the back reflections (see Figure 2.13).

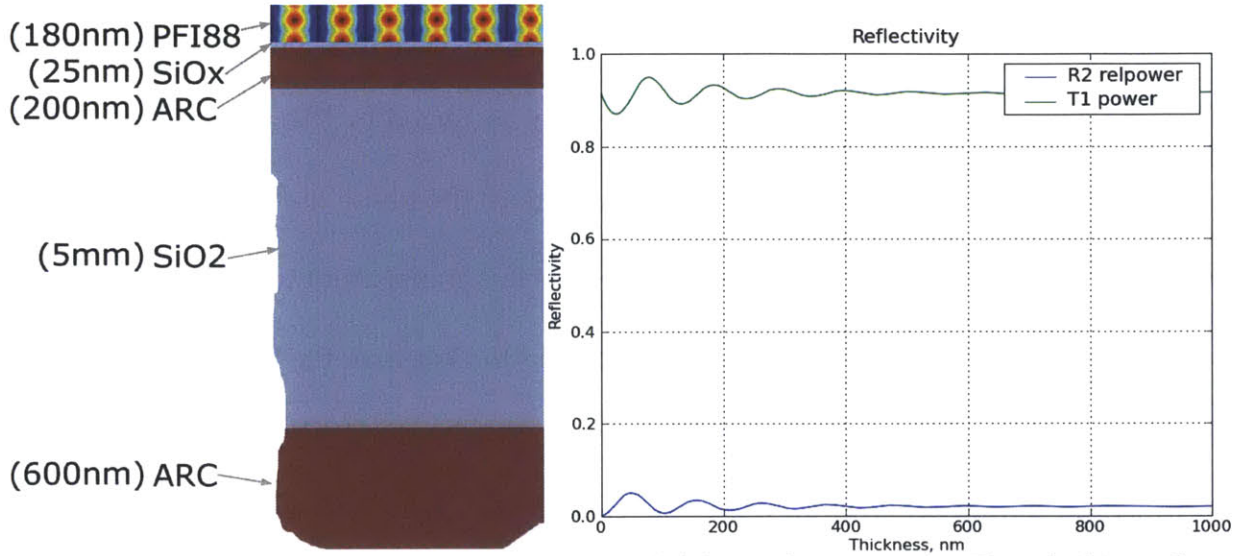


Figure 2.13 Photostack design for the CDL phase mask lithography processes. Though this stack was used to contact print the CDL mask with ISPI marks, it was optimized to eliminate reflections during the Lloyd's mirror exposures. Despite the different periodicities between the ISPI marks and grating patterns, the thick backside ARC allowed 200 nm of ARC on the front side to suppress reflectance to less than 3% during each lithography step.

After coating the borosilicate with PFI-88, the flexible daughter was contact printed to transfer the pattern of ISPI markers into its PFI-88. This pattern was then transferred into the borosilicate with RIE. Then it was cleaned, prepared for IL (again with a thick backside ARC) and patterned using the Lloyd's mirror. After development and RIE through the trilayer stack, ARC was painted over the ISPI markers (and subsequently baked) to protect them. Then, the pattern was transferred with RIE into the borosilicate. Table 6.5 of the appendix contains details; etch rates had to be adjusted from the typical values because thicker substrates etch more slowly.

To test CDL a trilayer-stack coated a substrate that was loaded beneath and brought parallel with the phase mask at a gap of 1.92 μm. Figure 2.14 shows the material cross-section and reflectance plot. Figure 2.15 shows the fringe patterns observed on a 'T' mark and Figure 2.16 shows the developed photoresist in both cross-section and top views imaged in the SEM at 5 keV and a 3mm working distance.

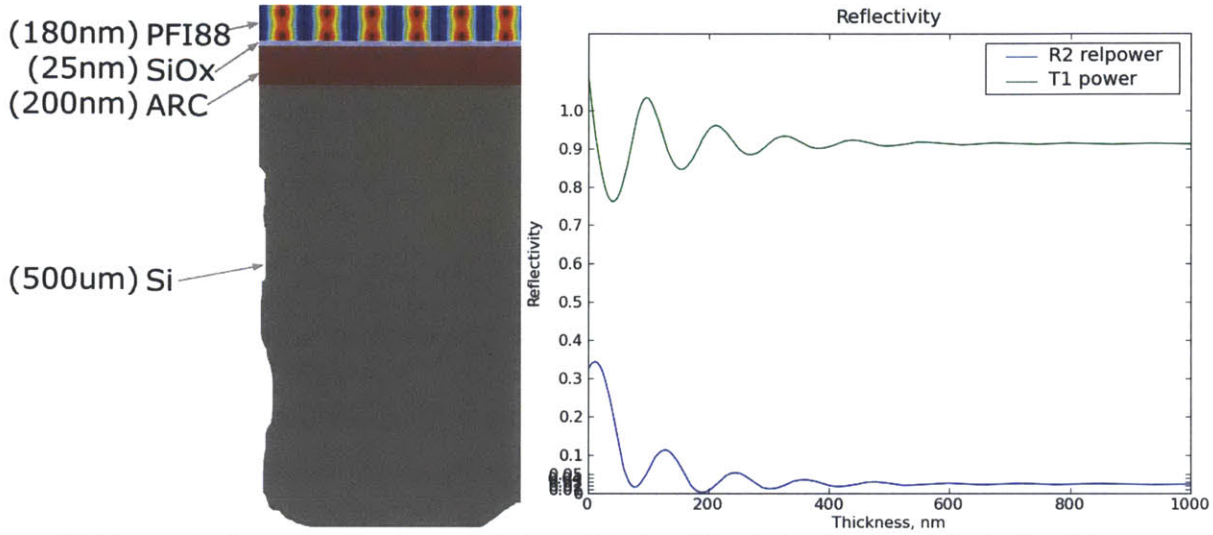


Figure 2.14 Photostack design for the substrate printed with CDL. On the left, is the trilayer stack optimized for exposure to 405 nm light. On the right the reflectivity is plotted against ARC thickness.

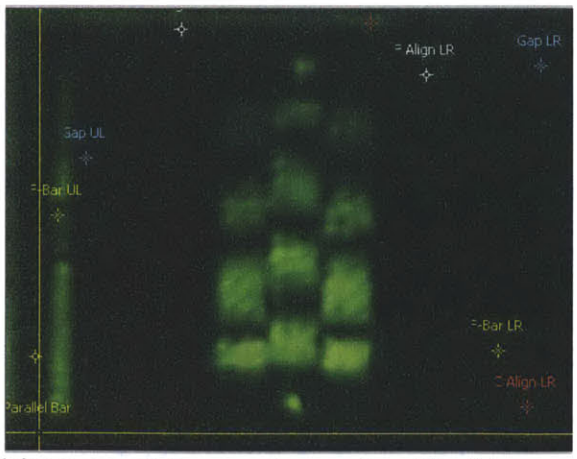


Figure 2.15 Alignment signal from one of the gapping marks. The fringe pattern from the VISx T mark corresponded to a gap of 1.92 μm. The three columns of fringes each have 3.5 fringes. In this case, the phase relationship between the center column and outer columns is such that the half fringe extends roughly a quarter fringe cycle past the fringe next to it.

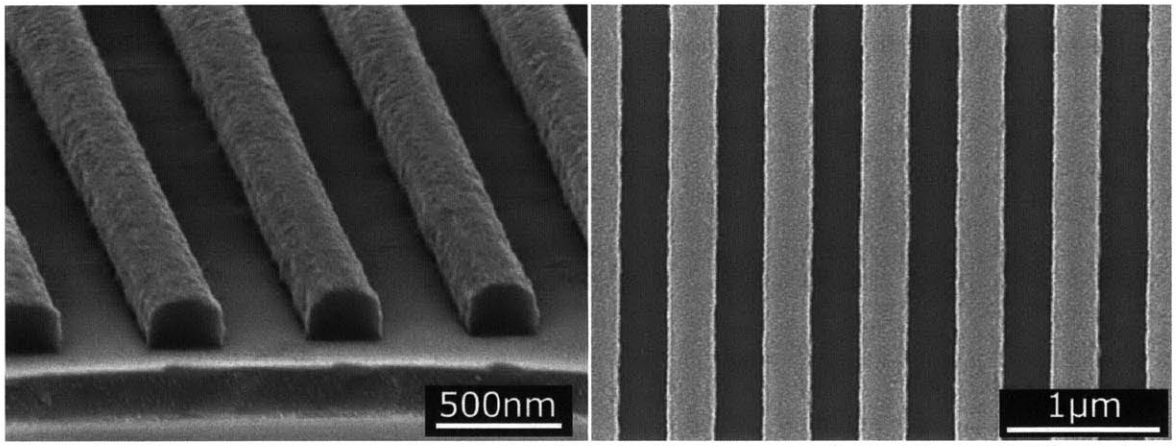

Figure 2.16 Coherent-diffraction Lithography result. The pattern on the mask was replicated in the photoresist on the substrate with an exposure dose of 108 mJ/cm$^2$. The mask was positioned with the inner set of $Vis_x$ and two $Vis_y$ ISPI marks at a fixed gap of 1.92 μm from the substrate.

CDL is capable of replicating the pattern on a mask and more work could be done using it to create precisely overlaid rod and hole patterns shown in Figure 1.1. However, from the standpoint of making and stacking membranes this capability is not a requirement nor does a photonic crystal necessarily require rod and hole patterns.

**iii The Meshpile Structure: only holes**

In collaboration with a post-doctoral associate Ling Lu, fellow graduate student Lin-Lee Cheong modeled a photonic crystal *meshpile* structure [34] specifically designed for the stacking paradigm as illustrated in Figure 2.17. The structure contains membranes patterned with only a grid of holes, which are each shifted from the neighboring membranes by a half period of the pattern, first in one direction and then the other (see inset). The process is considerably simplified by eliminating the rod-based processing steps (see Table 6.4 for details). Moreover, with these patterns, the overlay capability of coherent diffraction lithography is no longer required to align multiple lithography steps. Thus conventional interference lithography should be well suited to pattern these membranes.

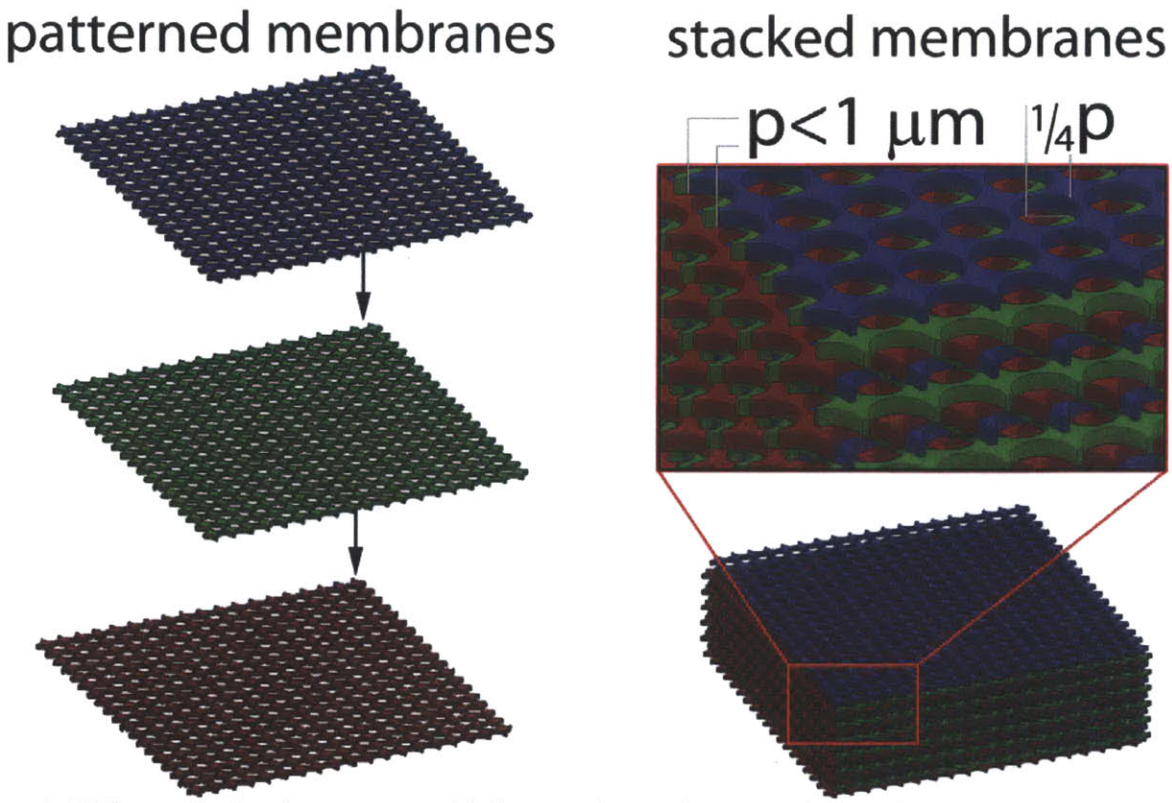


Figure 2.17 The meshpile photonic crystal following the stacking paradigm. This structure composed of only layers of holes [34]. The dimensions are representative of photonic crystals operating at optical frequencies, though to optimize the bandgap for this silicon/air structure at the 1.55 μm wavelength, the authors reported that a 42% hole radius (of the 605 nm pitch) would give rise to a 14% bandgap.

Previously, the Lloyd's mirror interferometric lithography tool was used to generate an array of holes, an array of rods superposed on an array of holes and a grating for a CDL mask. CDL was also used to replicate this grating pattern. Both the Lloyd's mirror and CDL are useful and have different limitations: at ~660 nm pitch the Lloyd's mirror can generate arrays of holes roughly 3 cm × 3 cm in area and while CDL is an attractive replication process, a faster approach that does not require careful mask-substrate parallelization and covers larger areas can be found with the Mach Zehnder interferometric lithography tool shown in Figure 2.18.

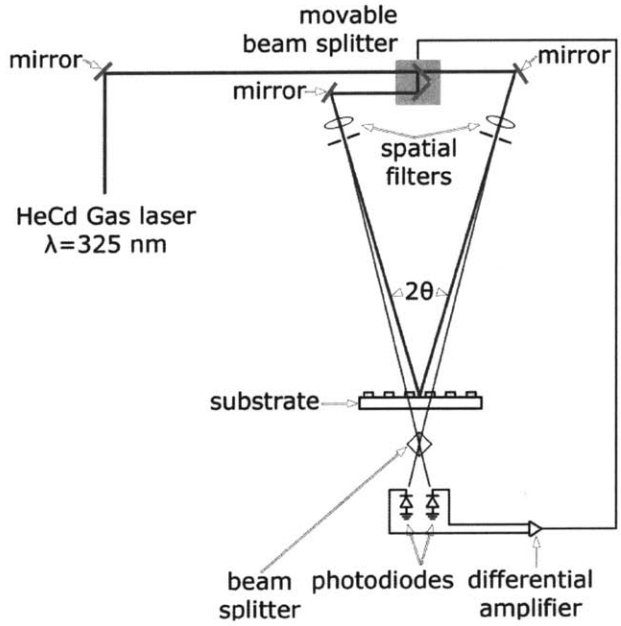


Figure 2.18 Illustration of our Mach Zehnder IL tool. Coherent light from a HeCd laser is split by a movable beam splitter into two arms. Spatial filters for each arm send light to both the substrate and a fixed beam splitter. During exposure, the substrate and fixed beam splitter are illuminated with light from each spatial filter. The fixed beam splitter sends interfering optical signals (from each arm) to the pair of photodiodes. These photodiodes control the movable beam splitter via a differential amplifier to lock the standing-wave exposure at the substrate in place [28].

While a Lloyd's mirror interferometer splits one spatially-filtered beam into two using a mirror, a Mach Zehnder interferometer differs in that it splits the beam with a 50% mirror *before* spatially filtering both beams. The Lloyd's mirror has the advantage of stability to vibration (due to the mirror being rigidly fixed to the substrate chuck), however, the pattern size is limited by the size of the mirror and phase errors are exacerbated by the reflection from the mirror. In contrast, the Mach Zehnder system requires active control over the optical-path-length difference between the arms of the interferometer [35], but can produce patterns over the full area of a wafer.

The in-plane standing-wave period depends on the angle $\theta$ (see equation 1) between the two arms of the interferometer and being able to reproduce this period will be important. For instance as discussed in chapter 5, the grid pattern printed with the

Mach Zehnder could be used within the ISPI alignment paradigm as the $P_2$ checkerboard: if the exposed pitch of the grid is within a few nanometers of 707 nm then the long pitch of the grid (i.e. the checkerboard pitch) would be close to the base pitch of the ISPI $P_2$ markers. Interestingly, differentiating equation 1 with respect to $\theta$ indicates that 1 nm of error in pitch would correspond to an angular error of 334 μRad, or for spatial filters 1 m away from the stage, the pitch would change by 1 nm if the filters moved 334 μm. While pattern replication would eliminate this variability, careful alignment of the Mach Zehnder should suffice.

To reproduce a known period the spatial filters were removed and a monitor substrate previously patterned with a grating was placed onto the substrate chuck to diffract incoming collimated light. Then the beams were centered on the substrate and the back-diffracted and reflected beams traversed back through the system to interfere on a fluorescent screen. Adjustment of both the in-plane substrate rotation and position of each mirror caused the four returning beams to interfere on the screen. Once there was only one fringe on the screen, the coarse angular alignment condition is met.

After coarse alignment, the spatial filters were incorporated into the beam pathways. Select diffracted light cones from the monitor wafer were then imaged onto a fluorescent screen that was placed in front of the left spatial filter. Similarly a viewing card was placed off to the left side where diffracted orders overlapped. For illustration purposes an example interferogram formed on the viewing card is shown in Figure 2.19 (including pinholes reduced the intensity below what the camera could image, but fortunately eliminated the artifacts from the imperfect lenses). As the lenses and

pinholes were positioned the fringe period changed so that when the lenses and pinholes came into alignment the fringe period grew larger. The in-plane rotation of the monitor on the chuck was done by hand which made it difficult to reach one fringe across the entire field. Furthermore, adjustment of the spatial filters along the optical axis was not possible so the bull's-eye pattern consistent with overlapping spherical waves was typically observed. Regardless, the largest fringe period with the bull's-eye centered over the hole in the fluorescent screen occurs once the Mach Zehnder is aligned.

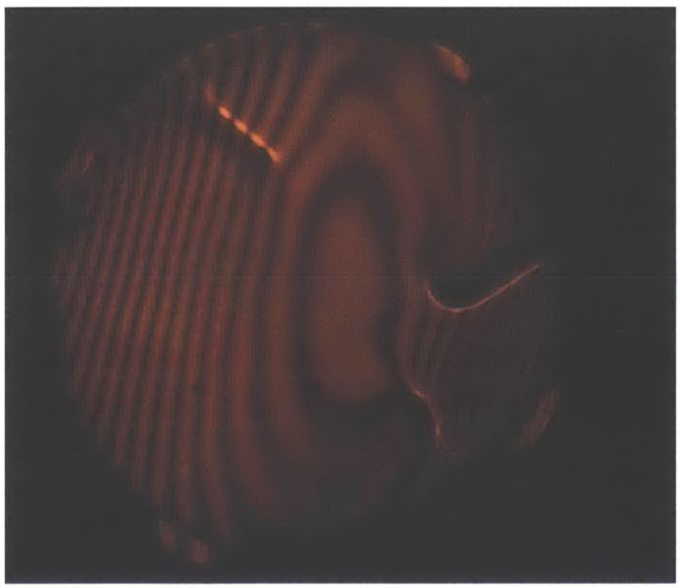

Figure 2.19 The fringes generated on the viewing card during alignment of the Mach Zehnder. The +2 order and -2 orders are shown interfering on the card. As the lenses are moved into alignment the fringe period grows larger. After moving the lenses around this was the largest fringe pattern that was found and the pinholes were then added into the spatial filters. With the pinholes in place the fringes were projected onto a card placed in front of the left arm and the bull's-eye pattern was centered on the hole in the card by moving the pinholes into alignment.

Once aligned the Mach Zehnder could be used to record an array of holes into negative photoresist with two orthogonal exposures. Figure 2.20 shows both the material stack and the back reflection as a function anti-reflection thickness for the substrate design. Again, following the procedure to eliminate vertical standing waves

in the resist a dielectric stack was incorporated between the photoresist and silicon device layer. Figure 2.21 shows a typical cross-section (imaged in the SEM at 5 keV with a 5 mm working distance) of the patterned resist following the recipe in Table 6.7. After development of the resist, the wafers were quartered to optimize the pattern transfer and bonding steps (see Figure 2.3). The pattern transfer process is similar to that presented before - i.e. trilayer etching steps followed by transfer through the oxide with $CHF_3$ and finally thorough the silicon with HBr. A final $CHF_3$ etch step was used to strip the 100 nm $SiO_x$ mask from the front side of the device layer silicon.

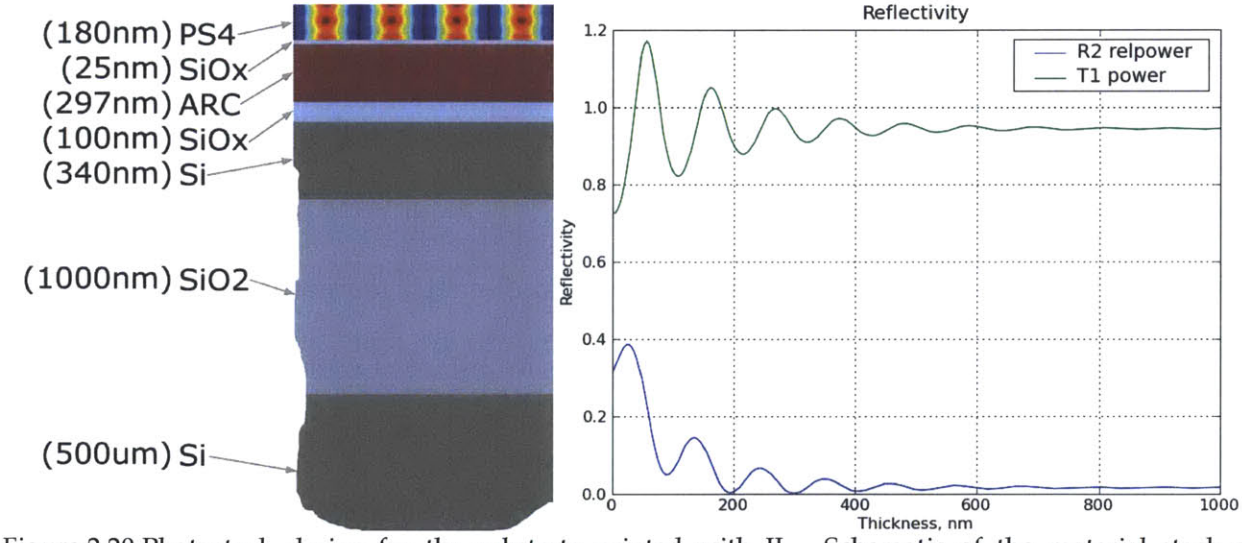


Figure 2.20 Photostack design for the substrate printed with IL. Schematic of the material stack as designed for IL. Superimposed on the layer of PS4 is the intensity calculated for the stack of materials described in the figure. That the vertical standing-wave is negligible at this thickness of Barli is confirmed by plot of reflectivity which has a reflectivity of 0.15% at an ARC thickness of 297 nm.

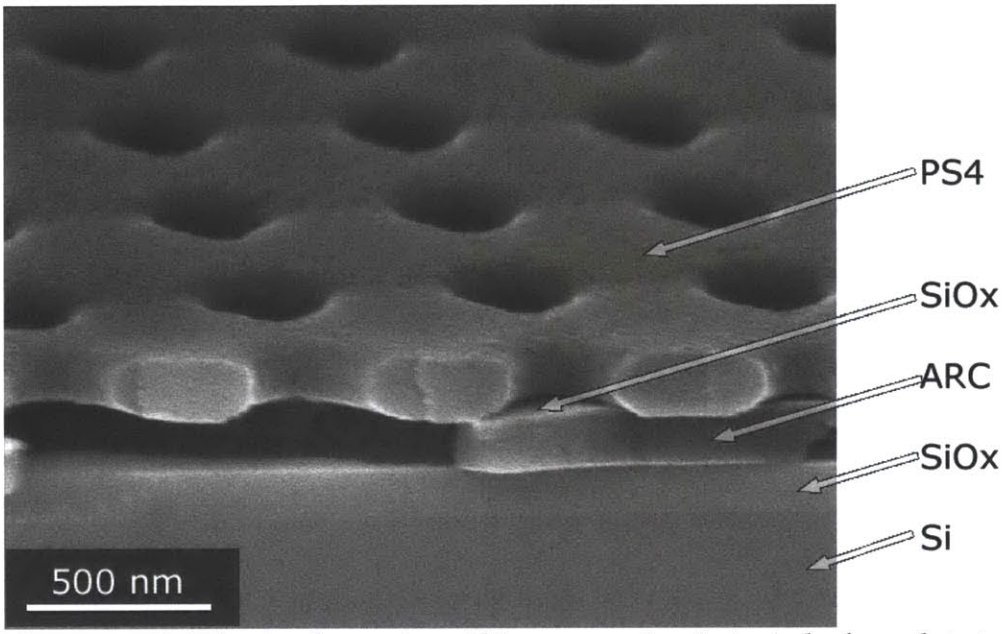


Figure 2.21 An array of holes in photoresist. This cross-section is typical of a substrate processed according to the parameters in Table 6.7 (though this ARC – at ~100 nm thick – was not optimized to the third node of Figure 2.20b). The buried oxide and handle silicon are not shown.

After the silicon was patterned with the grid of holes and the oxide mask was stripped, another round of planar fabrication steps was required to single out the 36 regions of the device layer that would become 1-cm-diameter membranes (see appendix for details). Figure 2.22 shows one of these regions illuminated with room light.

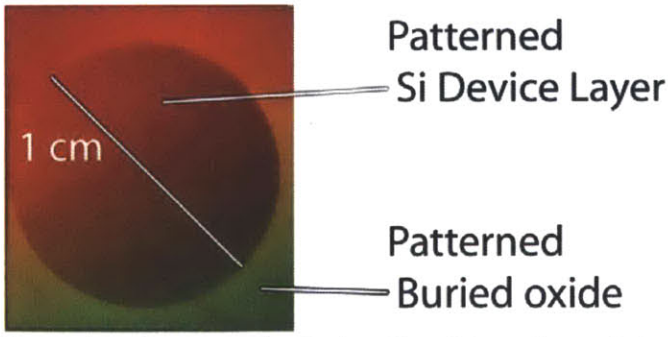


Figure 2.22 Patterned SOI sample prior to anodically bonding it to a glass substrate. The circular region is the patterned device layer that will eventually become a membrane. The membrane is defined via contact printing and reactive-ion etching its exterior in CF4.

It was found that the compressive stress in the SOI device layer made releasing 1-cm-diameter membrane regions directly from the handle silicon unreliable (<16%

yield) (recall Figure 2.2). In fact, once a membrane "stuck" down to the handle silicon it would not release, even though it was not chemically bonded to the handle silicon (scotch tape would remove it but fluid flow did not). A physical justification for the reason why the membrane would not float away is presented in the appendix (Chapter 6.c). This observation directly influenced the fabrication approach toward releasing silicon membranes. Instead of trying to etch the buried oxide to release the membrane, the membrane layer was anodically bonded to glass and then the silicon handle was stripped in TMAH. Then, instead of the reaction terminating once the buried oxide was consumed, it continued and the membranes released from the underlying substrate.

Thus the wafers were anodically bonded to borosilicate substrates to improve the yield of the membrane release step. Then, Protek ® B3 (Brewer Science) was painted around the edge to prevent TMAH from being drawn into the space between the regions of the patterned device layer and the substrates were etched in 25% TMAH at 90 °C until the handle silicon was removed. Intermittent inspection was necessary to decide when the handle silicon was cleared. Near the end, the borosilicate substrates were rinsed in DI and die-sawed into 1.2 cm × 1.2cm samples because the temperature gradient in the TMAH bath required different over-etch times to fully clear the residual silicon as described in Figure 2.23.

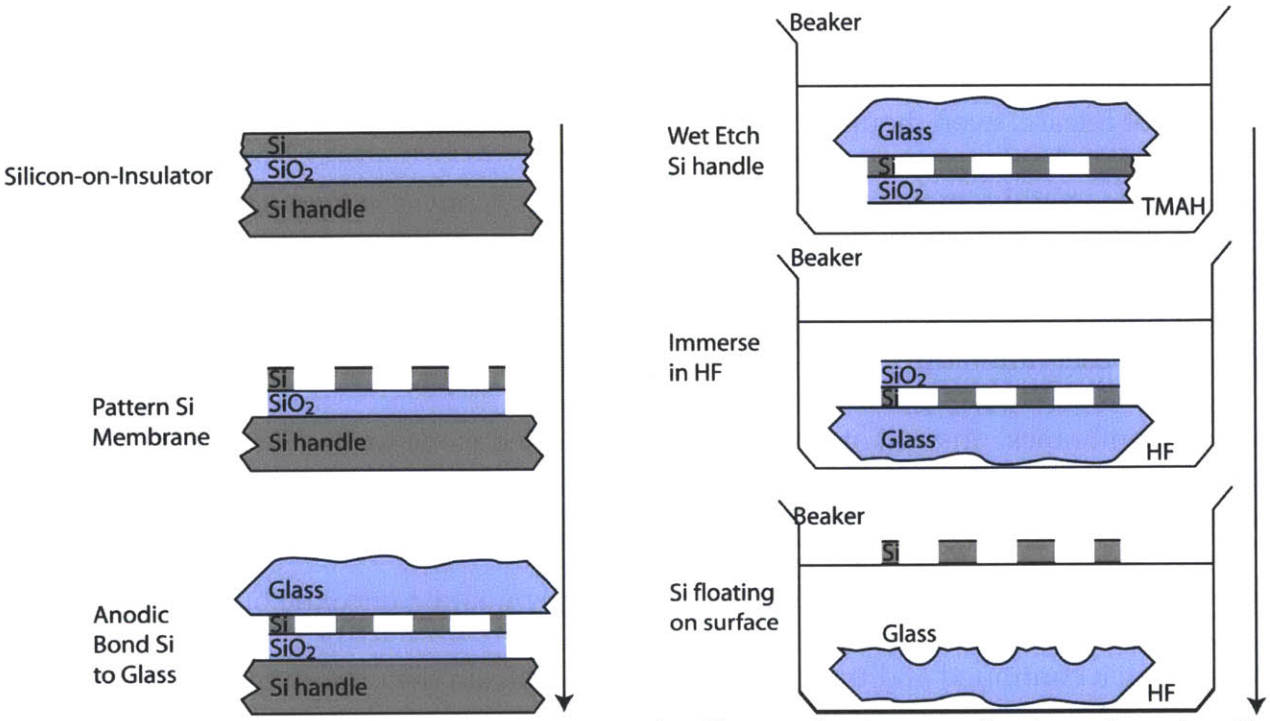


Figure 2.23 The membrane fabrication process. A silicon-on-insulator wafer is patterned with interference lithography and contact lithography. The patterns are transferred into the membrane layer with reactive-ion etching to create 1-cm-diameter regions of patterned silicon throughout the top layer of the SOI wafer. The patterned silicon membrane layer was then anodically bonded to glass, protected around the edge with Protek and the handle silicon was etched away from the backside in 25% TMAH. Subsequent immersion in buffered oxide etchant undercut the silicon membrane, releasing it to float on the surface of the buffered oxide etchant.

After the handle silicon was removed, the samples were ready to be turned into membranes. The samples were submersed in ammonium fluoride and hydrofluoric acid (BOE) for 20 to 45 minutes. Figure 2.24 shows a time-lapse of the membrane release process where membrane ends up floating at the surface of the BOE after it was released from the borosilicate substrate. Sometimes, if the membrane did not surface within 45 minutes, a polypropylene syringe was filled with BOE, which was flowed between the membrane and handle to help the membrane detach.

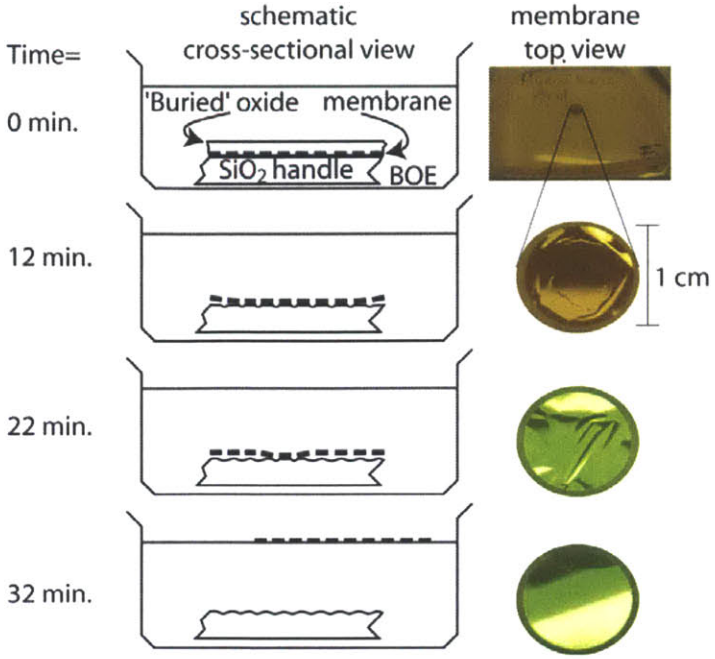


Figure 2.24 Release sequence of a 1-cm membrane. After removing the Si handle, this sample was cleaned in Piranha and submersed in buffered oxide etchant (BOE) for 32 minutes. At 12 min., the now-face-up buried oxide (BOX) was removed and BOE permeated patterned silicon to begin to release the edges of the membrane. At 22minutes, the membrane was substantially released, with the exception of three spots still anchored to the glass. After 32 minutes, the membrane was freely floating.

This chapter focused how to fabricate membranes. Silicon membranes fabricated for the frame-based approach of [25] buckled. The buckling was addressed: silicon that was bonded to glass was thinned by grinding/polishing but ultimately the SOI process of Figure 2.23 was adopted. Another issue regarded periodic pattern replication. Coherent-diffraction lithography was developed as a technique to reproducibly replicate periodic patterns; however the Mach Zehnder should be sufficient for grid patterned membranes that stack up into the structure described in Figure 2.17. Finally, the alignment marks that were described in the context of CDL extend to the precision stacking approaches explored in Chapter 5. However, before stacking is described in Chapter 4, handling techniques that resulted from hydrostatic analysis of the floating membranes are described in Chapter 3.

# Chapter 3. Manipulation of freely-floating membranes

The previous chapter discussed fabrication methods to make freely-floating pre-patterned monocrystalline silicon membranes. This chapter describes how to handle and manipulate them in preparation for stacking. Care is needed because a 350-nm-thick membrane is too delicate to be picked up with, or even touched by, anything as large as the tip of a tweezers. Thus new methods to handle them were developed. In many ways, handling techniques remain the pivotal issue when dealing with delicate substrates: such a myriad of approaches [36] - [37] developed by the semiconductor industry to indirectly handle 50-μm-thick substrates through the use of a carrier wafer is indicative of the lack of an established handling technology for micron-scale semiconductor wafers. Moving to even thinner substrates will undoubtedly require additional innovations as the technology to stack them matures.

Instead of indirectly handling delicate substrates through the use of a solid carrier substrate, this chapter focuses on methods to handle membranes when water is used as the intermediate carrier. Observation of the free floating membranes enabled several handling techniques. Specifically, the freely-floating membranes described in chapter 2 needed to be added and removed from a beaker, moved along or alternatively held on the surface of the liquid, moreover in some instances, the membranes also needed to be dried onto a carrier.

a. **Observations**

In developing these methods several aspects of floating membranes were observed: (i) silicon oxidizes rapidly when submerged in water, (ii) surface-tension forces act strongly on a membrane; (iii) a porous membrane is difficult to re-submerge once surface tension holds it at the surface; (iv) diffracted light from a drifting membrane contains information about its orientation and quality and (v) though not relevant but included for completeness surface tension of the fluid and electrostatics can affect the behavior of the membrane.

**i Oxidation of hydrogen-terminated silicon**

Throughout much of this work, the free floating membranes were thought to be hydrophobic. With their release in hydrofluoric acid leaving the silicon surface hydrogen-terminated it was assumed that the surface remained hydrophobic despite the presence of water. However, the membranes are patterned with an array of small holes so the hydrophobicity of the surface of the holes will affect the hydrostatic behavior of the membrane during floating and stacking. To quantify how long the surface of hydrogen-terminated silicon remained hydrophobic when submerged in water an experiment was conducted. It was observed that hydrogen-terminated silicon begins to oxidize within 10 minutes of being submerged in water.

The experiment to determine how quickly silicon begins to oxidize when submerged in deionized water was performed on four hydrogen-terminated quarter-wafer samples three of which were tested after every minute of submersion in water with one of the following tests (the final quarter-wafer was used as a control wafer):

- Ellipsometry ("E") test: record $\Psi$, $\Delta$ with the ellipsometer: in the absence of oxide the measured values of $\Psi$ & $\Delta$ will not map to thickness or refractive index.
- Water-runoff ("WR") test: observe the behavior of water with the sample surface by (i) holding it parallel to the ground while dripping deionized water onto it and (ii) tilting it so the water runs off the surface. Observe (i) the static contact angle and (ii) the trailing edge of the water as it runs off the surface.
- Steam-nucleation ("SN") test: in a clean beaker, boil water and quickly steam the surface of the sample by momentarily holding it facedown near the water. Observe the steam as it evaporates on the sample surface: a uniform pattern of droplets indicates a surface that is hydrophobic, thickness interference fringes indicate a surface that is very hydrophilic and a non-uniform pattern of droplets indicates a contaminated surface.

Initially the samples were etched in buffered hydrofluoric acid for the same amount of time it took to release a membrane. They were then (carefully) removed from the acid and tested again prior to submersion in water - each test confirmed that the samples were slightly hydrophobic. Then, setting aside the last quarter-wafer as a monitor, the remaining quarter wafers were submerged for 1 minute intervals until all tests confirmed that a native oxide was present. Explicitly, the experiment followed:

1. In the fume hood, RCA-clean a glass cover slip, a petri dish, a Pyrex beaker (for steam nucleation test), a Teflon beaker and Teflon tweezers for 30 minutes. Rinse each with DI water and dry.
2. Cleave a prime wafer into quarters: $X_1$ (WR), $X_2$ (SN), $X_3$ (E) and $X_4$ (E, control sample).
3. Observe that the prime silicon is hydrophilic applying tests to $X_1$, $X_2$ and $X_3$.
4. Etch samples in buffered hydrofluoric acid for 50 min. This step, longer than necessary, was chosen to mimic the membrane release process though the native oxide etches away in < 10 min.
5. With Teflon tweezers, remove samples from the buffered hydrofluoric acid.
6. Inspect samples for hydrofluoric acid droplets on edges, blow excess droplets into sink with $N_2$.
7. Set samples aside, dump the buffered hydrofluoric acid into sink and rinse out the Teflon beaker.
8. Cover $X_4$ (control) with clean petri dish and leave in the hood, do not wet surface.
9. Fill the Teflon beaker with DI water.
10. Perform tests: water runoff on $X_1$ (WR); $X_2$ (SN); $X_3$ (E) and $X_4$ (E).
11. Submerse $X_1$, $X_2$ and $X_3$ in DI water for 1 minute.
12. Repeat step 10 & 11 until oxide is observed.
13. After experiment observe $X_4$ with water-runoff test.

After 10 minutes, all tests confirmed that there is some oxide present on the surface. Static contact angle was near 90 ° immediately after hydrofluoric treatment but

prior to water treatment; after 1 hour of submersion in water it dropped to less than 30 ° and continued to decrease thereafter. It was concluded that in water the silicon surface oxidized on the same time scale as it was expected to take to stack a membrane. This could be problematic because a surface that wets will behave differently during stacking potentially allowing water through the holes (see Figure 3.1).

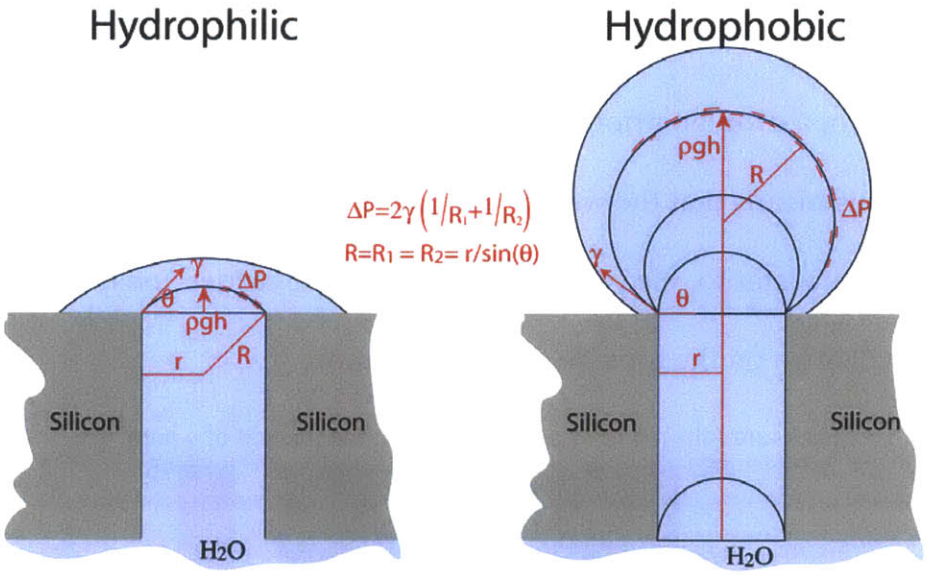


Figure 3.1 Hydrostatic interaction of water in a membrane hole. If the surface of the silicon is hydrophilic then capillary forces will draw water into the hole and any additional pressure forms a bead of water on the top surface. With enough pressure, the bead overcomes the contact angle and spills out of the pore. Instead, if the surface of the silicon is hydrophobic, applied pressure first forms a bead of water at the bottom of the hole and then the water rises toward the top of the hole. After breaching the hole, the bead will continue to grow until it surpasses the contact angle at which point the water will spill out of the pore.

Once it is submerged in water the silicon begins to oxidize. The contact angle will depend on the oxide that forms on the silicon and thus the amount of pressure to breach the hole will change accordingly. Within a 410-nm-diameter hole the bond number, which describes the ratio of gravity for body forces to surface tension forces, is small: $B_0 \sim 5.6e^{-9} << 1$. This indicates that the meniscus will have a spherical curvature given by the Young-Laplace equation (see Figure 3.1). The pressure to form a spherical

droplet scales with the inverse radius of the hole and dominates the behavior because the hydrostatic pressure head is small for thin membranes:

$$P_{curvature}(r) = \frac{2\gamma \sin\theta}{r} > \rho g h = P_{hydrostatic} \tag{7}$$

The curvature pressure in (7), parameterized by pore radius and contact angle, is plotted in Figure 3.2. The horizontal line indicates the typical radius of the holes in membranes used in this work[2]. As the surface of the silicon becomes more hydrophilic the pressure to form a droplet, prior to breaching the hole, will decrease with the contact angle. This means that the water-based stacking approaches will depend on the pressure applied by water to release membranes from the carrier: too much pressure implies water will form on the topside of the membrane.

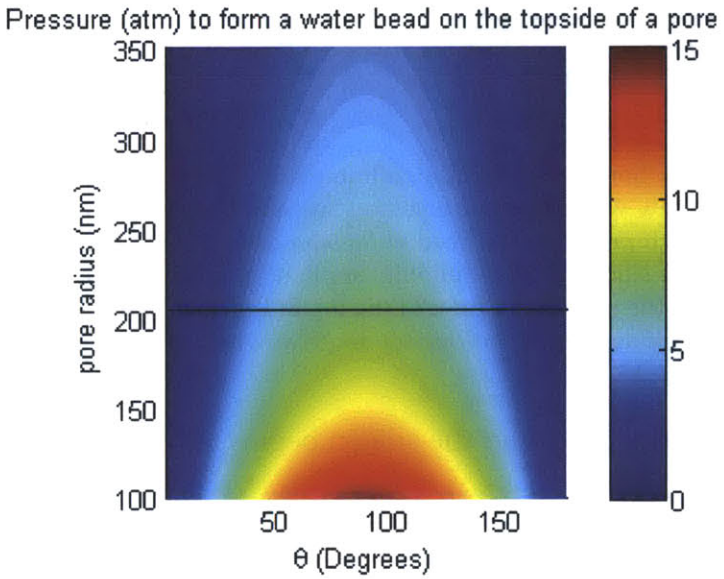


Figure 3.2 The pressure to form a spherical droplet. From equation 12, this pressure depends on the contact angle and the radius of the holes. The pressure applied to the membrane is balanced by this curvature pressure and the pressure head, ρgh. For the hydrophilic membranes, the water bead forms with very little dependence on the pressure head because capillary forces draw the water into the hole, while for the hydrophobic case, the water bead initially forms at the bottom of the hole and then excess pressure is required to push it to the top of the hole.

[2] note that this radius, ~28% the pitch, is less than what would be required for the optimized meshpile photonic crystal described in [34]

### ii Hydrostatics and Surface Tension

Membranes that float on the surface of both hydrofluoric acid and water sink into solvents. Initially, the membranes are hydrogen terminated from the hydrofluoric acid and are thus hydrophobic, but as observed in (i) within a few minutes a native oxide layer begins to develop (see also [38] chapter 2) and the contact angle changes accordingly. The authors in [39] report the contact angle between silicon and water for different silicon surface treatments with a minimum angle of ~5° for a silicon wafer that has been oxidized in boiling RCA for 10 minutes at 100 °C.

Despite a wide range of contact angles, the membranes remain floating, even after months of sitting in deionized water. Each 350-nm-thick, 1-cm-diameter membrane patterned with a 715-nm-pitch grid of 410-nm-diameter circular holes would have a surface area of 58.27 $mm^2$, a volume of 0.0204 $mm^3$ and a mass of ~ 47.5 ng, leading to a surface-area-to-volume ratio of ~2.85 million. However, the density of silicon is larger than water and so the forces that hold the membrane at the surface probably come from surface tension. This section provides a physical model for the mechanism by which the membrane floats.

Figure 3.3 depicts a membrane that is floating in a beaker on the surface of water. The membrane is drawn floating on the surface of a beaker of water in Figure 3.3a and in Figure 3.3b, the membrane is drawn in an exaggerated free body diagram that highlights the distance $h$ that the membrane recedes into the surface and the angle $\theta_a$ made between the water surface and membrane. The membrane pores are enlarged for

clarity in Figure 3.3c where the membrane is defined with a thickness $t$, pore diameter $d$, and periodicity $w$.

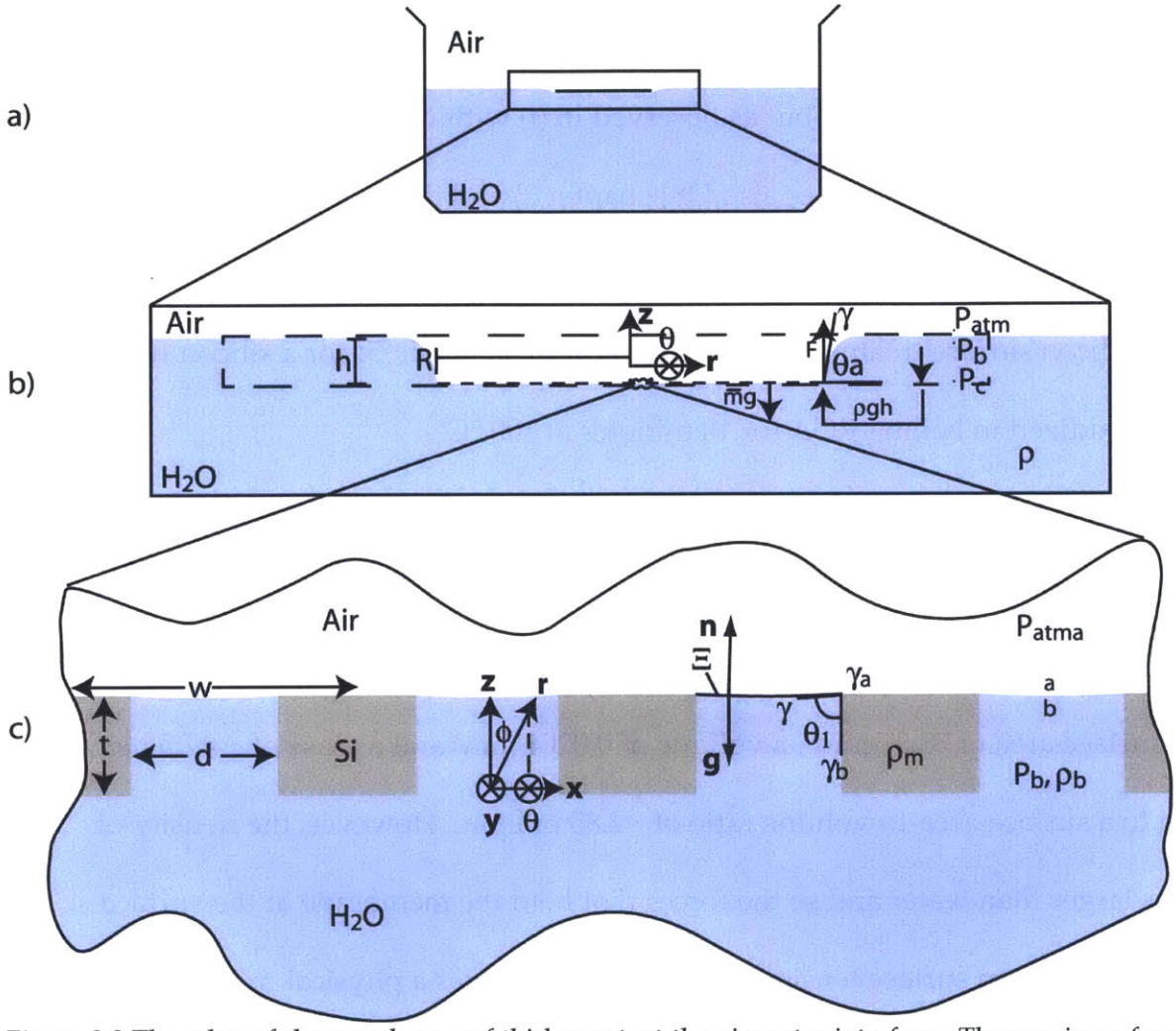


Figure 3.3 The edge of the membrane, of thickness t, at the air-water interface. The meniscus formed by surface tensions, γ holds the membrane to the surface because the free surface area is larger than if the membrane was absent. In open surfaces, e.g. membrane pores or away from the membrane, surface tension, γ, is balanced by the pressure drop across water-air interface and gravity forces.

In Figure 3.3b, the membrane displaces "its own weight of fluid". At the edge of the membrane, assuming a nonzero contact angle, the interface is pinned at the top circumference of the membrane and as long as the meniscus of water doesn't progress over the membrane, it will continue to float. At this corner, surface tension acts on the membrane to both pull it taught and lift it up. By Archimedes Principle, the z-

component of the line-integrated surface tension along this circumference provides a force that must be balanced by difference between the gravitational force and the hydrostatic force on the membrane. From Figure 3.3b this force balance is expressed as:

$$\left[m^* g - \rho g \pi r^2 h = 2\pi r \gamma \sin\theta\right]_{r=R} \Rightarrow \left[h = \frac{2\gamma}{\rho g r}\left(\frac{m^* g}{2\pi r \gamma} - \sin\theta\right)\right]_{r=R} \tag{8}$$

Equation 8 relates the angle $\theta$, which may differ from the contact angle, to the depth of the membrane at the radius R for a membrane of mass $m^*$ assuming a hydrostatic equilibrium. An additional equation that relates $\theta$ to h is needed to solve it.

The Young-Laplace equation relates the pressure across an interface to the curvature of the interface between air and water. Far away from the membrane, where the interface is flat, the pressure across the interface is negligible and the surface is at zero height, i.e. h(r) = 0. As the interface approaches the radius of the membrane the height increases and the hydrostatic pressure increases by ρgh(r). If the air-water interface is described by a function $\Xi(r,\theta,z,t)$ that is defined to be zero whenever the coordinates describe a point on the interface then for a circular membrane in hydrostatic equilibrium, the interface (for radii greater than the membrane) can be described as:

$$\Xi(r,\theta,z,t) = h(r) - z \tag{9}$$

Then, because the magnitude of the surface gradient defines the surface normal:

$$\vec{n} = \frac{\nabla_c \Xi(r,\theta,z,t)}{\left|\nabla_c \Xi(r,\theta,z,t)\right|} \tag{10}$$

By the Young-Laplace equation, in a cylindrical coordinate system, the pressure drop across the interface is the divergence of the normal vector scaled by surface tension:

$$P(r) = -\gamma\left(\nabla \cdot \bar{n}\right) \tag{11}$$

At the membrane edge the depth of the meniscus is assumed to be h and the meniscus forms an angle $\theta$ between the top surface of the membrane and the meniscus. Because the hydrostatic pressure is balanced by the pressure drop across the interface:

$$\rho g h(r) = P(r) = \frac{\gamma h'(r)}{r\left(1+h'(r)^2\right)^{1/2}} + \frac{\gamma h''(r)}{\left(1+h'(r)^2\right)^{3/2}} \tag{12}$$

This equation must be solved numerically to solve for h(r). According to [40] provided "the meniscus is narrow relative to the diameter of the rod [membrane]," the maximum height that the meniscus could be, just before the membrane becomes submerged depends on the contact angle $\theta$, surface tension $\gamma$, density $\rho$ and gravity g, as:

$$h_{\max} = \left[2\left(\frac{\gamma}{\rho g}\right)(1-\cos\theta)\right]^{1/2}\left[1+\left(\frac{\gamma}{\rho g}\right)^{1/2}\frac{1}{R}\right]^{-1/2} \tag{13}$$

As the silicon surface becomes more oxidized, the contact angle decreases. The exact solution for h(r) and thus, via equation 8, the form of $\theta$(r) is not presented here (see [41]) since a numerical solution is not necessary to describe why the membranes float. Instead Figure 3.4 compares equations 8 and 13. In practice it should be possible to measure the value of $h_{max}$ using an optical profilometer. This measurement was unsuccessful because room air flow caused the membrane to drift along the surface but it could be accomplished in a more controlled environment.

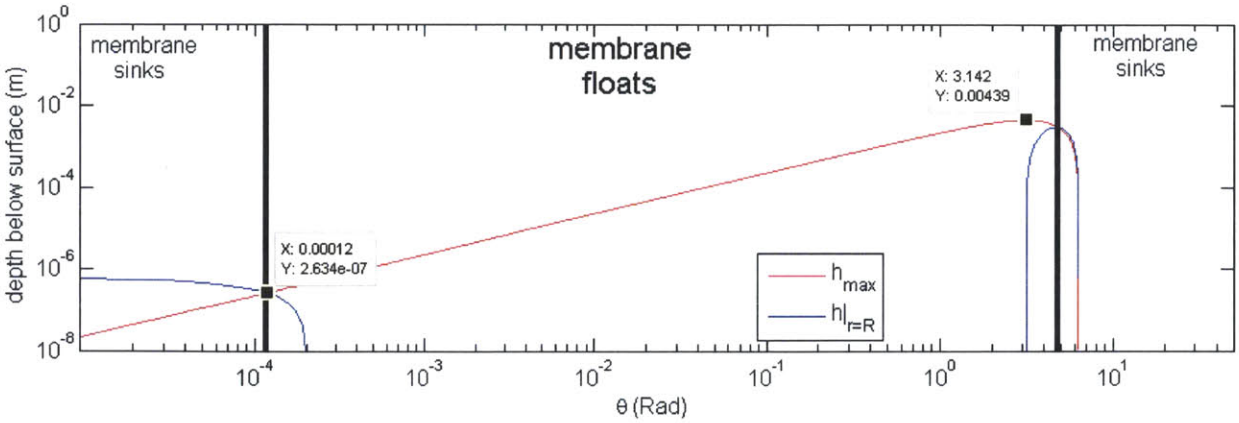


Figure 3.4 Range of contact angles for which a membrane floats in water. For a 47.5 ng membrane the first intersection of the two curves is the point at which the angle is large enough that meniscus height from equation 13 is less than the height equation 18 that the meniscus could be before the membrane is engulfed. As the angle increases the height of the membrane from equation 13 decreases until the contact angle grows larger than $\pi$. The plot covers a range over $2\pi$ for completeness though the meaning of a contact angle greater than $\pi$ is unclear.

Figure 3.3c depicts the hydrophilic membrane holes in cross-section with no applied pressure (following Figure 3.1). Aside from breaching the holes, another potential issue could arise if the apex of the meniscus protruded through the hole when pressure is applied during stacking. This could allow a small amount of water to form between the membrane and receiving substrate. If the contact angle were known within a hole, the height of the meniscus could be calculated from equation 12.

Surface tension is notable in that it holds the membrane up *and* pulls it flat. Thus, it can be used to constrain a membrane to somewhere on the surface of water or other aqueous solutions. For example, in the early process development toward releasing a membrane from an SOI wafer surface tension was used during the etch to peel a silicon device layer from the handle silicon: once the buried oxide was etched into an array of supporting posts, the sample was removed and reinserted at an angle relative to the surface so that the leading edge was at the surface. As the posts were etched, the device

layer peeled away from the handle silicon; unfortunately any small hand-twitch could crack the device layer and this was abandoned for the process described in Figure 2.23. Surface tension effects can also cause the membrane to move along on the surface of water since a gradient in chemical concentration at the surface drives the membrane normal to the gradient. This motion is readily observed with a floating membrane in water if a small amount of isopropanol is dripped onto a water surface. It is interesting to note how fast the membrane moves without breaking.

**iii Porosity**

Four different scenarios were observed that involve fluids flowing through the holes in the membrane. A silicon membrane freely-floating on water was transferred back to hydrofluoric acid after several days to remove new native oxide on the top surface. A single drop of hydrofluoric acid - smaller than the membrane - that was placed onto the upper surface permeated through the pattern of holes in the membrane. In another instance, a membrane on the surface of water did not submerge when small drop of water was put onto its top surface; even more interesting, the water also slowly seeped through it and once underneath it again, the membrane was flat with no rips in it. Another time, a membrane was dried onto a Mylar sheet with a 50 μm hole beneath the membrane and isopropanol that was pumped through the hole in the Mylar permeated through membrane to form a puddle on the surface. This was also observed with water when the silicon membrane spanned a 13 μm hole in a glass cover slip.

### iv Diffraction

Membranes drift about due to small perturbations of the fluid-air interface. As the membrane moves about, light diffracts from the pattern, which aids in visual inspection of the membranes and also provides information about the position and orientation of a membrane on the surface. As discussed in chapter 5, laser light diffracted from a membrane could enable multilevel alignment, however it is worth mentioning here, that when a patterned membrane is illuminated by fiber light the diffracted light provides some information about the membrane's flatness and quality (compare Figure 2.2 and Figure 3.5 c,d). In Figure 2.2, diffracted light from a buckled membrane helps reveal the bumpy surface. The freely-floating membrane appears flat in Figure 3.5c, but in Figure 3.5d the diffracted light reveals imperfections (cf. the green lines) in the membrane.

### v Extraneous observations

Surface tension forces are strong compared to the weight of the membrane and so flipping a membrane over is difficult. Once on the surface of water they tend to stay there, but if re-submerged maybe it could be possible to flip the membrane over. Once, a membrane was accidentally released along with a polymer coating (Shipley 1813 photoresist) and organic cleaning (acetone → methanol → isopropanol rinse) was attempted to eliminate the polymer. The membrane was carefully transferred to the bath of acetone, where it sunk. It drifted around beneath the surface of the acetone and once it was possible, the flipped membrane was picked up with a glass slide.

Though it is not yet obvious how, a mechanism to stack a membrane from its carrier to the receiving substrate will be needed. One candidate could be electrostatic detachment. A membrane that was held by Van-der Waals on a piece of glass was brought to within 500 μm of a dry polymer surface and it appeared to jump from the glass to stick to the plastic. Given the materials involved, this could have been an electrostatic interaction.

While neither of these last two experiments were repeated the observations (i) – (iv) suggested methods to manipulate membranes in preparation to stack them. In particular, they enabled the membranes to be transferred from one beaker of liquid to another, constrained from the edges and from underneath, moved along the surface of a liquid and finally dried down onto a target substrate. With these techniques, the next chapter will describe methods to directly remove the membrane from the surface of water by contacting it to a receiving substrate. Chapter 5 will describe methods to stack a membrane from a temporary carrier substrate onto the receiving substrate.

a. **Transfer from beaker to beaker**

Provided that membranes float on either hydrofluoric acid or deionized water, techniques were developed to transfer the membrane from one fluid to another because it is significantly easier to work with membranes in deionized water. Thin membranes are extremely compliant, so large objects like a hypodermic needle or fine-tip tweezers are inappropriate tools to use when trying to lift a membrane from one fluid to the next. In an early approach at free floating membranes, developed by Shabnam Ghadarghadr, the handle silicon of the SOI wafer was stripped using TMAH while the device layer

was protected by silicon dioxide films on either side. The sample was then lifted out of the TMAH in a Teflon basket (still submerged in aqueous TMAH) and carried to a beaker of deionized water where it was rinsed. Next the membrane was carried to a beaker of hydrofluoric acid where the silicon dioxide films were etched away. In the hydrofluoric acid, the different silicon dioxide films caused the resulting $SiO_2$ : Si : $SiO_2$ membrane to curl due to the stress imbalance in the oxide. The different layers of $SiO_2$ were etched at different rates, causing the silicon to initially curl up tighter than a pin and then to unravel. After unraveling the silicon was still submerged and was slowly drifting about, but as a portion of it approached the surface it appeared to jump to the surface.

This basket-based beaker-to-beaker transfer motivated her to introduce woven Teflon and Nylon screens. Comprised of interwoven filaments, these screens enabled a membrane to be transferred from one beaker to another (e.g. water in Figure 3.5). However, the relative thin (~1000x) membranes conformed to the large-scale undulation of the weave, sometimes forming small cracks that compromised the membranes upon release.

Fortunately, since the membranes float, they can also be lifted from underneath by fluid residing on a cover slide (see Figure 3.6). This prevents the membrane from accumulating wrinkles when it is transferred, however there is one caveat: if the slide is not parallel to the surface of the fluid, the membrane can spill off the slide before being removed from the surface. Regardless, a membrane constrained by surface tension

does not crack when supported by the fluid and thus the slide transfer technique became the predominant method for transferring a membrane between beakers.

The tradeoff between using the cover slide transfer as opposed to the screen transfer is that the fluid can evaporate from the slide and the membrane can thereby adhere to the slide, which can make the membrane difficult to recover, whereas with a screen the membrane can be re-released by immersing the screen into water. A membrane that needs to be stored dry could be carefully dried on a screen, whereas a membrane that needs to be cycled from bath to bath could be transported more easily with a slide.

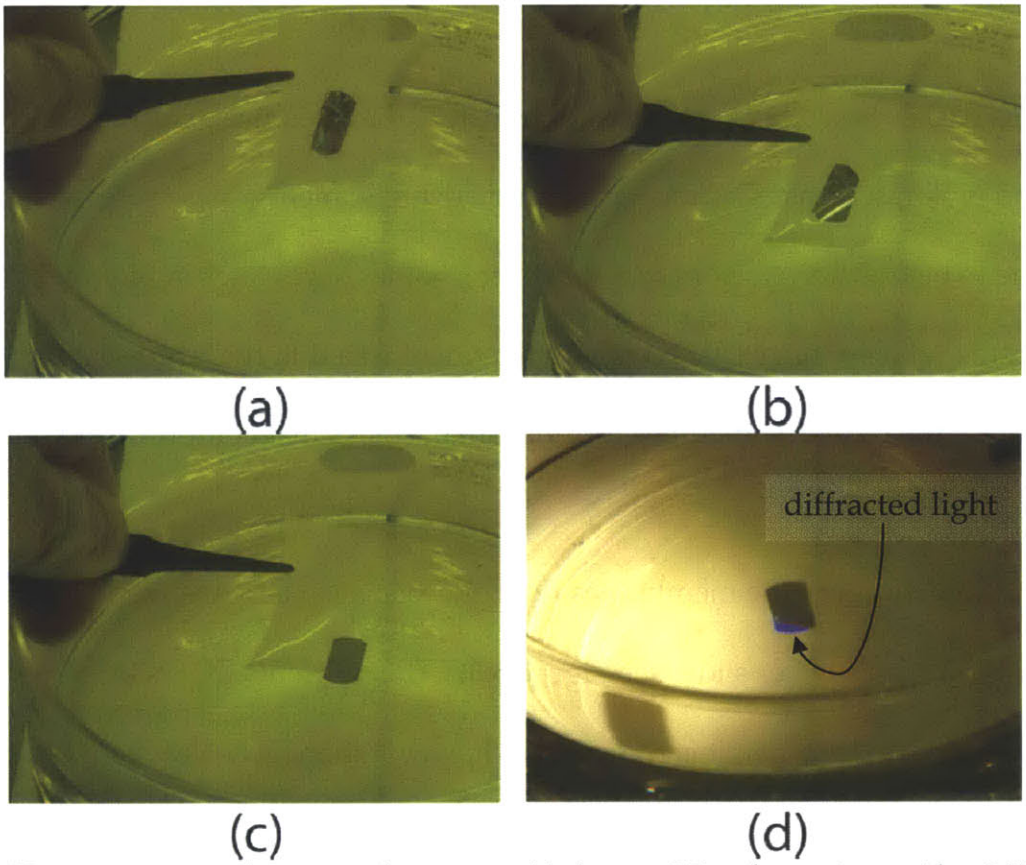


Figure 3.5 Woven screen membrane transfer process. (a) shows a 2.5 cm long × 1 cm wide × 340 nm thick buckled membrane supported on a nylon screen. (b) shows the same membrane as it is transferred onto the water surface. (c) shows the same membrane on the surface of the water. (d) shows the same membrane free-floating and diffracting blue and green light from fiber light illumination.

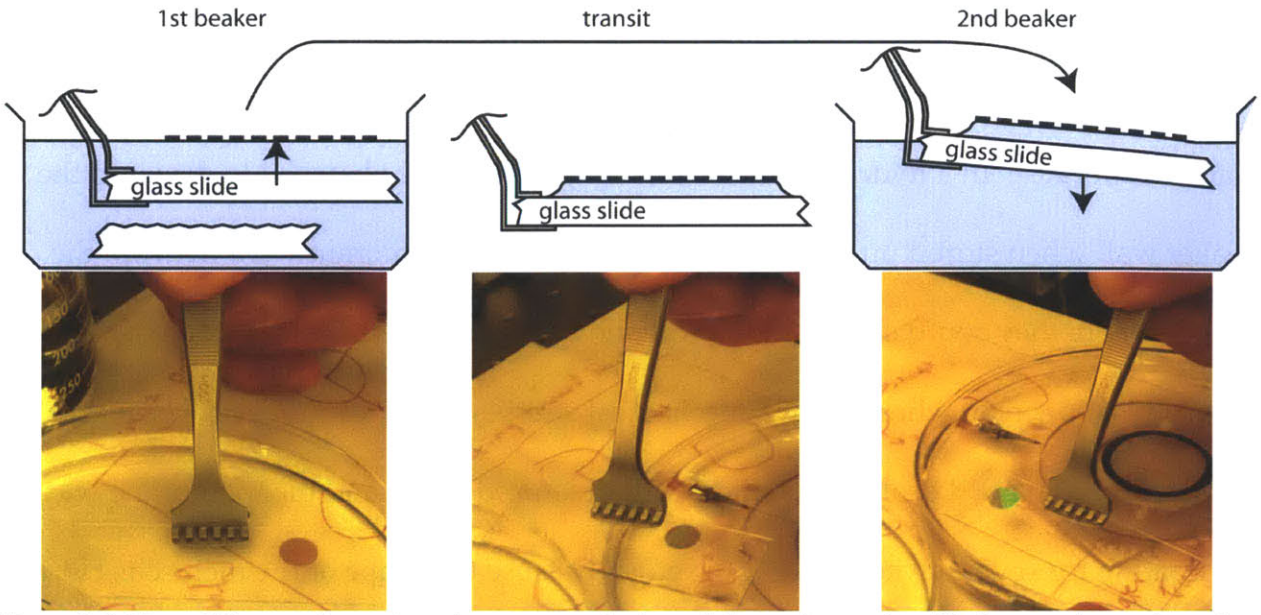

Figure 3.6 Glass slide membrane transfer process. A glass slide can be used to lift the membrane from the surface of water in order to transfer it to another beaker. The cover slide is kept parallel to the surface during removal and transit, but is then is tipped at a slight angle to deposit the membrane into the second beaker

b. **Motion within a beaker**

A carrier slide or a screen enables membrane transfer from beaker to beaker but once the membrane was removed again to the liquid surface it needed to be controlled. While surface tension is useful in that it confined a membrane to the liquid surface evaporation needs to be considered when the membrane was left floating for an extended period of time. According to Rayleigh [42], the water in a beaker "which, when protected from tremors and motes, is as flat as can be desired" has a flatness of 5%$\lambda$ in a 4-foot diameter beaker. Following the same reasoning and neglecting the meniscus around the edge of a 20-cm-diameter beaker, the curvature of a water surface due to the earth's gravity alone would be cause a deviation of ~1 nm at the apex (center) of the beaker.

Of course, the meniscus at edge of the beaker cannot be neglected. Figure 3.7 shows how the membrane interacts with a hydrophobic and hydrophilic beaker as water evaporates. In a hydrophilic beaker, membranes were observed to dry onto the beaker wall when stored unattended. Instead of storing membranes in a hydrophilic beaker where they could adhere to the wall, on a cover slide where they could dry out, or on a plastic screen where electro-mechanical stresses could lead to cracks or worse, a plastic Rubbermaid™ beaker was filled with deionized water and the membrane was left floating for several weeks. Near the edge, because the shape of the meniscus curves down evaporation does not allow the membrane to adhere to the beaker wall (see Figure 3.7).

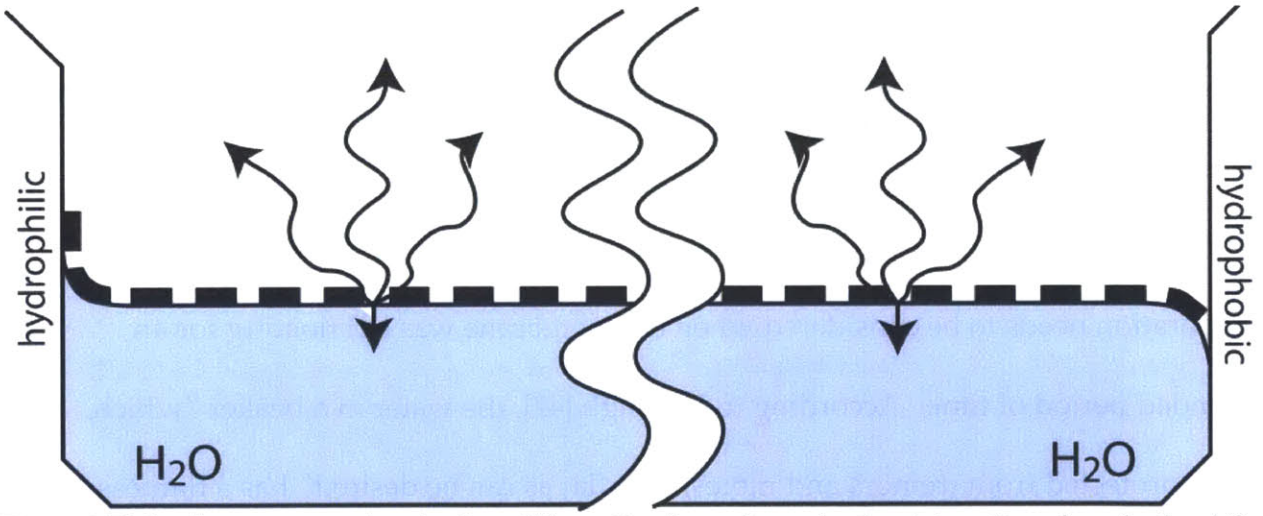


Figure 3.7 Membrane storage in a beaker. Schematic of membrane-beaker interactions for a hydrophilic wall (left) and a hydrophobic wall (right). Water evaporates and as the water level decreases, the membrane dries onto the wall of the hydrophilic beaker. In the hydrophobic beaker, to go into contact the membrane would need to roll up onto the wall of the beaker instead of being dragged onto it as in the hydrophilic case.

Clearly, the membrane does not just sit still in a beaker but rather would drift around the surface. The interaction of the membrane and beaker wall hinted at a way to move a membrane. In Figure 3.8, instead of the fixed wall of a beaker, a dipstick was

used to push the membrane about. A dipstick can be the tip of a tweezers, a glass or plastic pipette or any other impermeable object that is inserted into the fluid within a few mm of the membrane to create a meniscus that interacts with the nearby membrane. As the dipstick is moved along the surface, the meniscus can be used to push the membrane along with it. It is important though, not to move the dipstick too quickly because the membrane responds to the meniscus it generates and not directly to the dipstick.

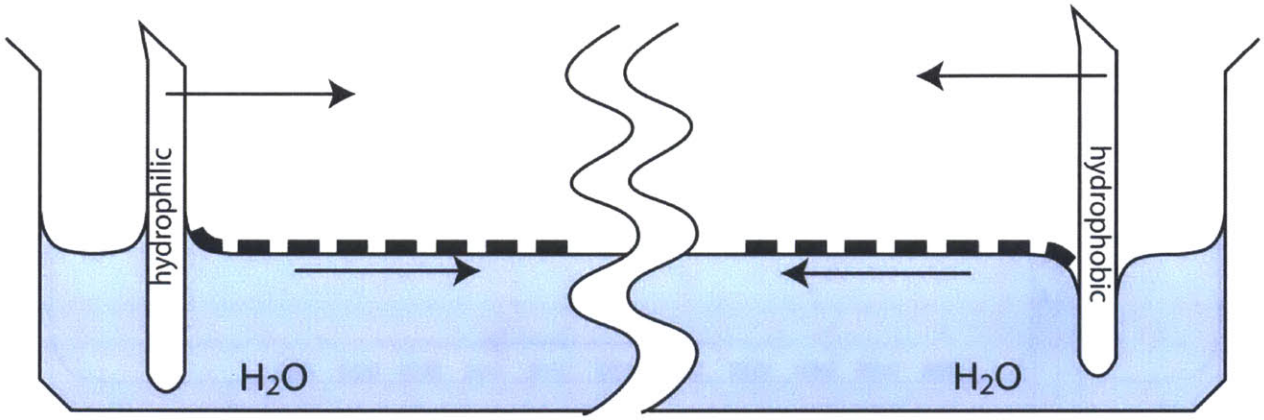


Figure 3.8 A membrane moved by a *dipstick*. A dipstick inserted into the water causes a meniscus to form. The meniscus followed the dipstick and allows the membrane to be moved without touching the dipstick. Both hydrophobic and hydrophilic dipsticks can be used to push the membrane, though as described in Figure 3.7, the hydrophilic dipstick allows the membrane to stick to the dipstick, which is undesirable.

More generally, techniques to move the membrane follow the theme of locally changing the meniscus to induce a force that moves the membrane. Figure 3.9 shows a refinement of the dipstick approach, where a wick is used instead to move the membrane and Figure 3.10 shows how to move the membrane by depressing the meniscus with airflow.

In Figure 3.9, a wick inserted into the fluid has a different effect on the membrane than the dipstick. It was observed that wicking the water initially causes the

membrane to move *away* from the wick due to the raised meniscus, however once the water level reduced sufficiently that the meniscus height decreased, the membrane would flow with the water current *toward* the wick. Thus the wick serves three functions depending on how it is used: it pushes a membrane away, slowly dries the water and pulls the membrane toward the wick. It is much more useful than a dipstick, since positioning the membrane typically went along with removing the bulk fluid. For instance, much of the stacking work in chapter 5 required drying the membrane onto a carrier substrate during which wicking away the water was a critical step.

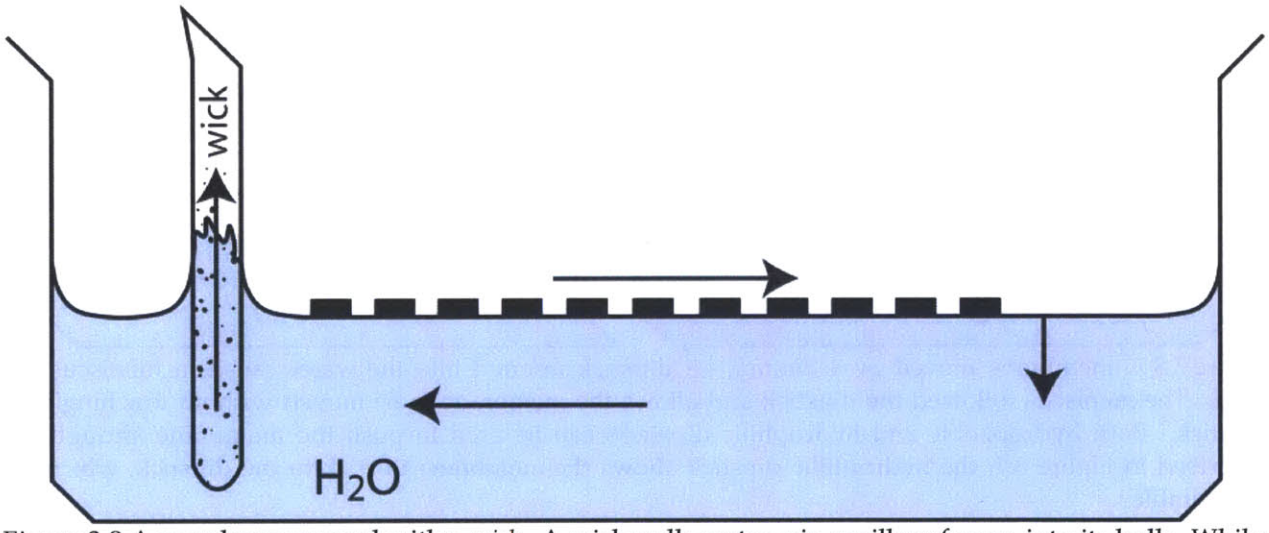


Figure 3.9 A membrane moved with a *wick*. A wick pulls water, via capillary forces, into its bulk. While the wick slowly removed water from nearby membranes the meniscus that forms to the sick pushes the membrane away. If enough water is removed, the membrane begins to flow back toward the wick so care is necessary to keep the membrane from accidentally attaching to it.

In some circumstances, particularly when there is not a lot of space available, neither a dipstick nor a wick was a practical actuator for positioning a membrane. Figure 3.10 shows an alternative method to move the membrane that uses nitrogen from an air nozzle to push and rotate the membrane. Due to the small space requirements, a 75 mm long metal air nozzle made from a thin metal tube was attached to house $N_2$

supply. This custom air gun was able to access the small working areas used during stacking and the meter valve controlled the flow rate of the $N_2$. Given the scales involved, only a small flow rate was needed, so the nozzle was submerged into a beaker of water and the valve opened very slightly. While submerged if more than one bubble at a time left the nozzle it was too aggressive. Then, holding the nozzle far away (~250 mm) from the membrane was seen to cause it to move more slowly (rotation <1 Hz) than if the nozzle was close (>10 Hz at 100mm), though these rates also depend on the in-plane angle of the nozzle with respect to the membrane tangent and the tilt of the nozzle from the water surface.

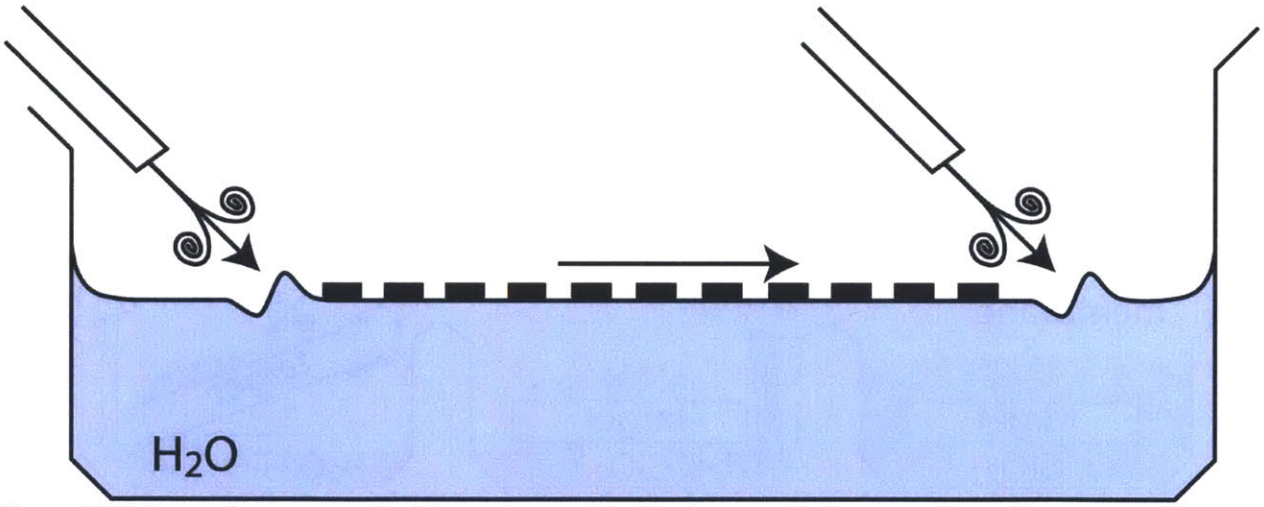


Figure 3.10 A membrane moved with an *air gun*. Gentle air currents from a custom nitrogen gun depress the air-water interface warping the meniscus as shown. By pointing it at an angle to the surface, the membrane can be pushed, pulled or rotated on the surface.

One of the most interesting aspects of this work was learning how to manipulate structures this delicate. Surface tension performs an amazing feat – by keeping it confined to the surface of the fluid, the requisite of holding the membrane with a frame (see Figure 1.2) is eliminated – however by conforming to the surface it is also difficult to remove. In order to stack the membranes onto the receiving substrate, methods

needed to be developed to allow their removal from the water surface. The simplest of these techniques, where the membrane is picked up from underneath, is presented next.

c. **Membrane transfer to a substrate**

Figure 3.11 shows one way a free floating membrane may be placed onto a target substrate. Illustrated in Figure 3.11a, it floats in a beaker above the target substrate and then in Figure 3.11b, as water is drained from the beaker with a syringe, it is left floating on the target substrate. As water evaporates the membrane's edge first approaches the target but before it contacts the surface, the target is slightly tilted as in Figure 3.11c so that only the trailing edge of the membrane contacts the target and gentle air flow dries the remainder down without wrinkles. This technique circumvents wrinkle formation because by returning the target to the horizontal orientation capillary forces delaminate wrinkled regions of the membrane from the target.

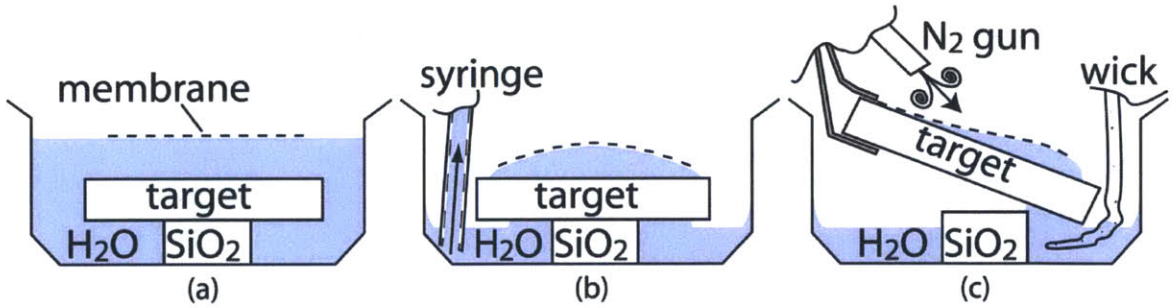


Figure 3.11 'Tilt-drying' process to dry a membrane onto a handle substrate. In (a), the membrane is freely-floating above a pedestal comprising a target glass substrate above a narrow glass spacer. (b) A syringe draws out the water, leaving the membrane bulged on a water puddle on the target substrate. (c) As the water dries (either by evaporation or assisted with a wick) the membrane approaches the target. When the membrane gets close to the target, the two are slightly tipped causing a bead of water to develop on one side (the right in the figure). The membrane-target contact is initiated from the left and gentle air flow causes the contact to propagate toward the right. As water is being driven out from underneath, the onset of wrinkles are stopped by counter-tipping the target to delaminate the membrane.

The virtue of transferring the membrane to a substrate following this approach is that it is possible to eliminate the formation of wrinkles by delaminating and then re-

laminating it until it lies flat. Membrane stacking via this approach is possible but extending it to a process that incorporates precision alignment would require precise control over the ambient environment, the tilt of the target substrate and the membrane's lateral and rotational position. In principle this could be accomplished with a dedicated tool that isolates the membrane and target from the ambient environment while ISPI-like alignment scopes control both the tilt of the target substrate and the position of the membrane relative to the target using airflow and a tip/tilt stage. However, the ISPI scheme depends on the reflections from the second surface (i.e. the target in this case) so the microscopes would need to tip/tilt along with the target substrate; this complicates the implementation and simpler approaches to stacking and alignment will be investigated in the following chapters. The stacking process described in the next chapter differs from this process. Instead of using water to pull the membrane into contact with the target, a scheme in which Van-der Waals adhesion mediates the contact to avoid water between the receiving substrate and membrane is desirable.

# Chapter 4. Membrane Stacking

The previous chapter discussed the hydrostatics of floating membranes and introduced several handling techniques based on locally modifying the water surface to indirectly manipulate membranes. This chapter leverages those handling methods to enable membrane stacking techniques. The end result of experimenting with different stacking configurations was a process where membranes were temporarily supported by an adhesive that sublimated and evaporated away to detach the stacked membranes. However the path to this achievement began with stacking free-floating membranes.

Throughout much of the development of the stacking process it was presumed that these membranes remained hydrophobic because the mechanism by which they floated was subtle - water spiders with hydrophilic feet would sink! Being deceived by the elegance of surface tension's ability to pull membranes flat, the first of several experiments was postulated.

***Hypothesis 1**: a bubble introduced beneath a free-floating membrane could be used to lift and stack it onto a receiving substrate*

Experiment 1. Bubble-initiated membrane stacking from water surface

The stacking approach described in this section benefits from its simplicity. It is distinct from the techniques described in [19] - [24] where membranes were transferred from an adhesive-coated carrier substrate and from the approach described in [25] where free-standing nitride membranes were supported around their periphery by a solid frame that was removed after cleaving the connective tethers. Instead the

membranes here were transferred directly from the surface of water to the receiving substrate. The main result of this experiment was five stacked membranes; the conclusion was that the free surface of water would lead to detachment of the membranes and that bubbles formed beneath the stacked membrane could drive the water away.

After its release to the surface of hydrofluoric acid, the membrane was rinsed clean and then transferred to a stacking apparatus. Then water lifted the membrane to approach the receiving substrate. This introduced very little pressure (cf. Figure 3.2) across the membrane holes because it was floating throughout. However there were some challenges to be overcome in getting the membrane to stick to the receiving substrate. Capillary forces pulled water between the membrane and receiving substrate when the surface of the water contacted the receiving substrate. Also, if the membrane initially contacts the receiving substrate in more than one point, buckles would form.

Figure 4.1 illustrates the first of these challenges. In it, a glass receiving substrate is depicted above a floating membrane. Water from the inlet lifted it upwards toward the receiving substrate; however when the water contacted the receiving substrate before the membrane capillary action would prohibit the membrane sticking to it. Then when the receiving substrate was removed the membrane would follow the water back down to the beaker.

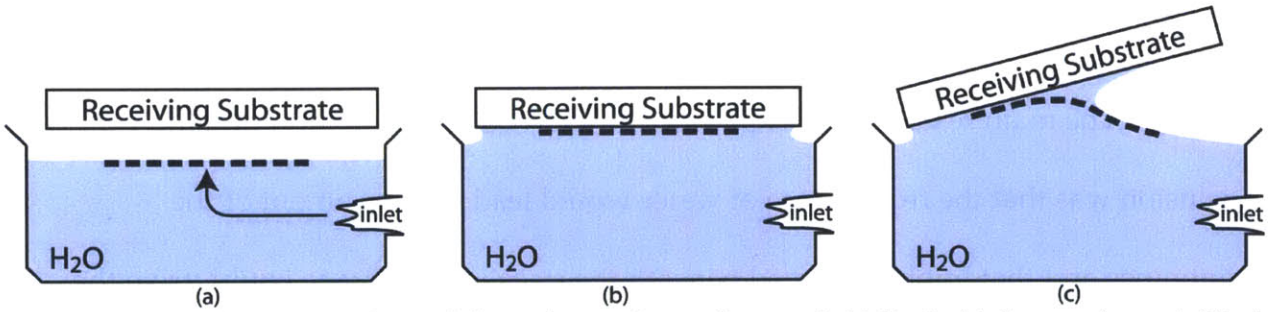


Figure 4.1 A free floating membrane follows the meniscus of water. Initially, in (a) the membrane is lifted with water flow from the inlet. But in (b) the water forms a meniscus with the receiving substrate and capillary forces draw water between the membrane and receiving substrate. When the receiving substrate is removed in (c) the membrane follows the water away from the receiving substrate.

Consider Figure 4.2 where instead of merely free floating, the membrane is confined to the interior of an annulus. In Figure 4.2a, the meniscus of the water is pinned to the top corner of the annulus completely confining the membrane within the annulus. In Figure 4.2b water added from the inlet lifts the membrane upward until it is level with the top of the annulus. Then in Figure 4.2c, because the water is pinned by the corner of the annulus, the membrane bulges upward on the curved meniscus – perhaps it could contact a receiving substrate first. The annulus helps confine the membrane and also reduces the free surface area of the water.

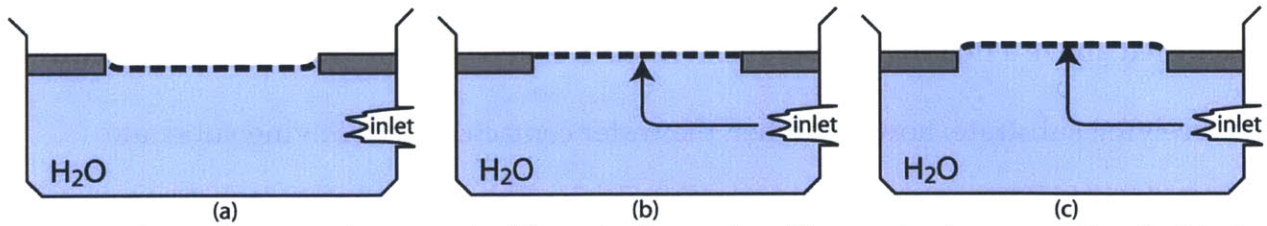


Figure 4.2 A membrane can be constrained by a plastic annulus. The annulus in cross-section depicts the corner effect: (a) a low water level creates an upward curving meniscus that corrals the membrane. (b) The water level is increased until the meniscus flattens out. (c) Addition of more water causes the meniscus to curve downwards, lifting the membrane out of the corral. Addition of more water eventually causes the water to spill outward from the corral.

In this experiment the annulus was a 1-cm-diameter hole drilled into a 3.125-mm-thick polyvinyl chloride (PVC) disk. Figure 4.3a shows the design of the PVC-based stacking apparatus in cross-section. The chamber was filled with water from the

source and was drained out the bottom; in addition to three #6-80 leveling screws, view ports were incorporated to allow viewing of the experiments from the water level. At the water line, the chamber was covered with the PVC annulus which was clamped in place with a PVC c-clamp (not shown). Figure 4.3b shows the apparatus loaded with a floating membrane. The membrane, transferred into the apparatus from a Teflon screen, was deposited onto the surface of water that had intentionally overflowed from the annulus. Once floating, it was positioned with a dipstick (the tip of a tweezers) over the annulus and the water was drained until the membrane was corralled by the annulus. In the center of the annulus, the membrane is shown diffracting room light. Careful examination of Figure 4.3b shows this particular membrane had developed a crack during the Teflon-screen transfer step.

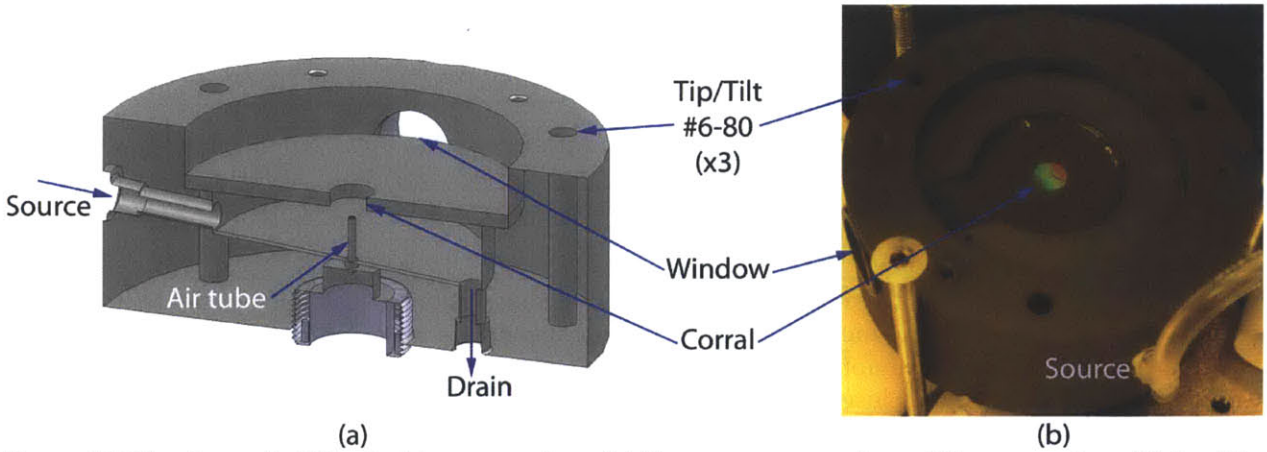


Figure 4.3 Membrane bubble-stacking apparatus. (a) Shows a cross-section of the apparatus. Water fills the chamber from the source; the drain is stopped until needed. Three #6-80 TPI screws provided tip/tilt control during experiments and view ports were included to observe the experiment from the water line. (b) The physical apparatus loaded with a membrane. The corral is used to hold the membrane as it freely floats on the surface of water. The apparatus was secured to the table with 3 hex bolts, one of which is visible on the bottom left.

In Figure 4.4 the first step of the process began with a membrane held flat in the center of the annulus. In the second step, an air bubble beneath the membrane

displaced it up into contact with the receiving substrate. In the third step, the amount of water displaced by the bubble is enough that capillary forces have drawn it into the space between the annulus and receiving substrate and the membrane is water-bonded to the receiving substrate. Then in the fourth step, a wick inserted into this space breaks the meniscus of water to leave the membrane on the receiving substrate.

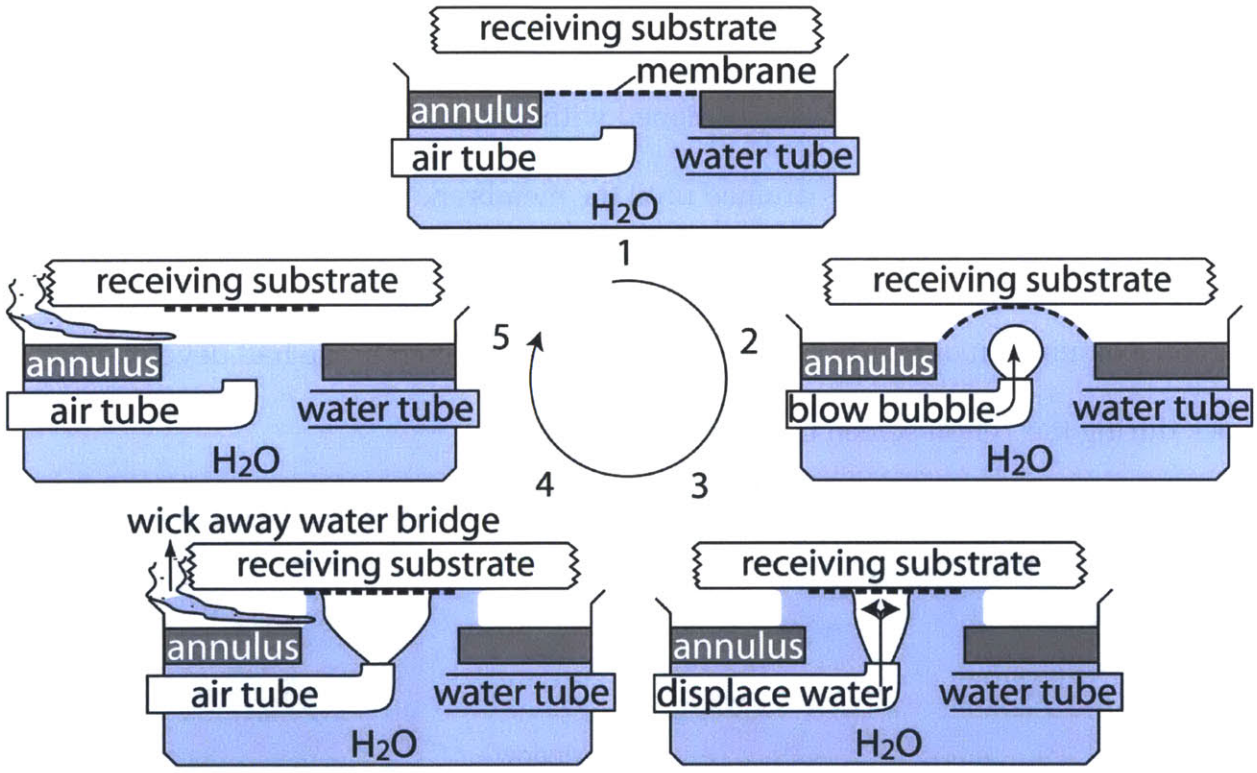


Figure 4.4 Membrane stacking from a fluid surface. At first, the membrane is floating in the center of the annulus. A bubble beneath the membrane in the second step brings up into contact with the receiving substrate. In the third step the bubble is enlarged to displace water into the region between the receiving substrate and annulus. A wick inserted between the two drew water away from the membrane where it remained stacked.

There were numerous issues that could not be addressed by this apparatus. The annulus was not sealed, so when water pushed the membrane up, it also leaked around the edge of the annulus to enter into the stacking area. Instead of having control over the gap between the receiving substrate and annulus it was set by the thickness of the c-

clamp[3], with which ~0.1 ml of displaced water was required to lift the membrane into contact with the receiving substrate. The membranes were occasionally mismatched in size and the annulus could not adapt, which meant that the capillary problem of Figure 4.1 was not fully addressed. Figure 4.5 shows that despite these issues, it was possible to stack 5 membranes using this apparatus.

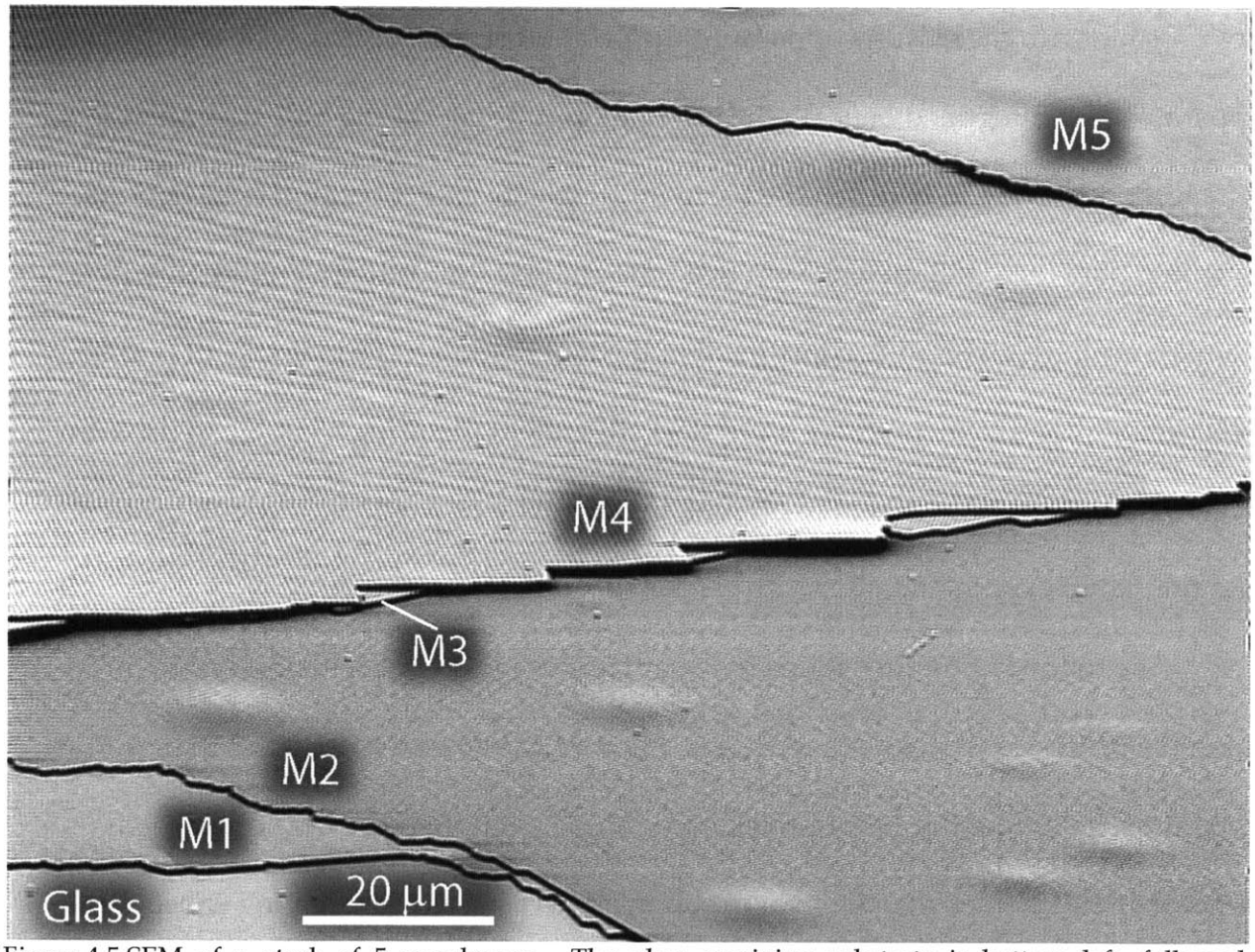


Figure 4.5 SEM of a stack of 5 membranes. The glass receiving substrate is bottom left, followed diagonally by the subsequent membrane layers, M1 - M5. Notice that the moiré generated by the scan rate of the e-beam highlights particles between layers as curving fringes, e.g. center of M4.

[3] The receiving substrate, a glass cover slip, was mounted onto a 75-mm-long glass cover slide, which spanned across the c-clamp. To reduce the spacing between the cover slip and annulus foam tape brought the cover slip to within 1.5 mm of gap.

***Hypothesis 2**: if the annulus was adjustable (and sealed properly) and the gap between annulus and receiving substrate was reduced then membranes might be stacked without requiring a bubble to drive away water.*

Experiment 2. Membrane stacking directly from water surface

The second hypothesis required two new capabilities. Adjustments to the gap between annulus and receiving substrate as well as the inner radius of the annulus were not possible with the existing apparatus and so another was created. The new apparatus was integrated beneath the existing tip/tilt stage of the ISPI alignment tool, which allowed the gap between the receiving substrate and apparatus to be decreased to within parts of a millimeter. Moreover, the annular PVC ring was replaced with a stainless steel iris to provide adjustment of the inner radius. The main result of this experiment was two membranes were stacked without requiring a bubble to drive away water; the conclusion was that freely-floating membranes would be difficult to align and this led to experimentation with carrier substrates.

The following modifications to the apparatus indeed made it possible to improve upon the process described in Figure 4.4. Figure 4.6a shows the design of the apparatus, including the 19-mm-thick base, adapter and iris. The iris housing was larger than the 25-mm-diameter cover slip that was used as the receiving substrate, which allowed arbitrarily small gaps between the membrane and receiving substrate. This capability facilitated contact between the membrane and receiving substrate without significant capillary action. Figure 4.6b shows the apparatus loaded with a membrane prior to being inserted beneath the tripod stage.

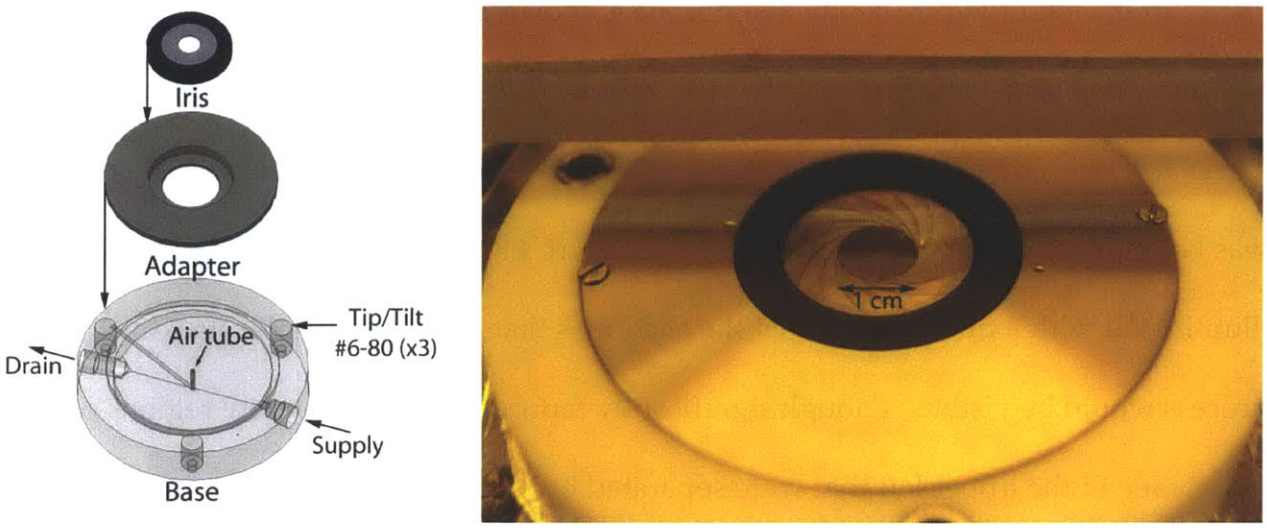


Figure 4.6 Iris-based membrane stacking apparatus. (a) Blown up design of second membrane stacking apparatus illustrating the base, adapter and adjustable iris. Water supplied from the right could be drained from the left. Tip/tilt screw were included to level the apparatus. Though depicted in (a) the air tube was not used. (b) The 1-cm-diameter membrane is shown floating inside the aperture of the iris.

Figure 4.7 shows the simplified membrane stacking process that incorporated the iris. In Figure 4.7a the membrane is confined to the center of the iris, however this time the gap between the iris leaves and receiving substrate was less than a millimeter. In Figure 4.7b a small amount of water (~0.05 ml) initiated contact between the membrane and receiving substrate and in Figure 4.7c additional water brought the remainder into contact. As more water was added, it again overflowed beyond the membrane but this time when removing the membrane and receiving substrate a bubble was unnecessary.

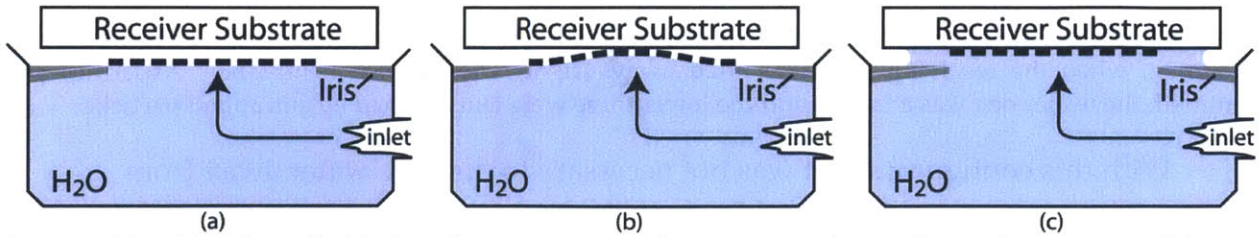


Figure 4.7 Stacking from the iris-based apparatus. (a) The membrane begins flat in the aperture of the iris and (b) contacts the receiving substrate in the center; no meniscus forms. (c) Additional water brings the rest of the membrane into contact.

In the left of Figure 4.8 the membrane is shown going into contact with the receiving substrate. The glass receiving substrate visible in close proximity to the iris leaves is mounted via foam tape and glass slides to a 76.2 mm diameter glass ring that was held in the tip/tilt stage. In the right of Figure 4.8 the patterned membrane is illuminated with a fiber light so that the asperities that resulted from the stacking process would be visible. Though significantly reduced, there were a few regions of the membrane in the upper left that were separated by particles from the receiving substrate and along the very top a buckle had formed.

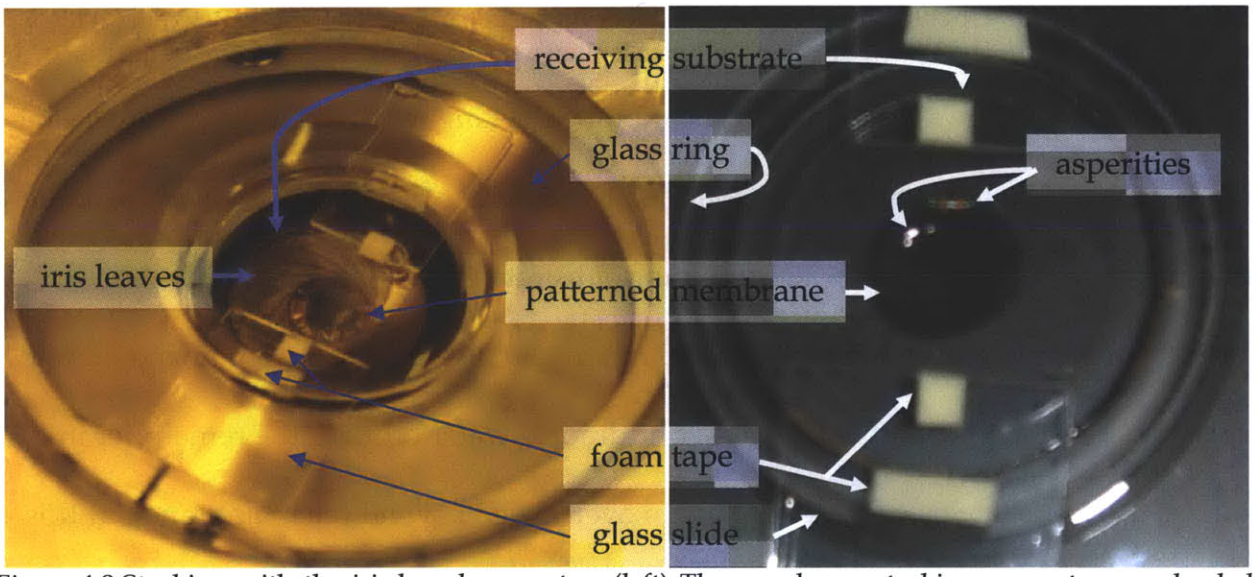


Figure 4.8 Stacking with the iris-based apparatus. (left) The membrane stacking apparatus was loaded beneath the receiving substrate and the membrane bulged upward toward it. The receiving substrate, mounted with foam tape and glass slides to the glass ring, was positioned with the tip/tilt stage to a gap of less than < 1 mm away from the iris leaves. During stacking the resulting meniscus did not detach the membrane when the receiving substrate lifted away. (right) The stacked membrane. Asperities are identified, the upper one was a buckle and the lower three were tents formed by entrapped particles.

With this configuration, it was not necessary to displace water away from underneath the membrane with a bubble. Presumably, the leaves of the iris sufficiently reduced the free surface of water to allow the membrane's attraction to the receiving substrate to dominate any detachment force applied when they were removed from the

apparatus. Moreover, with the iris much larger areas of intimate contact formed between the stacked membrane and receiving substrate.

Figure 4.9 shows a stack of two membranes using this apparatus. The membranes were smaller than 1-cm and had a rectangular shape[4]. In order to reduce the free surface of the water, before loading the receiving substrate, each membrane was lifted out of the iris by overfilling the annulus. The iris diameter was reduced so that when the water level was again decreased the corners of the membrane landed on the leaves of the iris and became *pinned* in place. Thus pinned, rotational alignment was attempted by observing diffraction from the pinned membrane on the iris and the previously stacked membrane. In Figure 4.9a, the optical micrograph was taken at a magnification of 100x. The fringes are clearly visible and their Fourier transform is shown in Figure 4.9b; the high frequency components along the diagonals most likely correspond to the fine grid of the top membrane. The fringe period is 5 μm and this corresponds to a rotation angle of 0.143 Rad.

[4] These membranes were released directly from rectangular SOI samples whereby the patterned silicon was first partially undercut in hydrofluoric acid, after which the samples were removed and then reinserted at an angle to use surface tension to peel off the device layer from the handle.

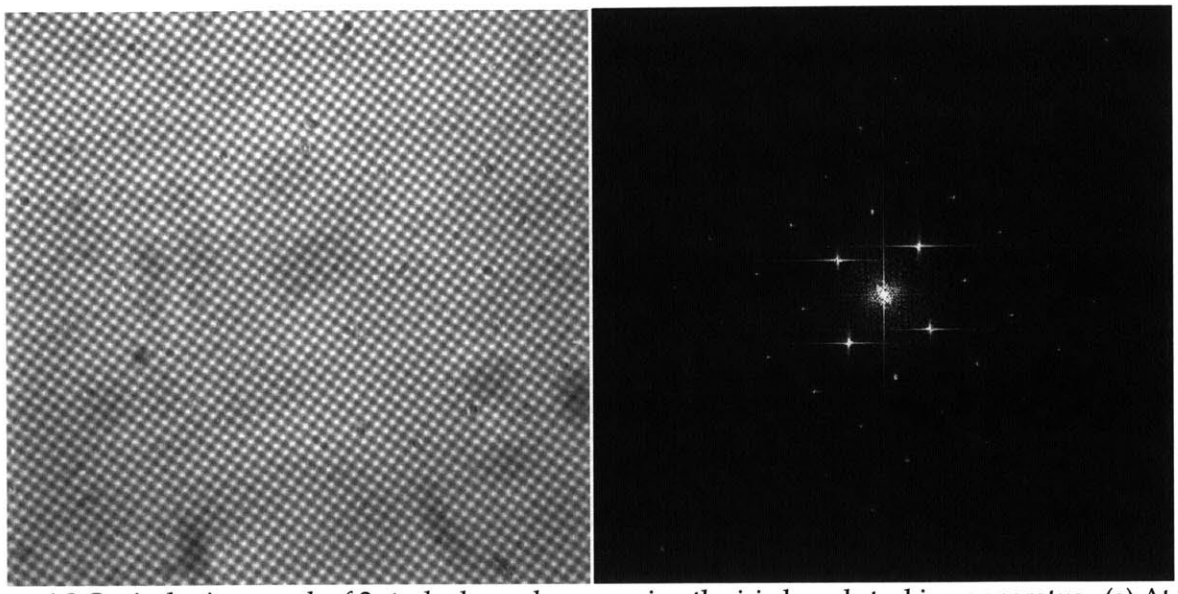

Figure 4.9 Optical micrograph of 2 stacked membranes using the iris-based stacking apparatus. (a) At 10x magnification, moiré fringes are observed. The fringe period is 5 μm which, assuming equal-period grid patterns, corresponds to an angle of 0.143 Rad. (b) The spatial frequencies of the micrograph in (a).

When the membrane was pinned in place it was no longer flat but rather conformed to the leaves of the iris. However, the membrane no longer drifted about and this led to another hypothesis.

***Hypothesis** 3: A stationary membrane supported by a flat carrier surface could be stacked if the carrier contained a hole from which water could release the membrane.*

Experiment 3. Membrane stacking from a glass cover slip

To explore the third hypothesis another apparatus was built and an experiment performed. This experiment did not lead to successfully stacked membranes; the conclusion was that water permeated the holes in the membrane before its adhesion to the carrier was overcome.

Elimination of the bubble generator greatly simplified the experimental design. A groove cut half-way into a 76.2-mm-diameter, 0.5-mm-thick glass wafer housed a 33-

gauge syringe needle. Then an 0211-glass cover slip was milled with laser ablation (248-nm-light) to have a 13-μm-diameter central hole that was positioned over the end of the syringe needle. The cover slip was glued to the glass base with uv-cure epoxy (Loctite #3104) and the diesaw groove was sealed with Unibond wax so that water from the syringe would flow through the hole in the cover slip to potentially push the membrane upwards to contact the receiving substrate as illustrated in Figure 4.10.

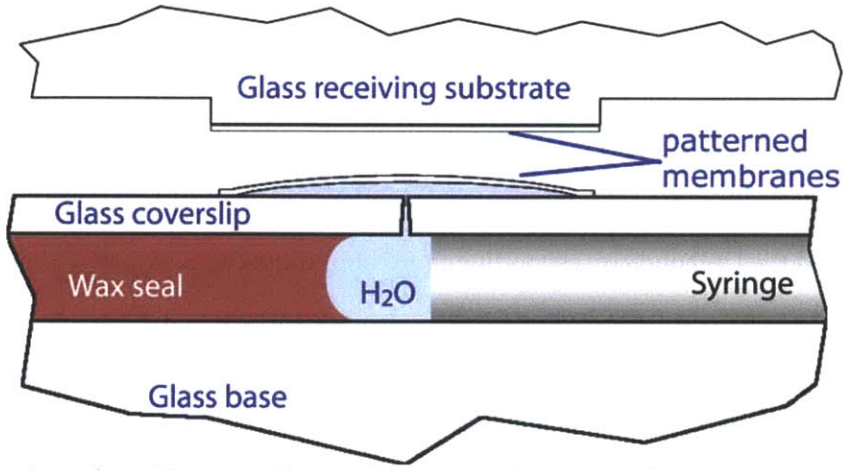


Figure 4.10 Illustration of stacking membranes from a rigid carrier substrate. Water from the syringe detaches the membrane from the glass cover slip in order to lift the membrane toward the glass receiving substrate.

Figure 4.11 shows a membrane that was dried onto the glass cover slip of this apparatus following the tilt-drying technique described in Figure 3.11. In Figure 4.11a the membrane supported on the glass carrier is ready to be stacked. Then while attempting to stack the membrane in Figure 4.11b water pressure was observed to compress air that was trapped within the grove. This provided a rough estimate of the applied pressure as described in Figure 4.12.

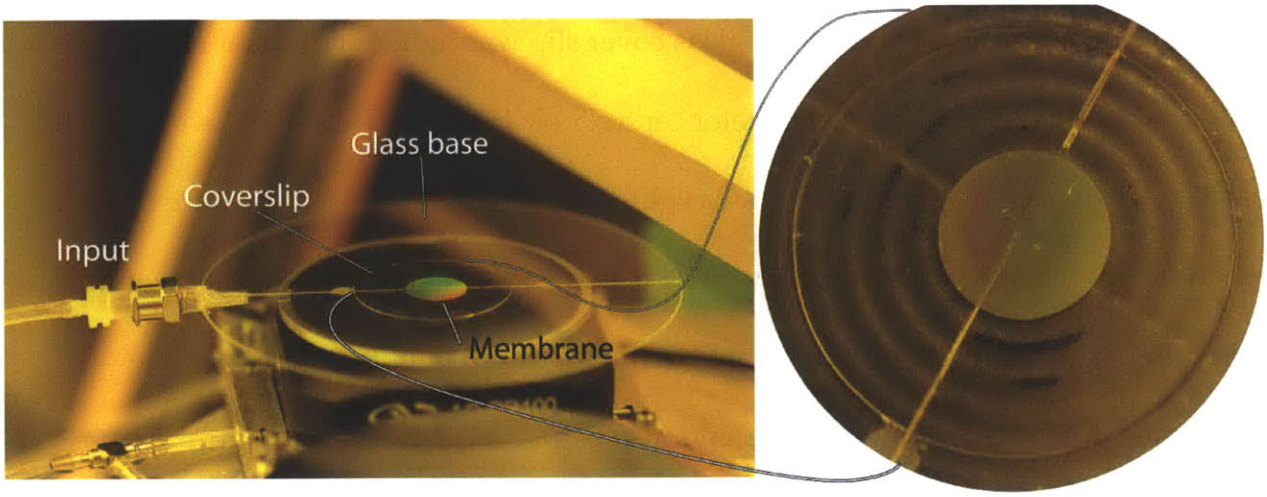


Figure 4.11 A membrane on the rigid fluid carrier. In (a) the membrane has been tilt-dried onto the cover slip and is shown diffracting room light. In (b) the membrane is shown from the top during a stacking experiment. There are three small wrinkles in the membrane, two by the syringe port and one in the upper right in addition to a few randomly distributed particles. Air bubbles between the glass base and cover slip are visible near the end of the syringe needle and also in the channel between the upper edge of the membrane and edge of the Unibond wax seal. The size accounts for ~16% of the volume between the end of the syringe and the Unibond corresponding to ~ 5 atm of applied pressure.

Something unexpected occurred when, instead of releasing the membrane, water permeated the 410-nm-diameter holes in the membrane to appear as a small droplet on the top surface. In this experiment, the air volume decreased by ~6x to form the two bubbles visible in Figure 4.11b. The ideal gas law at constant temperature indicates a change in pressure of ~500 KPa was applied to compress the bubbles.

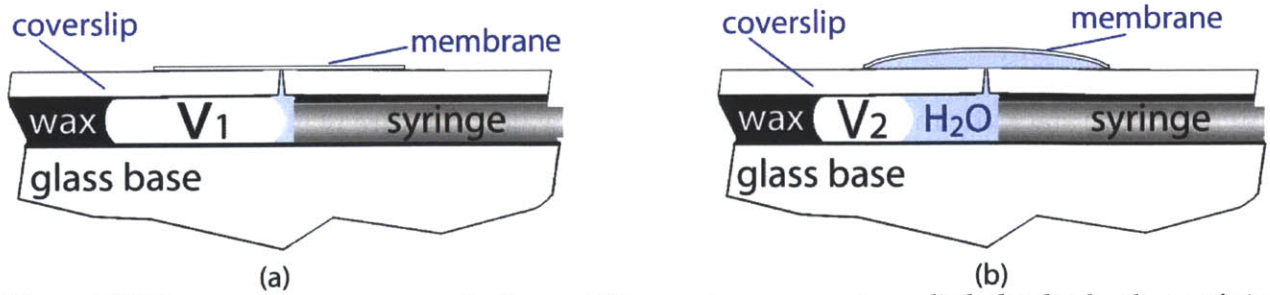


Figure 4.12 The pressure measurement scheme. When water pressure is applied, the dead volume of air between the syringe outlet and wax plug decreases from V1 in (a) to V2 in (b). With enough pressure a membrane with a fine grid of holes could detach as depicted in (b). However, if the adhesion force is larger than the force to push water through the membrane holes, then before the membrane released a droplet of water would form on the topside of the membrane.

It is possible that the adhesion of the membrane to the glass surface was greater than the pressure required to push water through the holes in the silicon membrane. In support of this, the authors in [43] measured that at 40% relative humidity 5.5 μN were required to detach an oxidized 2-μm-diameter flat silicon surface from smooth glass. Converted, the adhesion of 1.75 MPa is larger than the observed pressure difference (~0.5 MPa in Figure 4.11b) and is also larger than that predicted by Figure 3.2 to form a spherical droplet thus water was pushed through the holes on the membrane before it detached from the glass carrier.

There are ways to reduce the adhesion between the membrane and carrier substrate. The surface can be changed, either by roughening it or by applying a monolayer, or the contact area can be reduced. While roughening the surface could decrease the adhesion by an order of magnitude [43] the smoothness of the glass is desirable for the interferometric alignment (discussed in chapter 5), so instead a monolayer was sought. Recalling how easily the membrane detached from the Teflon screen (Figure 3.5a), it was surmised that the hydrophilic membranes' adhesion to the carrier could be reduced if the carrier surface was made more hydrophobic through application of a monolayer. HMDS was chosen because when it forms a monolayer, it terminates a glass surface with non-polar methyl groups, which convert the surface from hydrophilic to hydrophobic. Unfortunately, even with HMDS, before the membranes completely detached from the carrier water would leak to form between the carrier surface and the receiving substrate. Moreover, while HMDS reduced the

adhesion between the carrier and a membrane, reuse affected the surface modification – membranes became less likely to detach.

***Hypothesis 4**: The adhesion to the carrier surface could be reduced if the surface was perforated with a dense pattern of release holes.*

Experiment 4. Membrane stacking from a $SiN_x$ screen

A more robust approach than surface modification should be to reduce the contact area by perforating the carrier surface with a dense pattern of small holes. A modification was made to the apparatus to test this. The main result of this experiment was the wrinkle-free stacking of a membrane; however the conclusion was that water ultimately caused more problems than it solved especially since it would not extend to the stacking of disjoined membranes.

The 125-μm-thick glass cover slip was not an ideal substrate in this case because it would take a long time to laser ablate a dense pattern of holes (~40 s/hole). A free-standing $SiN_x$ membrane mounted to a Pyrex ring was perforated instead. The 3-cm-diameter, 1-μm-thick $SiN_x$ membrane was cleaned, patterned lithographically and then etched to form a dense array of water holes. Deferring the fabrication details for a moment (see appendix) the nitride was patterned with an array of 100-μm-diameter holes on a 300-μm-pitch grid to form the flat perforated *screen*. Figure 4.13 shows how this screen could be used for stacking. In Figure 4.13a by reducing the water level the free floating membrane is dried onto the screen and then in Figure 4.13b the screen is

positioned beneath the receiving substrate and water flows through it to stack the membrane onto the receiving substrate.

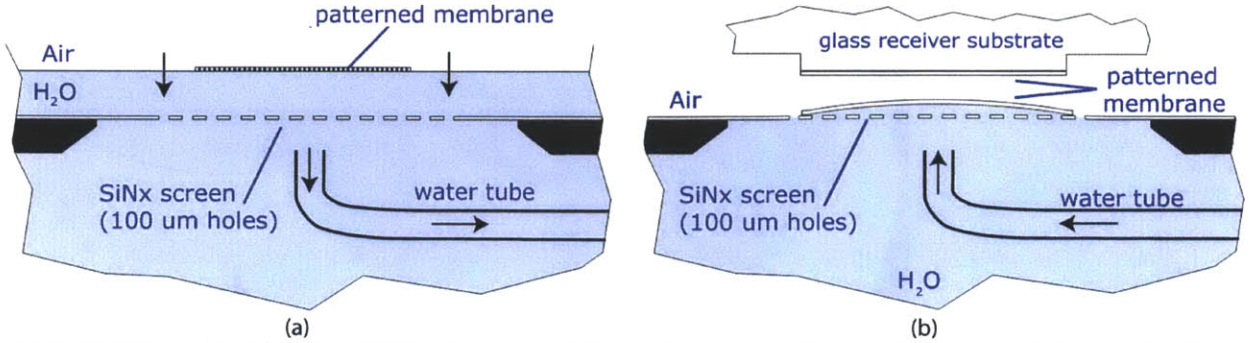


Figure 4.13 The idea of using a SiNx screen to hold and stack a membrane. The screen, fabricated with an array of water holes serves to temporarily hold the membrane – the holes allow the membrane to be attached to and released from the screen. (a) depicts the membrane being attached to the screen; as water is pulled out of the tube, the membrane settles onto the screen and (b) depicts the membrane being bowed upwards toward a nearby glass receiver substrate prior to being released from the screen and stacked onto the receiver substrate.

A new adapter was made to integrate the screen with the 19-mm-thick Teflon base shown earlier in Figure 4.6a. In Figure 4.14a the screen, adapter and base are shown. The screen and adapter were sealed with Unibond wax and the adapter and base were sealed as before with an o-ring. A hydrophilic Teflon filter was incorporated into center of the adapter to restrain the fluid flow through the membrane holes; the air tube was not used. Figure 4.14(b) shows the assembled apparatus; the inset shows the grid of holes in the screen.

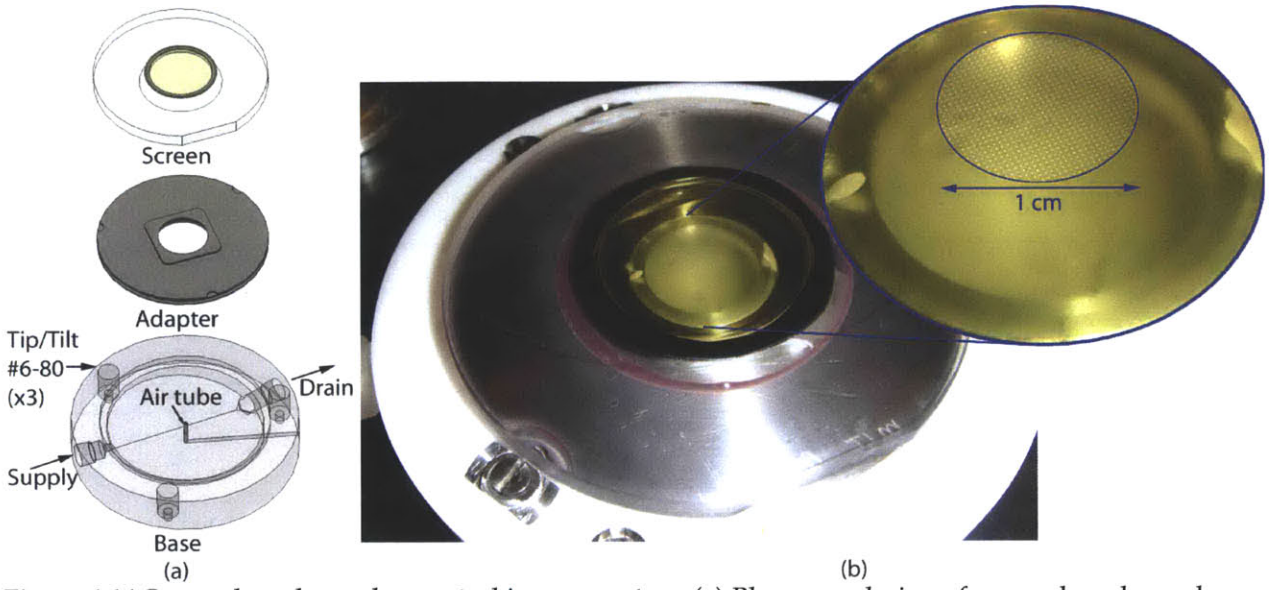


Figure 4.14 Screen-based membrane stacking apparatus. (a) Blown up design of screen-based membrane stacking apparatus showing the base, adapter and SiNx screen. (b) Shows the assembled apparatus. In the inset, the screen in SiNx is composed of an array of 100 μm holes on a 300 μm pitch covering a 1-cm diameter circle.

Figure 4.15 shows the apparatus being filled with water. The chamber beneath the adapter is filled first and then, once there was enough pressure across the filter, water permeated it to fill the space between the filter and screen. The meniscus in the figure shows water, in the center, pushing the air through the holes in the screen. Care was taken to ensure that there were always some holes available for air to pass though. Once only a small volume of air remained beneath the nitride, the apparatus was gently tipped so that the remaining air bubble moved off to one side. This air bubble was instrumental to draining the apparatus after experiments – without it the nitride would shatter when the water was drained out.

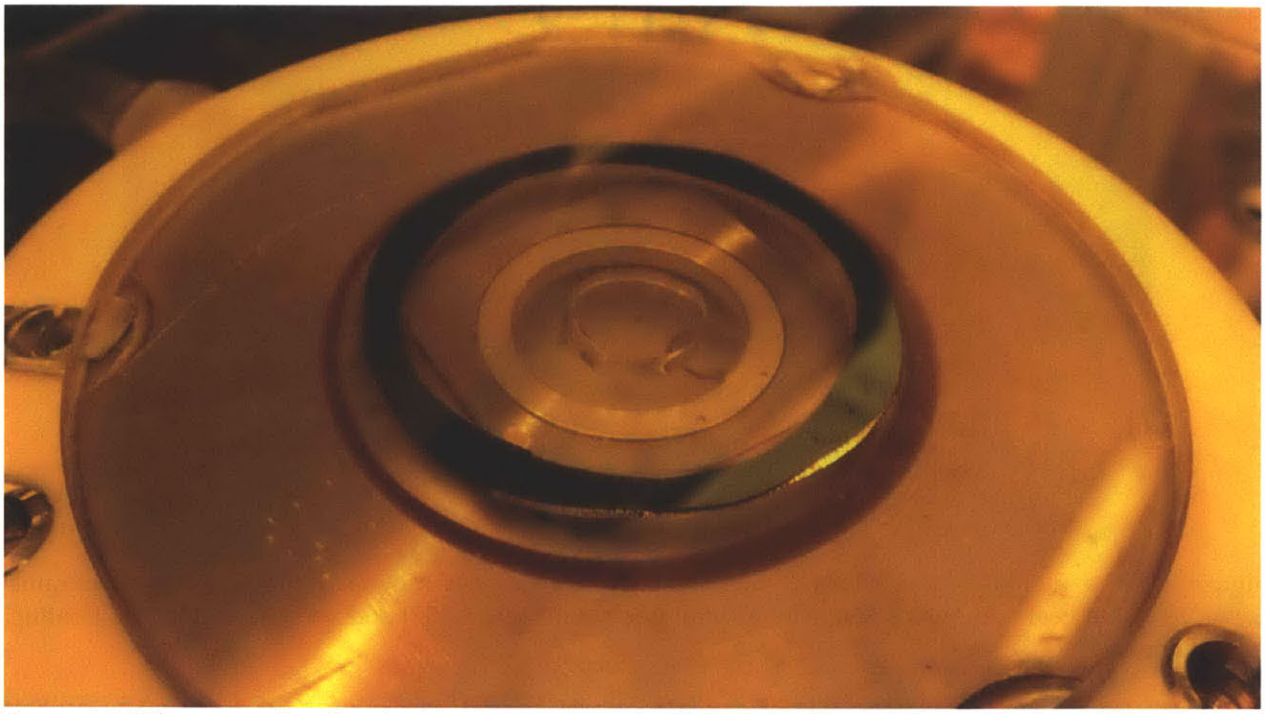

Figure 4.15 The screen is primed with water prior to loading a membrane. The meniscus of the water is visible in this image. As more water fills the space a small air bubble remains (visible in the Figure 4.16) to relieve pressure on the screen when water is drained. To remove the water, the bubble is positioned under the holes in the screen where it grows as the water drains out. If there is no air bubble, then the screen will pop as air is drawn through the holes.

The nitride screen was delicate and introducing perforations further weakened them. Some methods discussed in Chapter 3, e.g. dipsticks and wicks, were deemed too risky to be of use while the membrane floated over the nitride and so the primary means of manipulating them became limited to the air flow technique. To load the membrane onto the screen, water dripped into a puddle onto the glass ring enabled the membrane to float from a cover slip onto the nitride at which point the air gun pushed it into place and dried it down. Figure 4.16 shows the membrane moving from the glass ring onto the screen. Then water was wicked away from the glass ring while the membrane remained floating over the screen on a puddle of water.

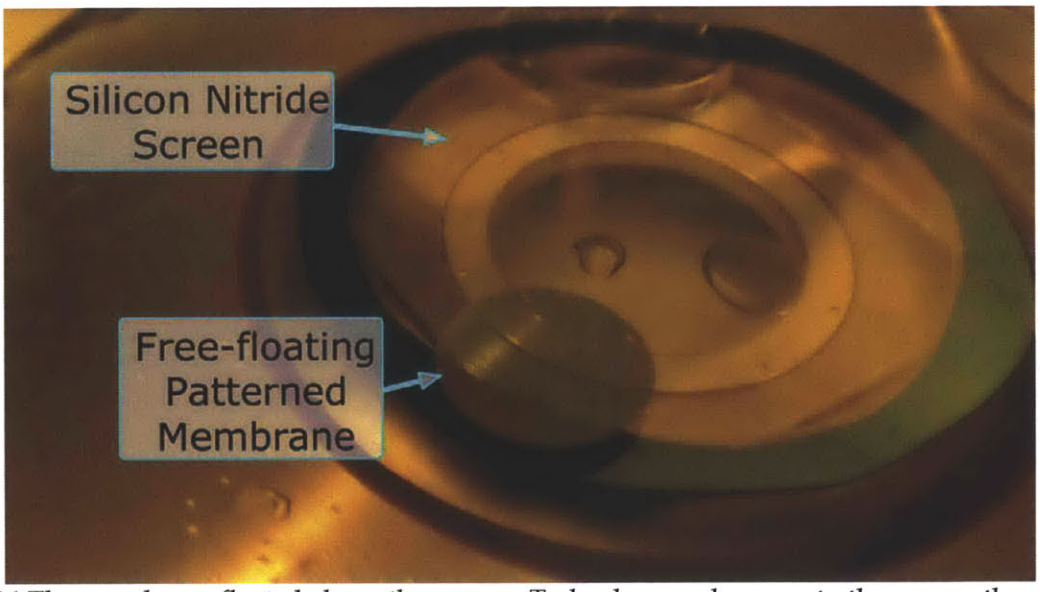


Figure 4.16 The membrane floated above the screen. To load a membrane onto the screen, the apparatus is placed into a beaker of water where an air gun (visible in Figure 4.17) and wick move the free floating membrane over the screen.

In Figure 4.17 the membrane was tilt-dried onto the screen. In Figure 4.17a, the membrane was partially in contact with the screen and a contact front progressed downwards. Figure 4.17b shows the membrane in contact with the screen; the water holes are visible beneath the membrane and "tents" arise where particles forced the membrane and screen out of contact.

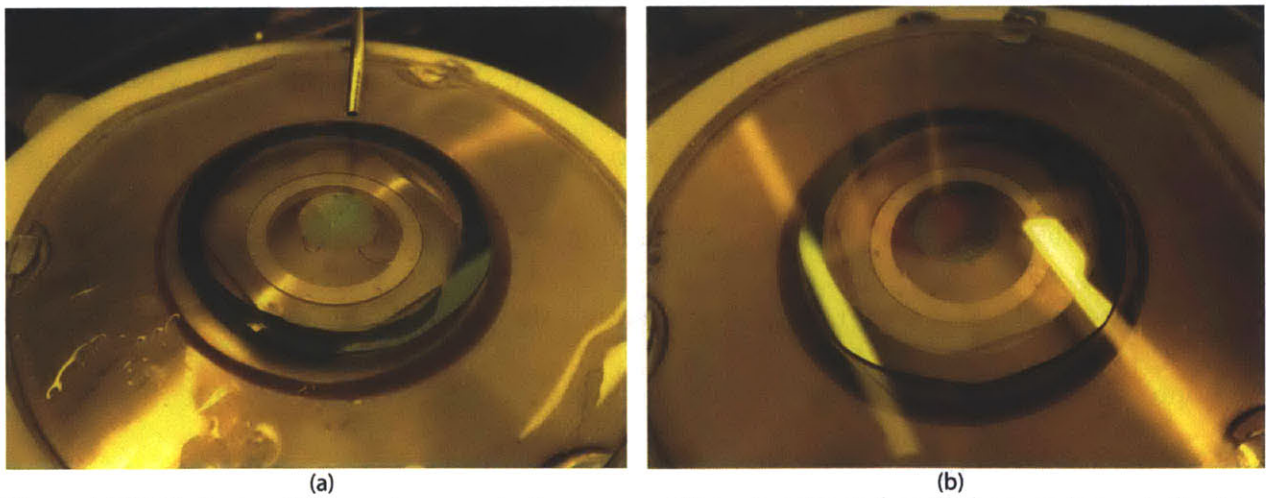

(a) (b)

Figure 4.17 Tilt-drying the membrane onto the screen. Water is retracted until the membrane is floating on a thin puddle and the air gun is used to gently dry them membrane onto the screen. (a) shows the contact front, generated from the air gun, as the membrane dries onto to the screen and (b) shows the dried membrane. Some particles contaminants are visible, as are the holes in the screen.

After the membrane was dried onto the screen, it was loaded as before beneath the receiving substrate. In Figure 4.18 water released the membrane from the screen stacking it onto the receiving substrate.

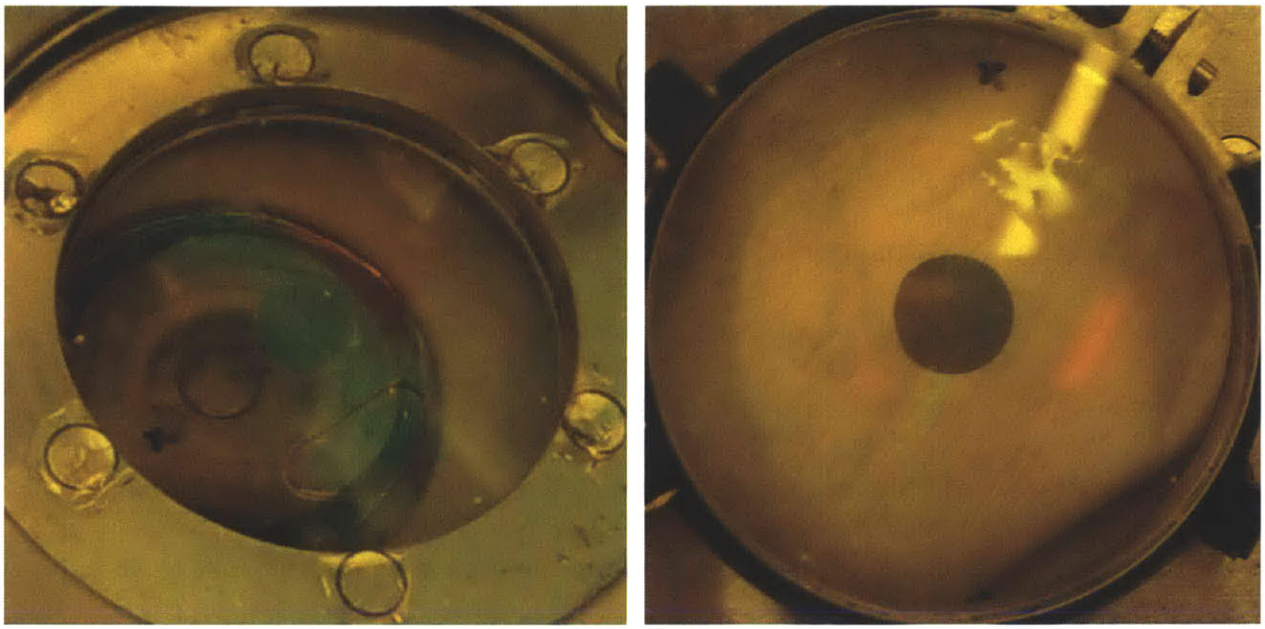

(a) (b)

Figure 4.18 The stacked membrane. (a) The apparatus has translated away leaving the membrane on the receiving substrate. The membrane is diffracting green light; the similar diffraction from the screen will be discussed in chapter 5. Also, a meniscus of water, between the screen and receiving substrate, formed during stacking. (b) The membrane on the receiving substrate. While there were some small holes in the membrane, no cracks or buckles formed from stacking it on the receiving substrate.

The membrane that was stacked onto the receiving substrate exhibited no buckles or wrinkles but why did it release from the nitride? The adhesion force reported in [43] is still much greater than the burst pressure of the nitride and so one possibility is that the small particles of contamination acted to defeat the adhesion between the membrane and the nitride. Then because the nitride had many holes, some of them were able to inject water under the membrane *tents* and in these regions the water pressure never had to overcome the adhesion of intimate contact. This could allow capillary forces to spread the water and release the membrane. While it should be

possible to further engineer the surface of the nitride carrier to facilitate the water-based membrane release step, either by the deposition of a monolayer or by decreasing the contact area to reduce the adhesion, there were other issues that made nitride undesirable as a carrier material.

Nitride carriers were delicate in the wrong ways. As the water evaporated from the screen, back pressure would bow the screen away from the receiving substrate, which caused the nitride membrane to fracture more than once. Moreover, while the nitride can handle moderate point loads, deflecting normal to the surface by easily 100x their thickness, they are weak to shear stresses. When water formed a meniscus between the nitride and the receiving substrate (c.f. Figure 4.18a), because the nitride wets, the component of the surface tension along the nitride would increase the tensile stress in the region covered by water. This could also be a failure mode of the already tensile nitride membrane, especially when the meniscus approached the edge of the nitride. These issues, though not insurmountable, challenged nitride as the carrier material and so a better solution was sought.

In addition to the issues related to releasing the membrane from a carrier substrate, once stacked onto the receiving substrate it also needed to be detached from the water. In the beginning of this chapter, an air bubble was used to drive off the water and then the free surface of water was largely eliminated to allow the membrane to first contact the receiving substrate. Then, with the solid carriers, the membrane was first mostly released from the carrier in order to contact it to the receiving substrate and if water leaked around the membrane during this step it would form between the

membrane and receiving substrate, which could prevent the membrane from stacking. This is exacerbated as silicon oxidizes in water to become more hydrophilic because water leak more easily through the holes at lower applied pressures. Moreover, in photonic crystal designs in which the holes are especially large (e.g. radii ~45% the pitch) this gets only worse. Combined, these observations suggest that despite surface tension's ability to eliminate distortion in the membrane, water ultimately complicates the stacking problem.

Yet another problem with stacking from water was alluded to in the introduction. Recall that membranes could have disjoined patterns (Figure 1.3 is repeated here as Figure 4.19).

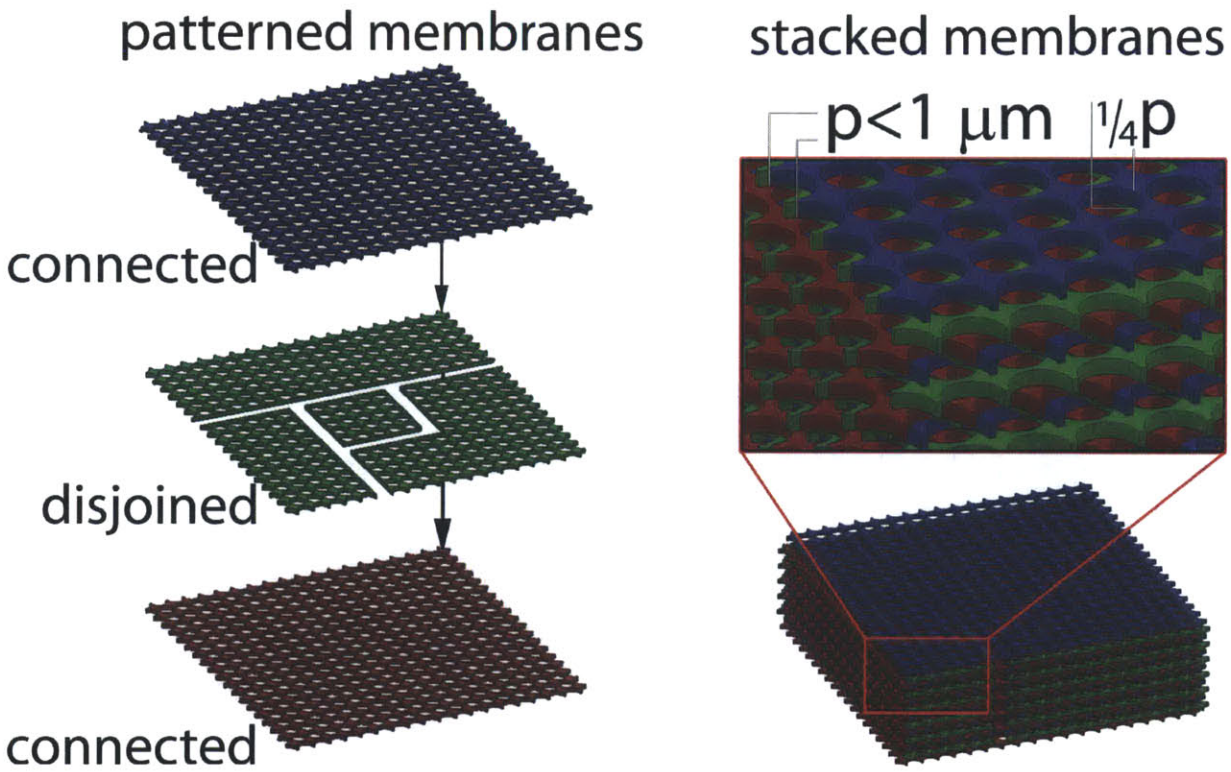


Figure 4.19 Repeat: Stacking in the case of disjoined membranes. Clearly, the supporting the disjoined membrane around its periphery – by a frame or other mechanism – is problematic because its middle region would not remain registered to the others and the edges that result from the cutouts would sag. However if they were held from underneath these issues would be circumvented.

The disjoined membrane, even in the unlikely event it dried onto the carrier in an aligned state, would not adhere to the receiving substrate because water would contact it first. A better stacking process will require careful consideration of the membrane-carrier adhesion and should take into account stacking disjoined membranes.

***Hypothesis 5**: The stiction force that holds membranes on the carrier could be eliminated if instead they are supported during stacking by sublimable adhesive.*

Experiment 5. Membrane stacking from a sublimable adhesive layer

To explore hypothesis 5 required an adhesive. In the approaches of [19] - [24] are many schemes to overcome the adhesion between a membrane and receiving substrate. In general, these methods reduce rather than eliminate the adhesion between the carrier substrate and membrane. Instead, if the adhesive could be sublimated away then during stacking no adhesion forces would remain to affix the membrane to the carrier substrate. The final stacking system explores this idea with polyaromatic hydrocarbons. The main results were demonstration of a low-stress and clean release process which was followed by the vaporization (i.e. sublimation *and* evaporation) of the glue to release and stack of four connected membranes; the conclusion was that additional research would ultimately be necessary to determine the best sublimable agent to enable the disjoined membranes in Figure 4.19 to be staked with the process proposed at the end of Chapter 1.

Within the class of polyaromatic hydrocarbons are four similar materials derived from sequentially linked benzene rings. Naphthalene is composed of two benzene rings

joined together, anthracene follows, then tetracene and finally pentacene. These materials can be thermally evaporated and have sublimation points that are below their melting points as shown in Figure 4.20. Furthermore, it may be possible that light rather than heat or pressure could be used to remove them[5].

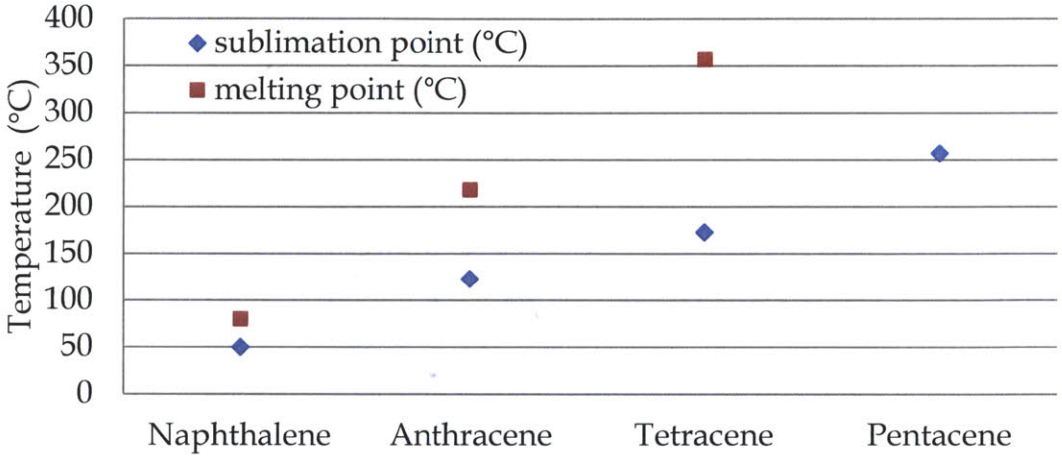


Figure 4.20 Comparison of a few polyaromatic hydrocarbons in increasing number of benzene rings. For these materials, the sublimation point is below the melting point. Of them, Pentacene can withstand the highest temperatures and would likely be optimal for semiconductor processing.

While a high-temperature sublimation point is more desirable from the processing standpoint it is certainly not required with free-floating membranes. In the simple case of fully connected membranes that have been considered up until now, there are no high temperature steps after the membranes are released and so naphthalene is chosen because it is less harmful than anthracene and less explosive than tetracene. Furthermore, naphthalene is sufficient to demonstrate the sublimable release process and so pentacene is deferred for future work.

[5] Photocatalytic degradation pathways exist from anthracene & naphthalene to water and carbon dioxide [44] and a similar photodecomposition reaction [45] of pentacene under the same catalyst has been shown. Interestingly, these pollutants result from burning fuels thus there is a lot of research that describes how to get rid of them.

Before attempting to stack membranes, it was necessary to establish that naphthalene could be used as a low-stress release agent so an experiment was performed. Initially, as imaged in Figure 4.21 a thin silicon wafer was mounted onto a perforated carrier substrate by solidifying liquid-phase naphthalene.

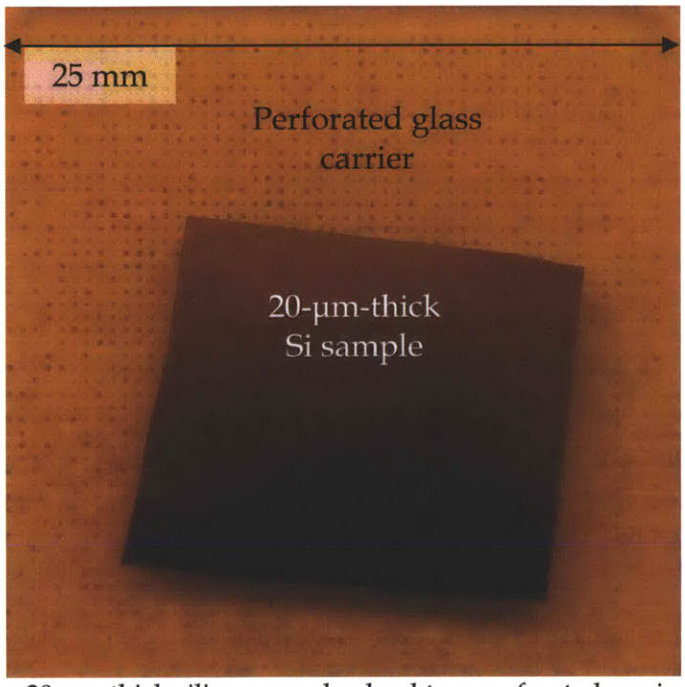


Figure 4.21 Top-view of a 20-um-thick silicon sample glued to a perforated carrier with naphthalene. The thin silicon sample is glued above an array of ~2600 small holes that were laser-ablated into a 200-um-thick flexible glass substrate. The flex glass was mounted onto a glass ring (not shown) to facilitate handling.

Once the silicon sample was glued to the perforated carrier a low-stress vapor release process was demonstrated. First, the Si-loaded carrier was flipped over and placed silicon down (illustrated in Figure 4.22) onto a hot 76.2 mm silicon wafer. At 60 °C the silicon wafer was slightly above the sublimation point of the naphthalene, which caused it to vaporize. Then, after 20 minutes at 60 °C the silicon sample detached completely from the carrier.

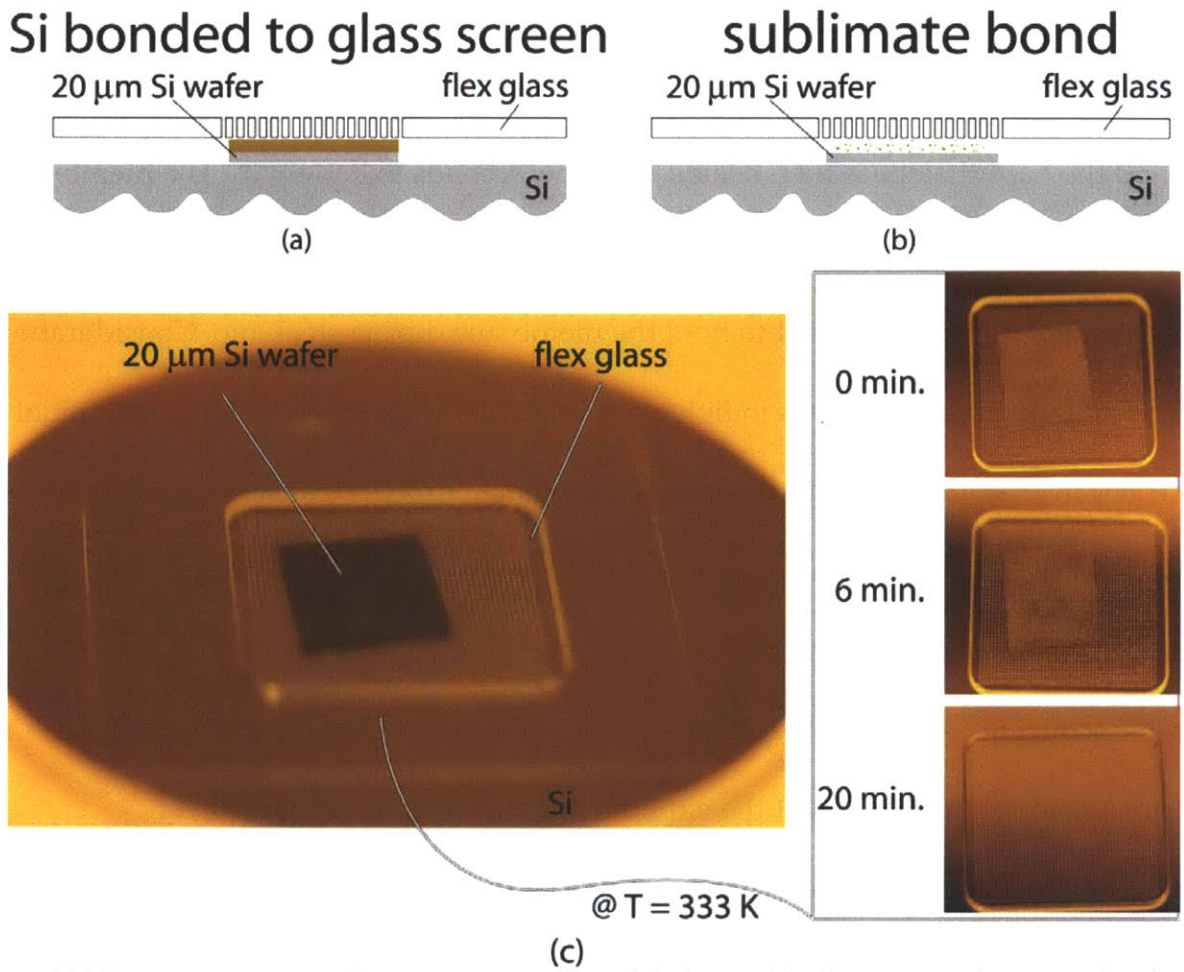


Figure 4.22 Low-stress vapor release process with naphthalene. (a) Illustrates a thin Si wafer that is supported on a perforated sheet of flex glass with a layer of naphthalene. (b) At 60 °C the naphthalene sublimates away to transfer the thin silicon wafer to the underlying 76.2 mm thick silicon receiving substrate. (c) Images showing the release process. On the left the thin silicon wafer is in the configuration described in (a). In the inset of (c): (upper) At the start the naphthalene has not sublimated, (middle) After six minutes the layer of naphthalene has begun to sublimate and the areas surrounding each perforated hole begin to release and (lower) after 20 minutes the thin silicon has detached completely.

In order to incorporate naphthalene into a stacking scheme, there are some questions that needed to be addressed. First, how is a membrane prepared for stacking from a layer of naphthalene? Second, how viable is naphthalene as a glue layer? Third, when the naphthalene is sublimated does it leave behind a residue? Finally, under what conditions is the membrane release process carried out and does it release reliably during stacking?

The first and second questions could be related depending on the fabrication process. In the simplest case, free-floating membranes are dried onto a naphthalene film and the naphthalene is then heated for a few seconds to liquefy it. The membranes float and the naphthalene cools to a solid with the membrane on top. In this case, naphthalene as glue is sufficient to hold the membrane during stacking. Consideration of disjoined membrane patterns in light of the discussion about grinding-down initial substrates in chapter 2 helped to inform the candidate process that was discussed in the introduction. It is worth pointing out that a silicon wafer that was bonded with a layer of naphthalene to a glass cover slip survived several minutes of scrubbing with an abrasive scouring pad. No edge chips formed in the glass cover slip nor did the two delaminate and so to that extent the naphthalene is sufficient as a glue layer.

The third question is really important because if a scum layer remains after the naphthalene is gone a post-cleaning step will be required. To test this in a realistic way, a prime silicon wafer was inspected with the steam nucleation test, cleaned and hydrogen-terminated with HF and then observed again with the steam test. After a uniform initial droplet pattern appeared from the steam test, naphthalene was thermally evaporated onto the silicon to form several disconnected crystals. Then two clean glass cover slips were glued via the layer of naphthalene to the silicon by briefly heating the silicon up to 100 °C. After the two were glued down, the excess naphthalene that was not between the silicon and glass boiled off and the silicon wafer with glass cover slips was inspected under the steam test. The nucleation points where the naphthalene crystallized on the silicon were visible in the steam pattern. After the

steam test, the hotplate was increased to 180 °C and the substrates were baked for 10 minutes. The glass cover slips detached from the silicon and the subsequent steam test showed no evidence of the original nucleation points, though the regions of silicon which housed the cover slips showed a different dot pattern than the rest of the silicon. After another 10 minutes on the hotplate, the droplet pattern returned to the uniform initial state and no residual contamination was apparent.

The last question is most relevant to membrane stacking. Four nanomembranes were fabricated and then stacked following the process described in Figure 4.23. Following the drying process of Figure 3.11, the first membrane was deposited onto a film of naphthalene coating a glass cover slip – the carrier - and was then adhered to the carrier by briefly placing on the hotplate at 90 °C until liquid naphthalene was only present between the membrane and carrier. While it is possible that some residual naphthalene was present, none was visibly left on the carrier except beneath the membrane and carrier. The carrier was then flipped over and the membrane was contacted to another cover slip – the receiver. They were heated at 180 °C for 7 minutes and then removed from the hot plate. Once the membrane was stacked onto the receiver the carrier was lifted away with tweezers and the buckle-free membrane remained on the receiving substrate see Figure 4.24. The receiving substrate was placed back on the hotplate while the carrier was prepared with the next membrane.

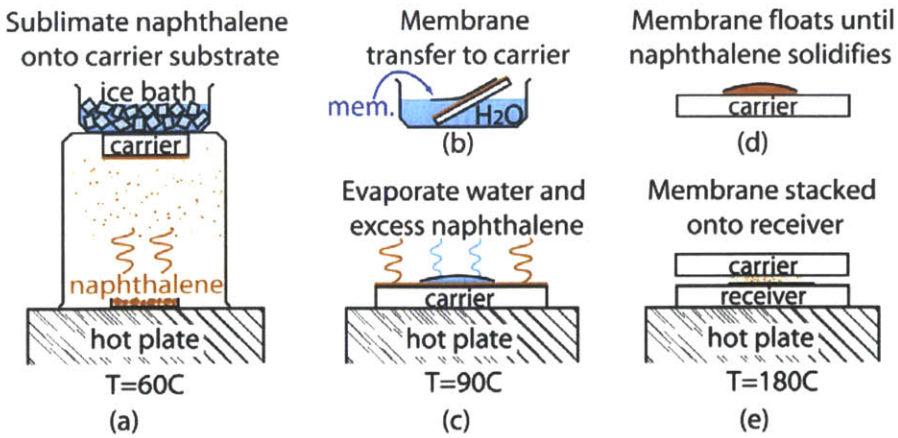


Figure 4.23 Adhesive-based stacking process. In (a) naphthalene was evaporated onto a carrier substrate. In (b) a free floating membrane was picked up on the naphthalene-coated carrier. The membrane remained free-floating throughout (c) where at 90 °C residual water and excess naphthalene evaporated leaving the membrane on only liquid-phase naphthalene. Removal of the carrier in (d) caused the naphthalene to solidify. In (e) the carrier is flipped face down and placed onto the receiver at 180 °C until the naphthalene boiled away after which the carrier was removed leaving behind the membrane.

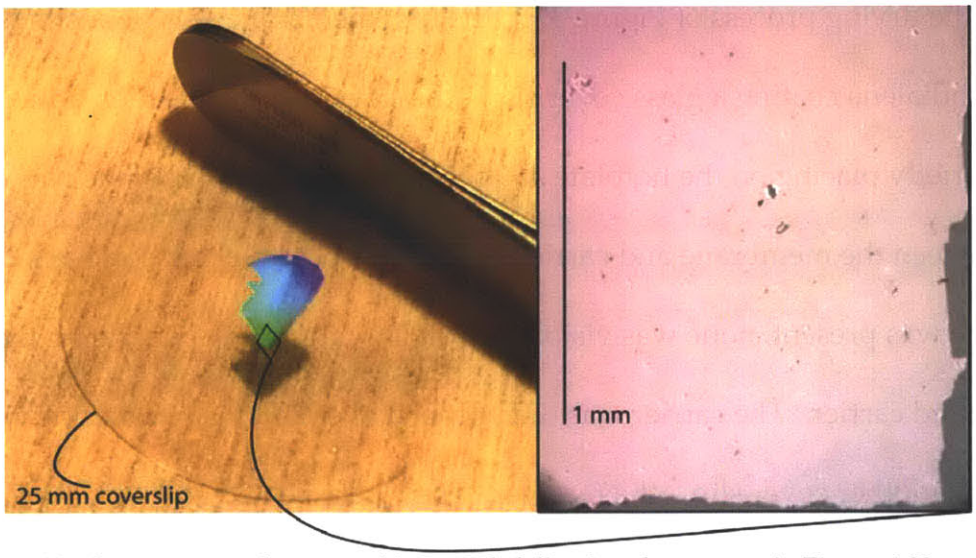


Figure 4.24 Buckle-free nanomembrane stacking result following the process in Figure 4.23.

This process was repeated to stack the other three nanomembranes that are shown in Figure 4.25. In (a) the moiré patterns that resulted from their overly are obvious. In (b) is a SEM showing the same four layers at a higher magnification.

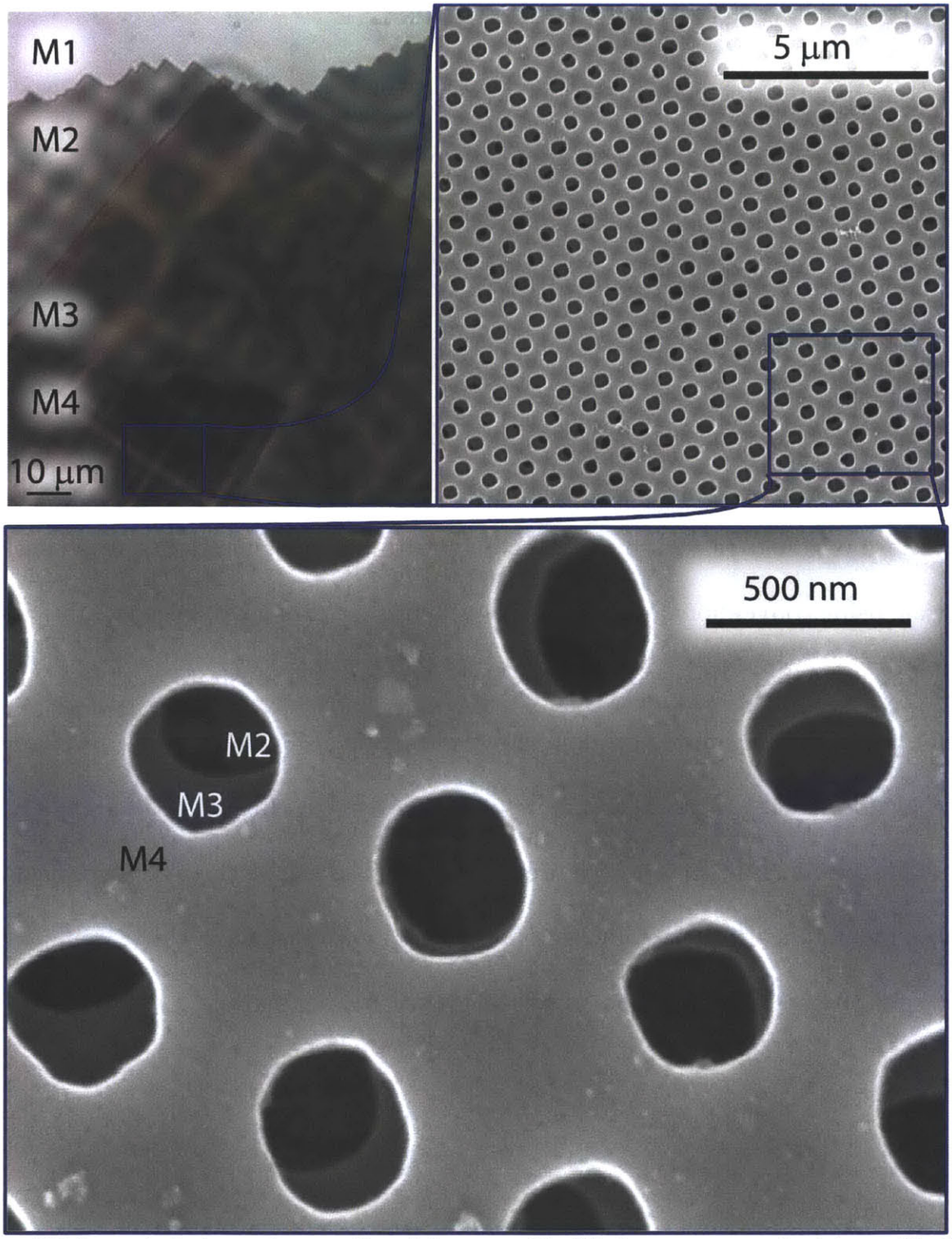


Figure 4.25 Four stacked membranes aligned by eye. Naphthalene was vaporized to enable four membranes to be stacked up. In (a) is a 100X micrograph that shows the moiré fringes generated by the sequentially stacked layers. (b) shows a SEM of these membranes.

# Chapter 5. Alignment techniques

Five different methods to stack membranes were reviewed in the last chapter. In this chapter two different relative alignment approaches are described, which rely on interferometric alignment techniques to infer the position and orientation of the membrane relative to the receiving substrate. It was not possible to combine the naphthalene-based stacking process with the alignment system without significantly modifying the setup and so the techniques described herein relied on the earlier apparatuses and were thus of limited success.

It is possible to register the first membrane to alignment marks on a receiving substrate using conventional interferometric alignment techniques. If the membrane's fine grid pattern, of pitch $p$ (recall Figure 2.11b), serves as the substrate mark in the ISPI scheme then light transmitted through the corresponding $P_1P_3$ marks on the receiving substrate (located above the membrane) would interfere with this grid pattern to form fringes. However, as is shown in Figure 5.1, once aligned and stacked the alignment of the next membrane using the same alignment marks would fail because the first membrane obscures the alignment marks on the second membrane.

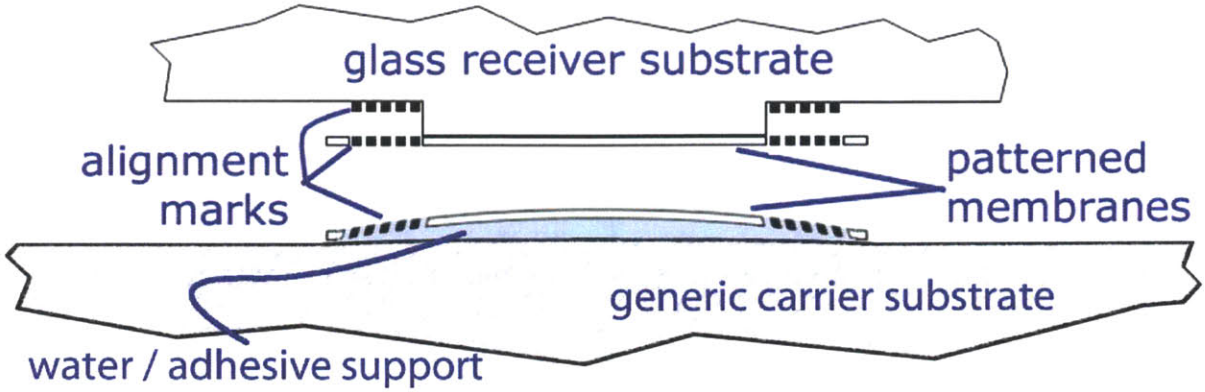


Figure 5.1 The alignment problem. Neglecting the details of the stacking approach, assuming that a first membrane is aligned and stacked onto the receiving substrate then every subsequent membrane's alignment marks would be increasingly obscured by those on it its predecessors.

Alignment of a freely-floating and then dried-down membrane to the receiving substrate is complicated by the fact that the membrane's position on the carrier is arbitrary. Interferometrically imaging the membrane's fine grid should be possible within the ISPI scheme but the membrane still needs to be stacked and subsequent membranes also need to be aligned. In the *align-step-and-stack* approach the membrane is referenced directly to the receiving substrate but is not immediately stacked, instead the membrane is precisely moved to and stacked at a different spot called the stacking site. In the *secondary referencing* approach the membrane is referenced to the carrier and the carrier to the receiving substrate, then the membrane can be stacked onto a blank region of the receiving substrate without obscuring the alignment markers.

a. **Align-step-and-stack**

Perhaps the simplest technique to circumvent the alignment problem is to align the membrane to the receiving substrate and then precisely move the stage to a different location. Then the membrane could be stacked on the receiving substrate without

obscuring the alignment marks. In this approach, which was explored using the rigid glass stacking apparatus (c.f. Figure 4.11), there are two stages of alignment as depicted in Figure 5.2. First, the *home* position of the membrane is established using the interferometric marks on the receiving substrate and second the translation to the *stacking site* is mediated by a separate encoder that measured stage motion.

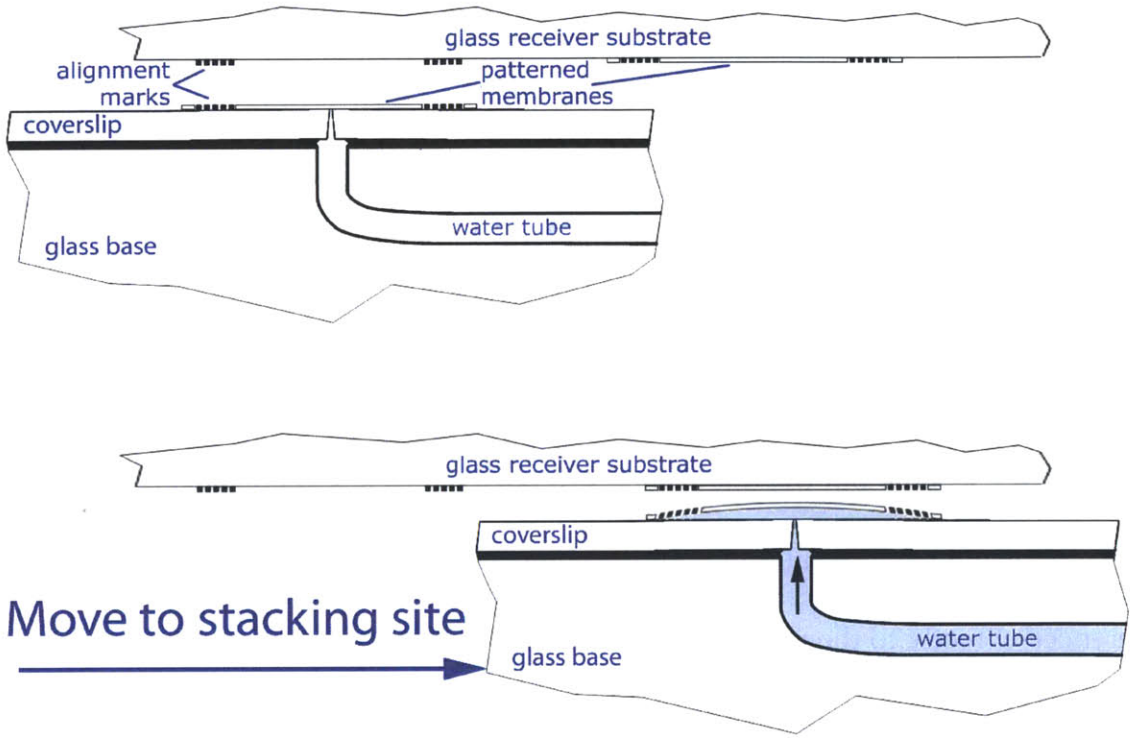


Figure 5.2 Align-step-and-stack approach. The membrane is dried onto the glass cover slip as before in Figure 4.11. Initially, the membrane is aligned to the alignment marks on the receiver substrate (top) and once aligned the membrane is translated to the stacking site (bottom) where water releases the membrane to stack it onto the glass receiver substrate.

Within the ISPI scheme, interferograms that were generated between the $P_1P_3$ alignment marks on the receiving substrate and the fine grid pattern on the membrane would change when the membrane moved relative to the receiving substrate. Figure 5.3 shows typical interferograms generated when the membrane was at the *home* position. Within the x-directed and y-directed fringes sets are three salient features, which are described in the insets of each image. In the left inset of each, the averaged

signal from the fixed array of horizontal *bars* is used to compare the phase of the averaged signals from the sets of *fringes* shown in the right insets. In this case, the fringe signals in both the left and right insets were lined up at the 400th pixel, which is demarcated by a horizontal line through each of the interferograms.

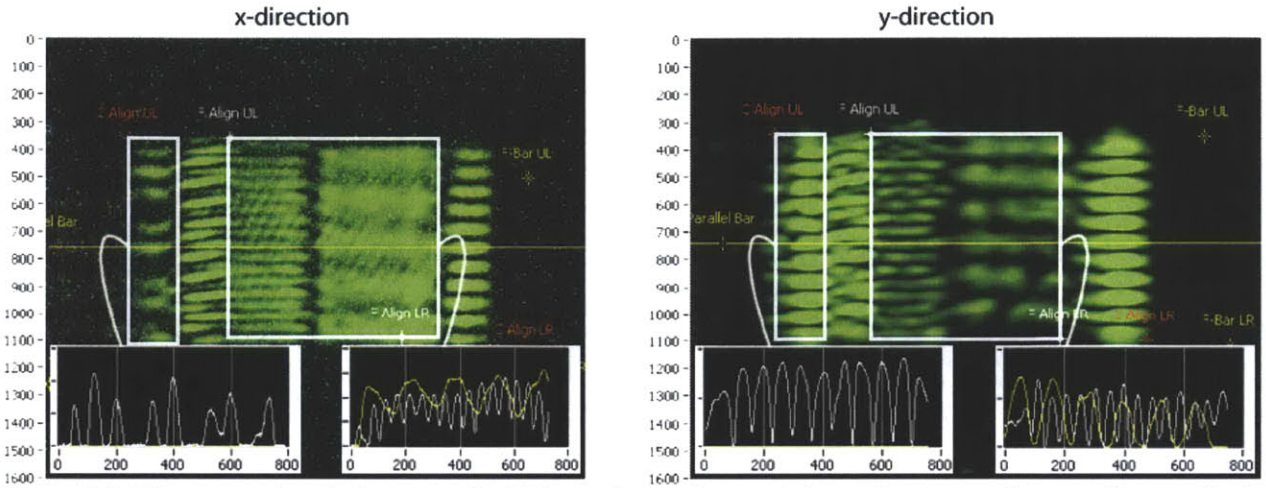


Figure 5.3 Alignment signals between the $P_1P_3$ marks on the receiving substrate and a membrane. Each of the x-directed and y-directed interferograms maps the relative position of the grid pattern ($P_2$ mark) on the membrane to the $P_1P_3$ mark on the receiving substrate by comparing the phase of the *bars* on the left to that of the *fringe sets* on the right. In this case, the averaged signals from the *bars* and *fringe sets* in both the left and right insets were lined up at the 400th pixel to define the *home* position, which is demarcated by a horizontal line in the interferograms.

Were the membrane to translate in either direction the *left* and *right fringe sets*, identified in the large rectangles in Figure 5.3, they would move counter to each other while the *bars*, in the narrow rectangle, remained stationary. After a displacement of $\frac{1}{2}P_2$ both sets of fringes would cycle back so that the peaks again lined up with the horizontal line. In consideration of the meshpile structure where the first membrane is shifted by *p/2* from the second membrane the required displacement would be a shift in both the x- and y-directions by $\frac{1}{4}P_2$.

Another feature of the $P_1P_2P_3$ scheme is that it can be used to infer the pitch of the membrane pattern that is seen by the ISPI scope. Assuming $P_1$ and $P_3$ are known *a*

*priori* this pitch can be calculated from the fringe spacing. In Figure 5.3 the fringe sets each have different fringe periods. By measuring the distance between the peaks of the averaged fringe profiles the number of fringes within each fringe set can be calculated. Within the x-directed microscope image 4.74 and 17.43 fringes were calculated over the 220 μm field and in the y-directed image there were 15.4 and 6.22 fringes over the same size field. From [26], the relationships that describe the fringe period $p_f$, the average period $p_{av}$ and the pitch $P_2=\sqrt{2}p$ on the membrane as seen by either the $P_1$ or $P_3$ grating on the receiving substrate are given in (19). Thus, by counting the number of fringes in the left and right fringe sets, the measured values of the membrane pitch while being viewed with the ISPI microscopes are $p_x$ = 717nm ±0.2 nm and $p_y$ = 714.1nm ±0.3 nm.

$$p_f = \frac{P_{1,3}P_2}{2\left|P_{1,3} - P_2\right|} \;\&\; p_{av} = \frac{2P_{1,3}P_2}{P_{1,3} + P_2} \tag{14}$$

In contrast, measurement of 325-nm-light diffracted from a pre-released patterned SOI sample lead instead to a periodicity of $p_x = p_y$=714.59nm ±0.89nm. Despite careful alignment of the Mach Zehnder interferometric lithography system following the method described in Chapter 2, $P_2$ on the membrane deviated from the ideal specification of the $P_2$ alignment feature by approximately 10 nm. While this deviation could complicate closed-loop positioning of the membrane at the *home* position[6], instead

[6]The closed loop control algorithm developed in [26] interprets the phase information between the averaged fringe sets from interferograms similar to Figure 5.3. The magnitude-squared of the cross-power spectrum is used to pick out the dominant frequency of the combined left and right fringe sets and then at that frequency the phase shift is encoded in the angle of the cross-power spectrum. When the fringes are locked in closed-loop feedback this angle is stabilized so that the relative phase shift between the fringes does not change. However, different frequency fringe sets introduce errors into the phase shift measurement, which can destabilize the closed-loop control.

of using feedback, the coarse stage was powered down and the 4-μm travel piezo XYZ stage was used to home the membrane until it was translated to the stacking site.

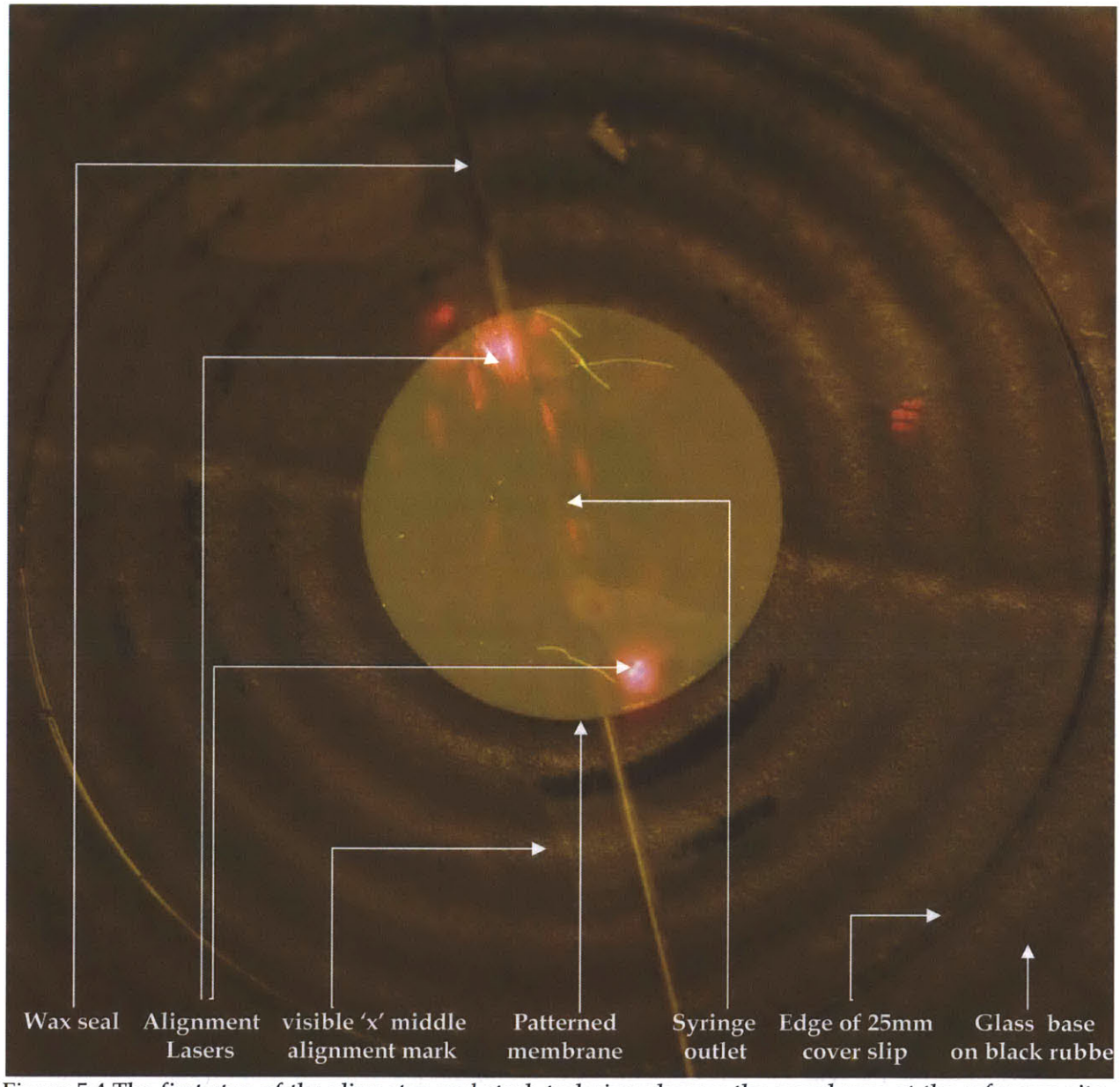


Figure 5.4 The first step of the align-step-and-stack technique homes the membrane at the reference site. The 1-cm-diameter membrane in the center of this image was dried onto the cover slip of the rigid stacking apparatus shown previously in Figure 4.11. The black rubber beneath the apparatus was used to reduce back reflections from underlying vacuum stage. The fringes shown in Figure 5.3 resulted from beams of 660nm laser light, visible here as the two red dots, interfering as they bounce back from the marks on the glass receiving substrate and the alignment mark of the membrane pattern. Also identified is the middle of the visible 'x' alignment marks described in the layout of Figure 2.10. The syringe outlet is located ~100um from the ablated hole (not annotated) in the glass cover slip.

Once the membrane was homed, as in Figure 5.4, the coarse stages were used to translate the stage to the staking site. The encoders on the coarse stage could lose encoder counts if the stage moved too fast and so a repeatability test was performed at different stage velocities to determine how fast the stage could accurately move from *home* position to the *stacking site*. A calibration standard, 1.7 cm in length patterned with a ~714.59 nm-pitch grid in silicon was positioned beneath the 'x' ISPI mark and the coarse stage traversed back-and-forth over a distance of 1 cm at 2mm/s and 0.2 mm/s. Figure 5.5 compares the fringe sets on the x-scope at the start of and after 10 translations (5 round trips) at 0.2mm/s. Following [26], at 2mm/s the fringes were calculated to be out of phase by 11% of a fringe cycle or ~28nm and when the stage was moved at 0.2mm/s the fringes were calculated to be out of phase by 6.5% or ~16.5 nm.

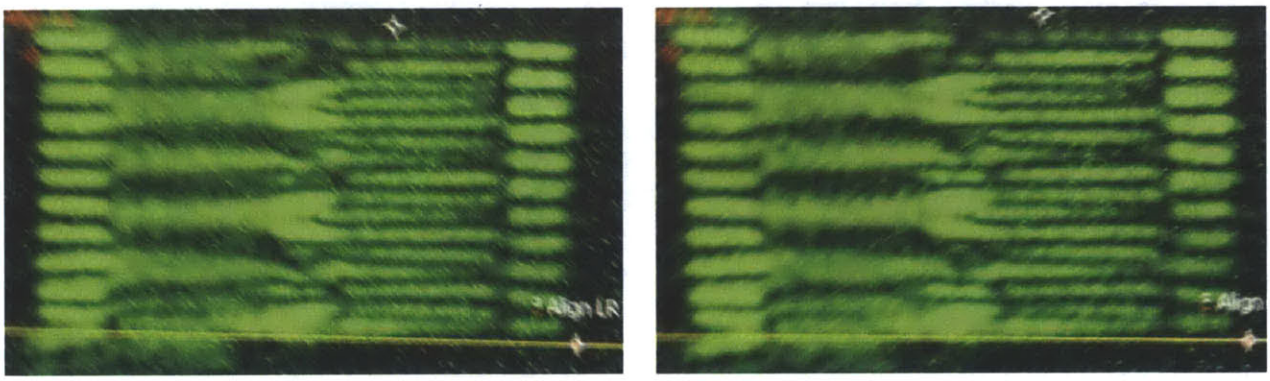

(a) (b)

Figure 5.5 Evidence of repeatability in the native stage encoders. (a) fringes between a calibration standard (i.e. a patterned SOI chip - recall Figure 2.22) and x mark on the receiving substrate before the stage was translated at 200 μm/s. After traversing 5 roundtrips the fringes (b) was observed on the x-scope. By measuring the relative displacements between the left-left and right-right fringe sets between (a) and (b), led to a phase shift of 6.5% corresponding to 16.5 nm of error in the repeatability.

The membrane shown in Figure 5.4 was slowly translated 1.1 cm to the stacking site as shown in Figure 5.6. In the figure, the red laser dots above the membrane indicate the locations of the registration marks on the receiving substrate that were used

when it was aligned to the home position. Visible on the receiving substrate above the top of the displaced membrane is the mirror-image of the middle of the visible x-marks that were described previously in Figure 2.10. It was thought that this mark could be used to study errors in the first membrane's positioning after it was stacked: if the same fringe patterns were imaged with this mark before and after stacking then the membrane would be precisely positioned on the receiving substrate.

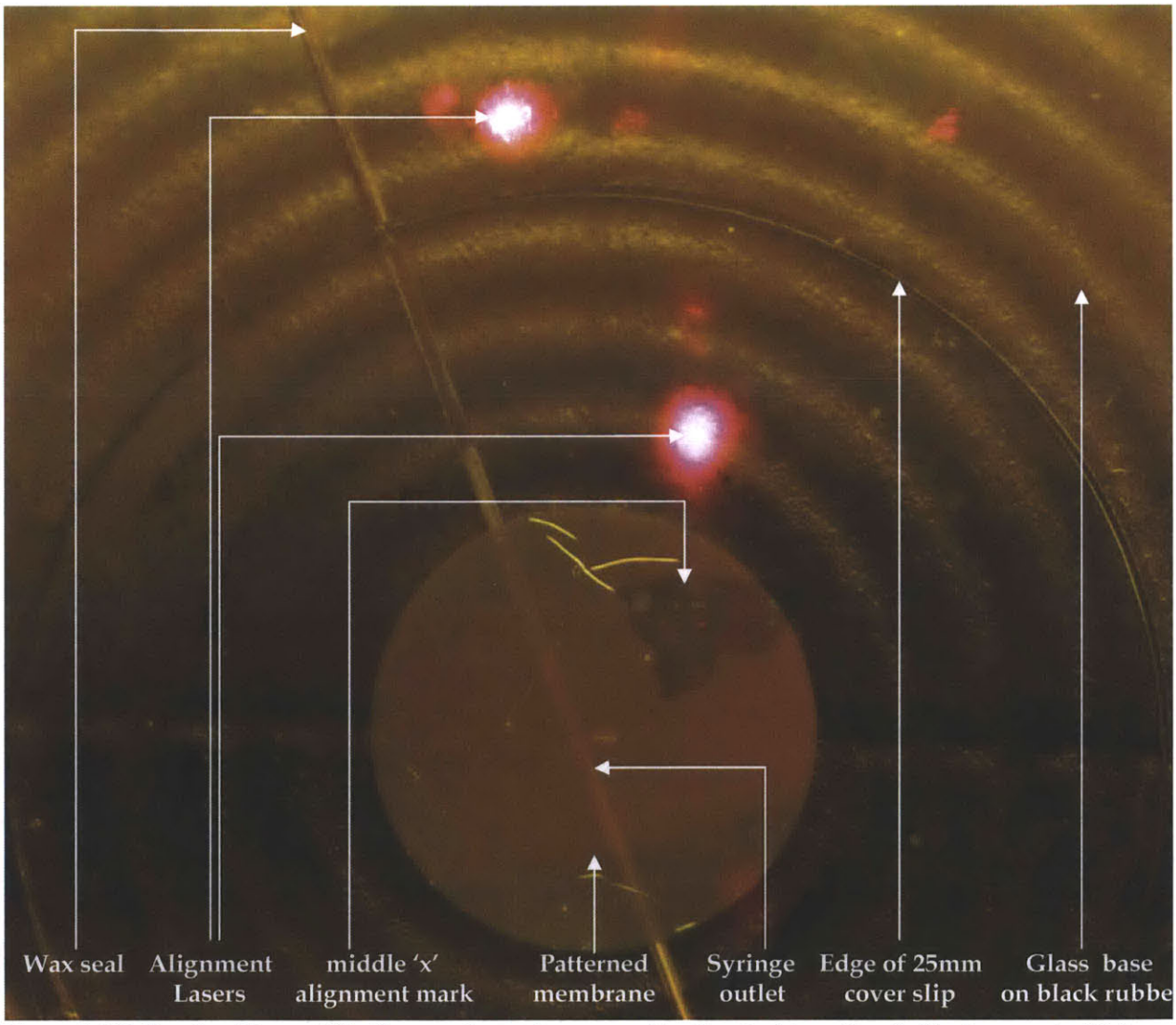


Figure 5.6 Following Figure 5.2b, the membrane has moved to the stacking site. A displacement of 1.1 cm from the home position is indicated by the two laser dots in the upper part of the figure. On the receiving substrate above the upper right of the membrane is an image of the middle visible 'x' mark from Figure 2.10. Beneath the membrane, the syringe needle and diesaw groove are visible as well.

After the membrane was positioned at the stacking site water was pumped beneath the cover slip to release it. A section of the released membrane formed a contact front on the receiving substrate as illustrated in Figure 5.7. However, before pressure released the entire membrane water permeated its holes spilling out to form a meniscus visible around the upper right edge of the cover slip.

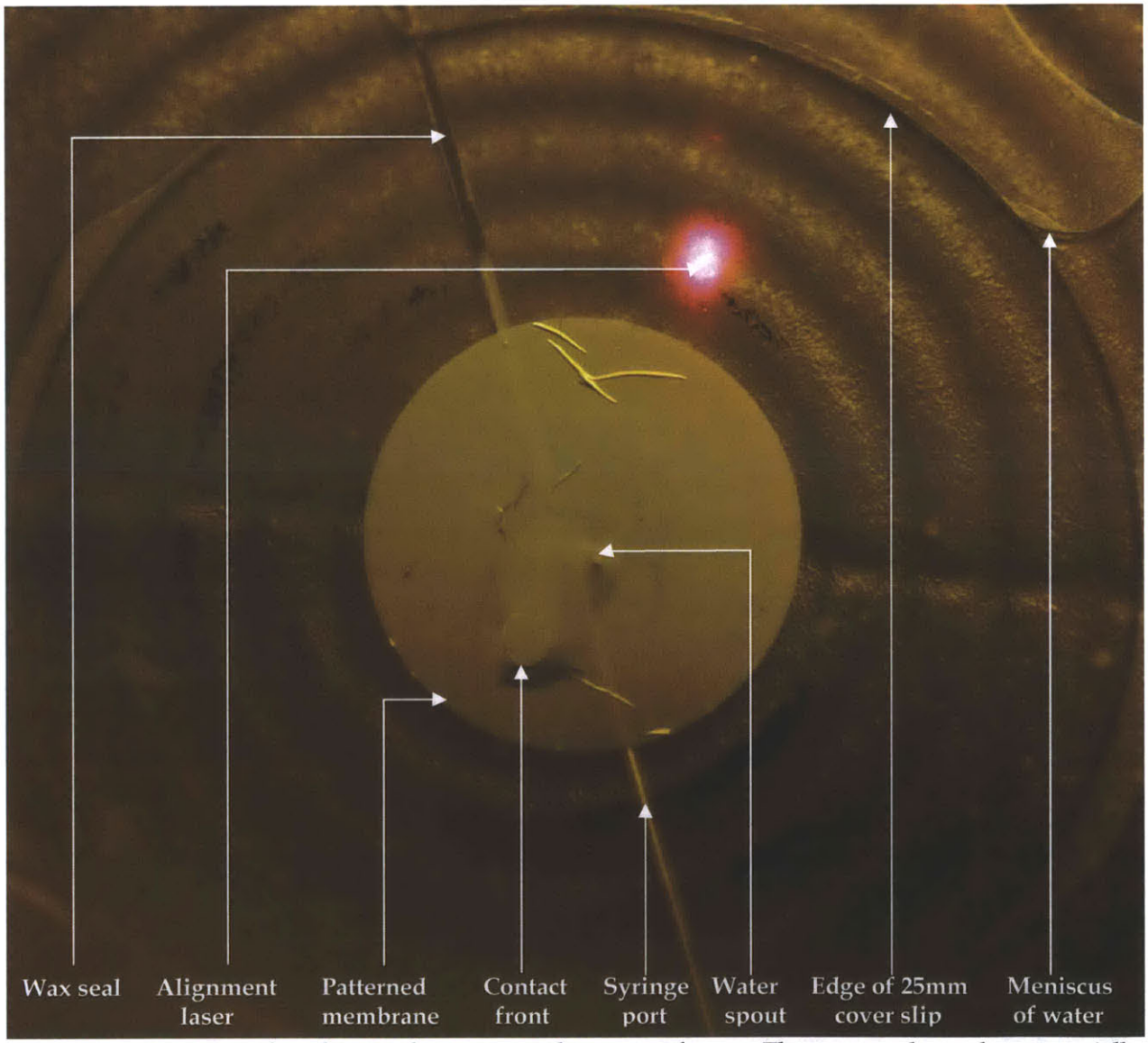


Figure 5.7 As water pushes the membrane upwards, contact forms. The patterned membrane partially released from the cover slip to form initial contact to the glass receiving substrate, but before it released entirely from the glass a water spout formed and water leaked through the holes in the membrane. Once water leaked through the membrane holes it did become more detached from the glass. The membrane was recovered and imaged in an optical microscope to confirm that the waterspout did not damage it.

While unsuccessful from the standpoint of stacking, this alignment approach showed promise. It did not take long to perform the align-step-and-stack step manually and this scheme could be extended to a closed-loop sequence, provided the membrane pitch was more closely matched to the alignment marks requirements. Fortunately, the alignment tolerance of 10% the membrane pitch (~50 nm) was well within the positioning capability of both the homing step with the interferometric scopes (sub-nm) and the step-motion governed by the stage's native encoders (<25-nm bi-directional repeatability).

b. **Secondary referencing approach**

In the secondary referencing scheme described in Figure 5.8a the membrane is first aligned to a nitride screen and then the screen is aligned to the receiving substrate. Once the membrane is aligned and then stacked on the receiving substrate it does not obscure the alignment of the next membrane because the marks on the receiver are not underneath the membrane. Figure 5.8b shows one of the fabricated nitride screens (fabrication details can be found in the Appendix). In addition to the water holes, the screen was patterned with a high-resolution grid (seen diffracting in the image) that, having a pitch of ~709 nm, was designed to generate moiré patterns with both the membrane pattern and the $P_1P_3$ alignment features on the receiver substrate (c.f. Figure 2.11a). The pitch of the screen constrained the membrane pitch as well: if the screen rotated from the membrane by less than ±0.25 degrees, a moiré pattern with fringe period of at least 100 μm is generated when the pitch of the membranes deviates by less than 0.55 % of the pitch of the screen.

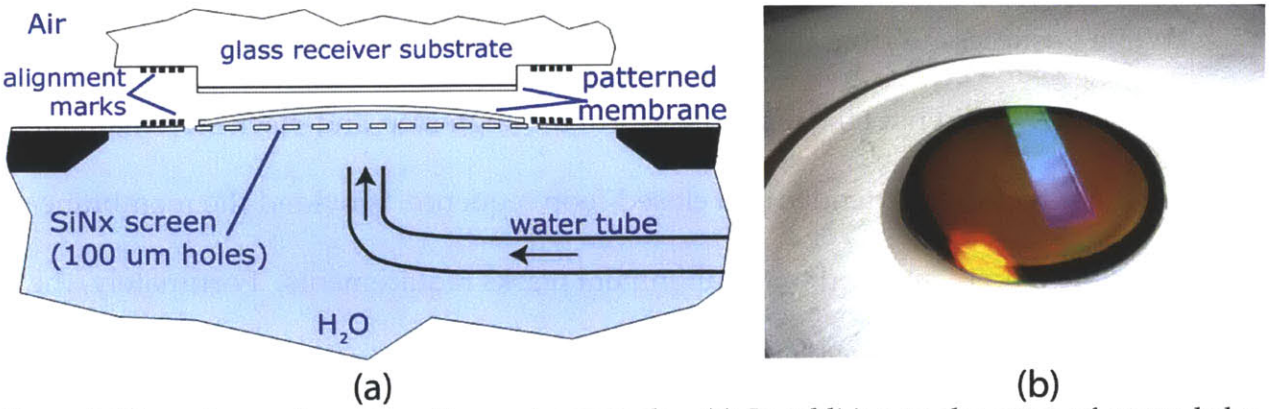


Figure 5.8 Secondary referencing alignment approach. (a) In addition to the array of water holes, alignment marks were added to align the screen to the receiving substrate. While localized alignment marks are depicted here for clarity, in practice, a high resolution grid pattern (~709 nm pitch) was printed onto the screen with interference lithography as shown in (b). Then, during an alignment step, the membrane would be first aligned to the screen and then the screen would be aligned to the receiver substrate.

In order to generate similar periodicity between the membranes, screen and $P_2$ mark, the Mach Zehnder was aligned to the $P_2$ mark following the process described in Chapter 2. Both the $SiN_x$ screen and the SOI wafers were exposed in the same fabrication run; due to their different thickness adjustment of the micrometer, z-stage (see Figure 5.9) brought each substrate into alignment with the same exposure plane[7].

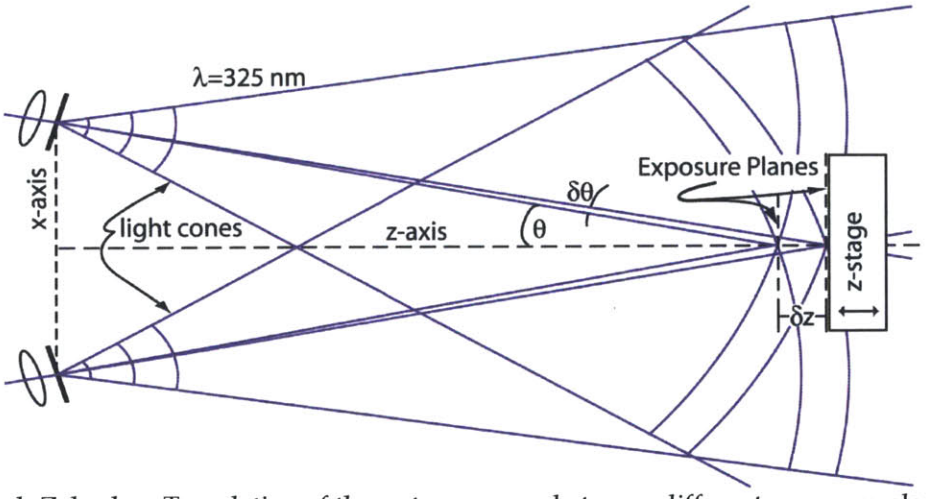


Figure 5.9 Mach Zehnder. Translation of the z-stage moves between different exposure planes.

[7] The position error of the z-stage roughly scales with deviations between the pitch of the screen vs. the pitch of the membrane (for deviations <~1%). Because the distance to the z-stage is ~1m, this means that an error of 0.55% in the pitch corresponds to roughly a displacement along z of ~ 5mm, which was well within the capability of the stage.

Figure 5.10 shows the fabricated screen, adapter and base being filled with water. The fine grid pattern diffracted the camera flash; the 100-μm-diameter holes are visible in the center of the nitride. The region between the nitride and the adapter plate is being filled from the outside inwards with water; a ~2-cm-diameter column of air has yet to be evacuated. Once primed by eliminating most of the air, the membrane was loaded and dried onto the screen (c.f. Figure 4.17).

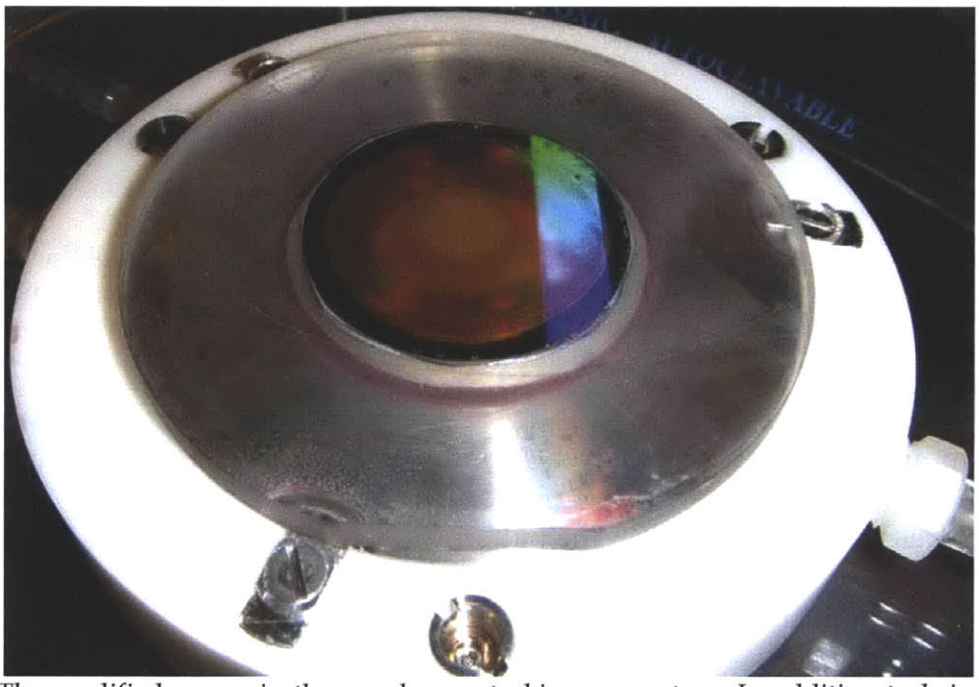

Figure 5.10 The modified screen in the membrane stacking apparatus. In addition to being patterned with an array of water holes, the high resolution grid pattern is shown diffracting a fiber light.

In Figure 5.11 are images of a silicon membrane that was dried onto the nitride screen. In the SEM image, the nitride membrane in the top half exhibits a checkerboard pattern and in the bottom half the silicon membrane covers the nitride. The membrane is rotated by 0.237 Rad from the silicon nitride. The optical micrograph shows a 100-μm-diameter water hole in the nitride spanned by a membrane. In the region outside

the hole moiré fringes are visible that arise from the difference in pitch and rotation between the membranes.

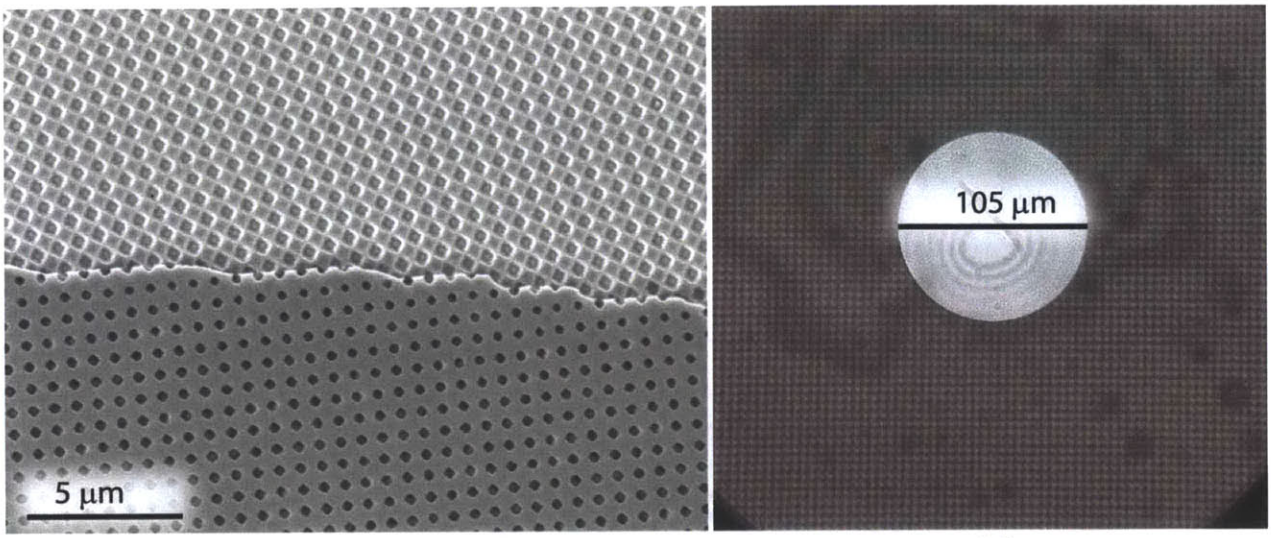


Figure 5.11 Images of a membrane on the screen. (left) Electron micrograph taken at 5kV with a working distance of 4mm that shows the silicon membrane, in the lower half of the image on top of nitride. Above it, the nitride checkerboard pattern is visible. (right) Optical micrograph of the membrane spanning one 100-μm-diameter water hole. The grid moiré pattern corresponds to 0.237 Rad of rotation between the membrane and nitride.

The moiré pattern provides a wealth of information about the position and angle of the silicon relative to the nitride. The patterns in the silicon membrane and those in the nitride are periodic in two directions and can be represented in inverse space by their spatial frequencies and corresponding grating vectors. For each direction of the periodic structure, the grating vectors, directed along the direction of the periodicity, have a magnitude, the spatial frequency in that direction, that is inversely proportional to the pitch as illustrated in Figure 5.12. In inverse space (k-space) these grating vectors form a basis that entirely describes the periodic structure of the membrane.

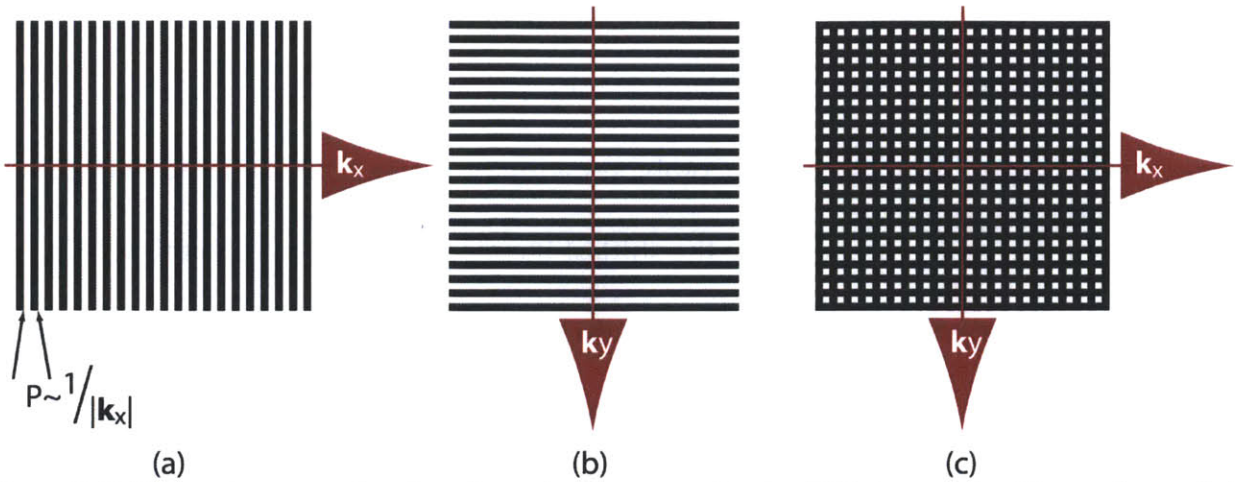


Figure 5.12 Nomenclature used to describe periodic patterns having 50% duty cycle. The grating period, denoted by P, is related to the magnitude of its corresponding grating vector, which is denoted by (a) $\mathbf{k}_x$ or (b) $\mathbf{k}_y$. (c) The overlap of two gratings creates a grid pattern which is represented by a vector field $\mathbf{k}_x \times \mathbf{k}_y$. In an orthogonal grid, the grating vectors are perpendicular.

To analyze the moiré patterns between two grid-patterns in contact it is helpful to decouple the x-directed and y-directed grating vectors. This is shown in Figure 5.13. The x- and y-directed periodic patterns, in (a) and (b) respectively, are superimposed to form the moiré shown in Figure 5.13c. The moiré fringe vectors are described by the difference vector between overlaid periodic patterns. Thus, When the periodic patterns

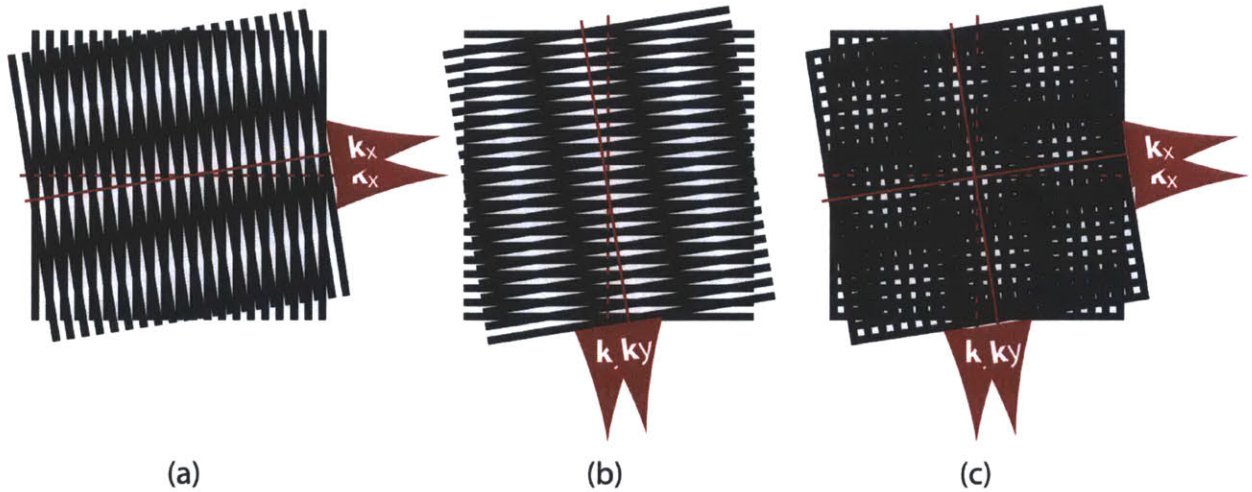


Figure 5.13 Moiré fringes generated by paired periodic patterns that are rotated by 9° and scaled by 2.5%. It is readily apparent that the moiré pattern displayed in (c) is the superposition of those in (a) and (b). Note that the moiré fringes are aligned to the difference vector formed between paired spatial frequency vectors.

of the membrane and screen overlap, the difference vectors generated between the overlapping $\mathbf{k}_x$ and $\mathbf{k}_y$ vectors contains information about the angular orientation between the membrane and screen. Combined with the water holes in the screen, the phase of the moiré pattern references the shift of the membrane relative to the screen.

A membrane's position when dried onto the screen is arbitrary; however the rotation angle of the membrane to the screen can be calculated from the moiré fringe period, provided the membrane pitch and the nitride pitch are known. The membrane pitch of 714.59 nm was measured from the diffraction angles of 325-nm-light. Similarly the screen pitch was measured at 708.86 nm. Equation 15 describes the fringe period $p_f$ with respect to the membrane pitch by $p_m$, the screen pitch by $p_s$ and their respective rotation angle $\theta$ as:

$$p_f = \frac{p_m p_s}{\sqrt{p_m^2 - 2p_m p_s \cos\theta + p_s^2}} \tag{15}$$

In order for the secondary referencing approach to work, the rotation angle between the membrane and screen needs to be small enough ~0.5° that the ISPI scopes still pick up the back-diffracted light from the screen. For the measured periods, this means that the moiré pitch needed to be larger than 60 μm. Also, the 640 pixel × 480 pixel (~1 μm/pixel) field of view of the 10X 0.28 NA Optem microscope used to image the moiré pattern could easily capture moiré periods between 60 μm and 600 μm, provided there was a way to rotate the membranes on the screen

Figure 5.14 shows a time sequence of a membrane rotated on the screen by directed air flow from an $N_2$ gun. With the air gun, the membrane can be rotated and

light diffracted from the membrane and screen give clear signals of the membrane's orientation on the screen. At the start – in the upper pane of the image – the membrane floats on a puddle of water on the screen, the flash light is not used and the screen diffracts room light. At 0s diffracted light from an LED flashlight appears from the screen as an additional diffracted order. At 17s the light diffracted from the screen is joined by light diffracted from the membrane and at 31s the membrane has rotated past.

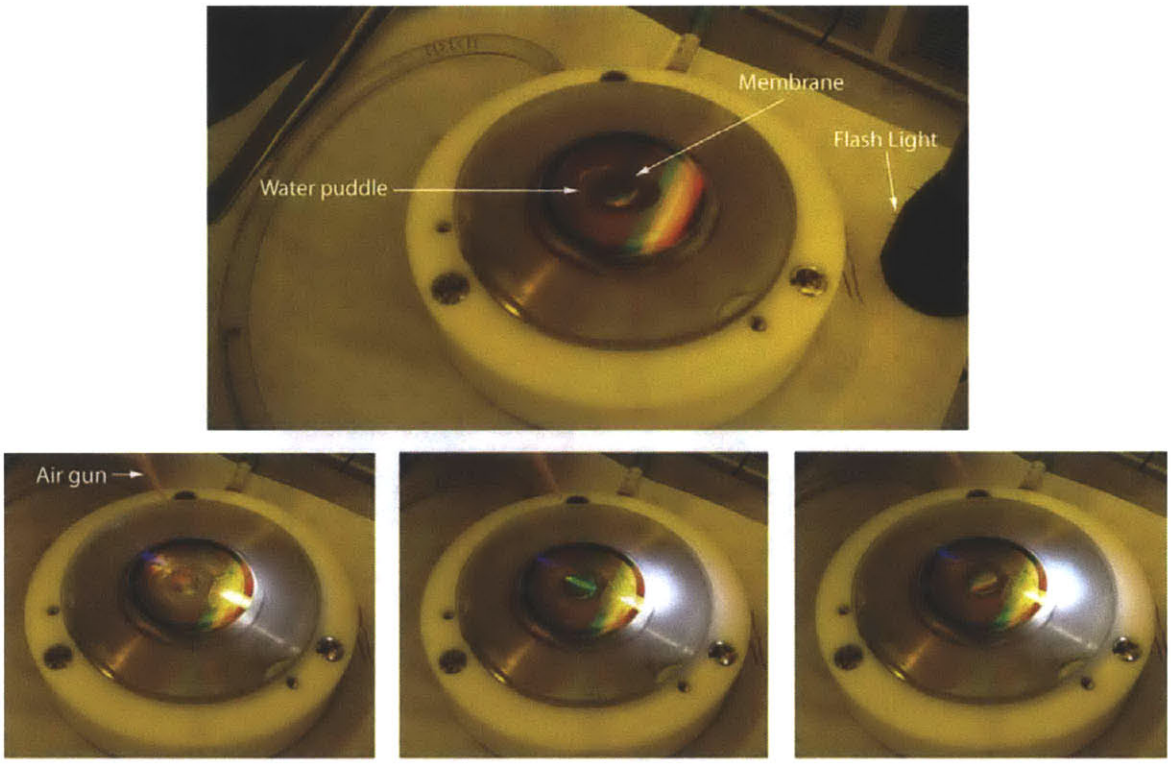


Figure 5.14 A sequence showing the membrane rotated clockwise by an air gun. The top image shows the floating membrane as illuminated by the overhead lighting. In the bottom three images, the membrane is illuminated by a flashlight from the right. At 0 seconds and 31 seconds, the diffracted light from the membrane comes from the (extended) overhead room lighting. At 17 seconds the flash light diffracts from both the membrane and the screen, which are seen coming into rotational alignment.

In order to orient the membrane to less than 0.5° a normally incident Ar-ion laser was used. The multi-line source was projected back from both the membrane and nitride onto the transparent viewing card shown in Figure 5.15. In Figure 5.15a, the

card was coded with red, black and gray lines to demarcate 45°, 5° and 0.5° rotations respectively. In Figure 5.15b-d, the card was modified by cutting out its central region to facilitate rotation via air flow. In Figure 5.15b, the membrane was floating approximately 2° off from the nitride. In (c) the membrane rotated counter-clockwise to the next gray tick 5° away and in (d) the membrane had been rotated back into alignment. Getting the membrane to remain within 0.5° while water was retracted was sometimes tricky (sometimes requiring hours). Alternating the air gun accelerated and decelerated the membrane's rotation and once it slowed down enough the air gun was brought normal to the surface to dry it down onto the screen.

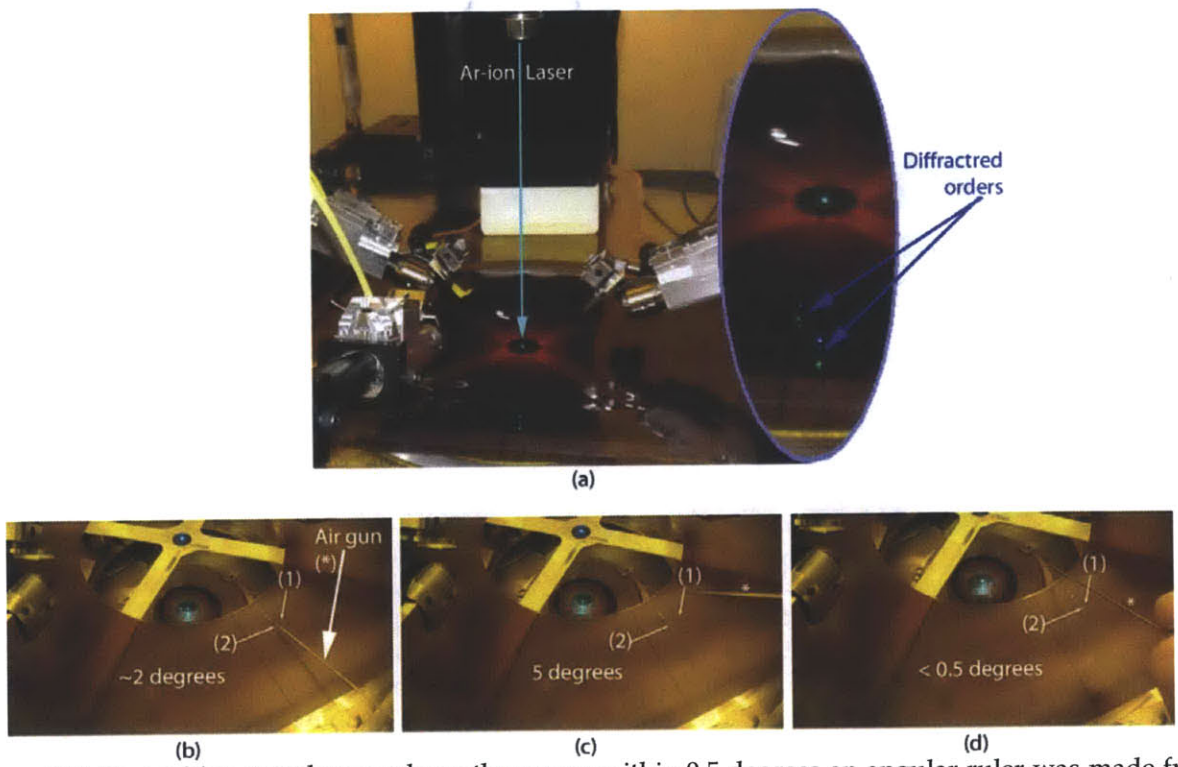


Figure 5.15 To position membranes above the screen within 0.5 degrees an angular ruler was made from a transparency. On the transparency, black lines were spaced every 45 degrees, gray lines every 5 degrees and red lines every 0.5 degrees. (a) A normally incident multi-line Ar-ion laser diffracts from two periodic structures casting linear arrays of dots onto the transparency. (b) An air gun points at the diffracted orders from a floating membrane (2) which is roughly ~2 degrees from the diffracted order from the screen (1). (c) As the air rotates the membrane, the diffracted orders (2) move to 5 degrees from (1). (d) Changing the angle of the air gun rotates the membrane back, bringing the diffracted orders into alignment.

The moiré could also be used to encode the relative phase shift between the membrane and water holes in the screen. This is accomplished by measuring the phase shift of the moiré fringes relative to a fixed location on the screen. These phase shifts were measured along the x- and y-directed grating vector directions to determine how to move the stage. A slight complication arose because the grid patterns made with interference lithography were not perfectly orthogonal and hence the moiré patterns were also not orthogonal. This is shown in Figure 5.16.

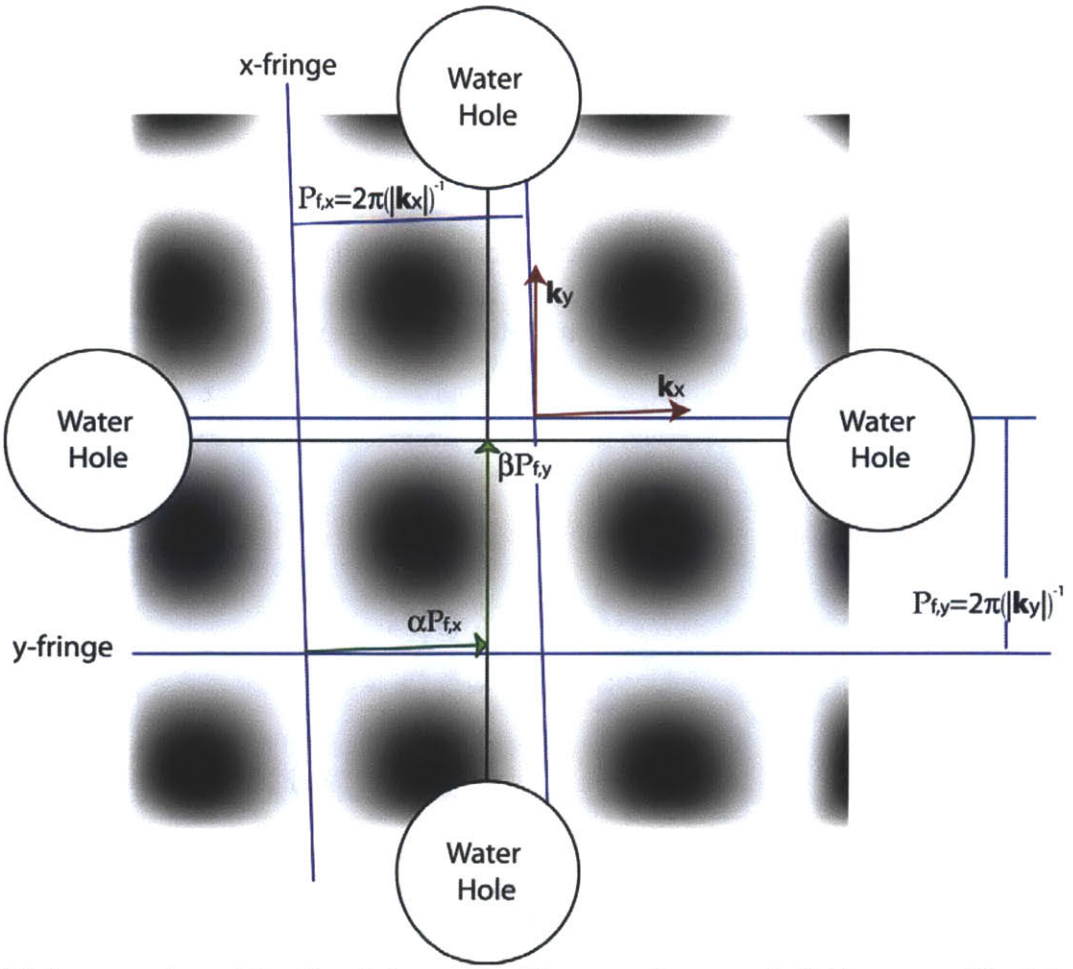


Figure 5.16 An example moiré pattern between the silicon membrane and nitride screen. The intersection of the x-and y-fringes relative to the centroid of the water holes is measured in terms of the phase shifts α and β – along the direction of the spatial frequency vectors $\mathbf{k}_x$ **and** $\mathbf{k}_y$. Combined with the fringe period, which describes the rotation between the nitride and silicon, α and β dictate the displacement of the moiré fringes, and hence the silicon membrane, from the center of the four water holes.

Two membranes were aligned following this approach. Their respective moiré patterns are shown in Figure 5.17. The (x, y) phase shift of the first membrane with respect to the centroid of the water holes was measured at (61.1%, 68.1%) and the second membrane had an (x, y) phase shift of (21.6%, 63.8%) of a fringe. However the fringes were not aligned to the stage axes, rather the fine pattern on the screen was aligned to the ISPI scopes - and hence the stage, which meant that these percentages had to be transformed into the displacements with respect to the stage axes. So, for the membranes whose moiré is shown in Figure 5.17, to align the first membrane to the centroid of the water holes required a shift of $\Delta x_1$=433.7 nm, $\Delta y_1$=482.5 nm and a rotation of $\Delta\theta_1$=582 arc-sec. Similarly, the second membrane required $\Delta x_2$=153.3 nm, $\Delta y_2$=452.6 nm and $\Delta\theta_2$=-62 arc-sec. Instead of translating the first membrane, it was stacked and the second membrane was translated by $\Delta x_1 - \Delta x_2$, $\Delta y_1 - \Delta y_2$ and $\Delta\theta_1 - \Delta\theta_2$.

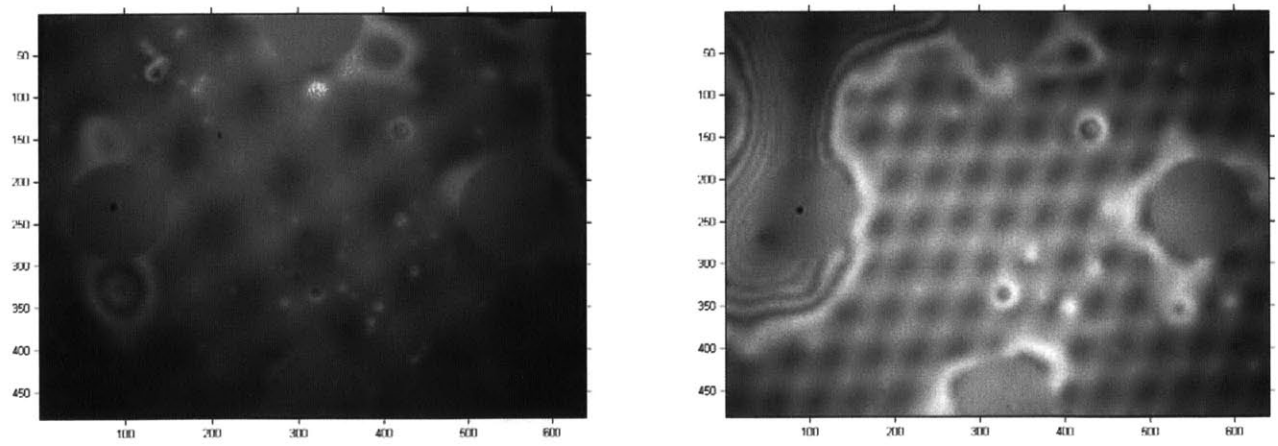

(a) (b)

Figure 5.17 Moiré images between the screen and two aligned membranes. Each image shows the same four holes of the silicon nitride screen. The water holes in the screen are clearly visible and while undesirable, the particulates match in each image, verifying that the same spot was imaged. The axes are in units of microns and each image is rotated to square up the water holes for image analysis. Fringes are analyzed in spatial frequency and orientation. The fringe period relates the membrane angle relative to the screen and the phase of the fringes relative to the centroid of the water holes relates the translation of the membrane grid relative to that on the screen.

The second membrane was aligned and subsequently translated in preparation for stacking. When it was in position, water was observed to condense on the receiving substrate and it detached portions of the first stacked membrane. The re-release of the first membrane presumably destroyed its alignment to the receiving substrate but the second membrane was stacked regardless. A 10X optical micrograph of the moiré pattern that resulted from the two stacked membranes is shown in Figure 5.18. The fringe periods are visibly different and the larger fringe period corresponds to a rotation error of 4.36 mRad of rotation while the smaller period corresponds to 6.65 mRad of rotation. The reason the fringe periods are different is described in Figure 5.19. In Figure 5.19 a grid pattern is depicted in which the x-fringes are rotated by 2 degrees from the y-fringes. Then, in Figure 5.19b, this grid is rotated 9° (compare to Figure 5.13c) and superimposed onto an un-rotated copy. Then in Figure 5.19c the grid is rotated instead by 99° over an un-rotated grid. Because the silicon membrane grids are not orthogonal different spatial frequencies arise in the moiré pattern depending on which grating vectors interfere.

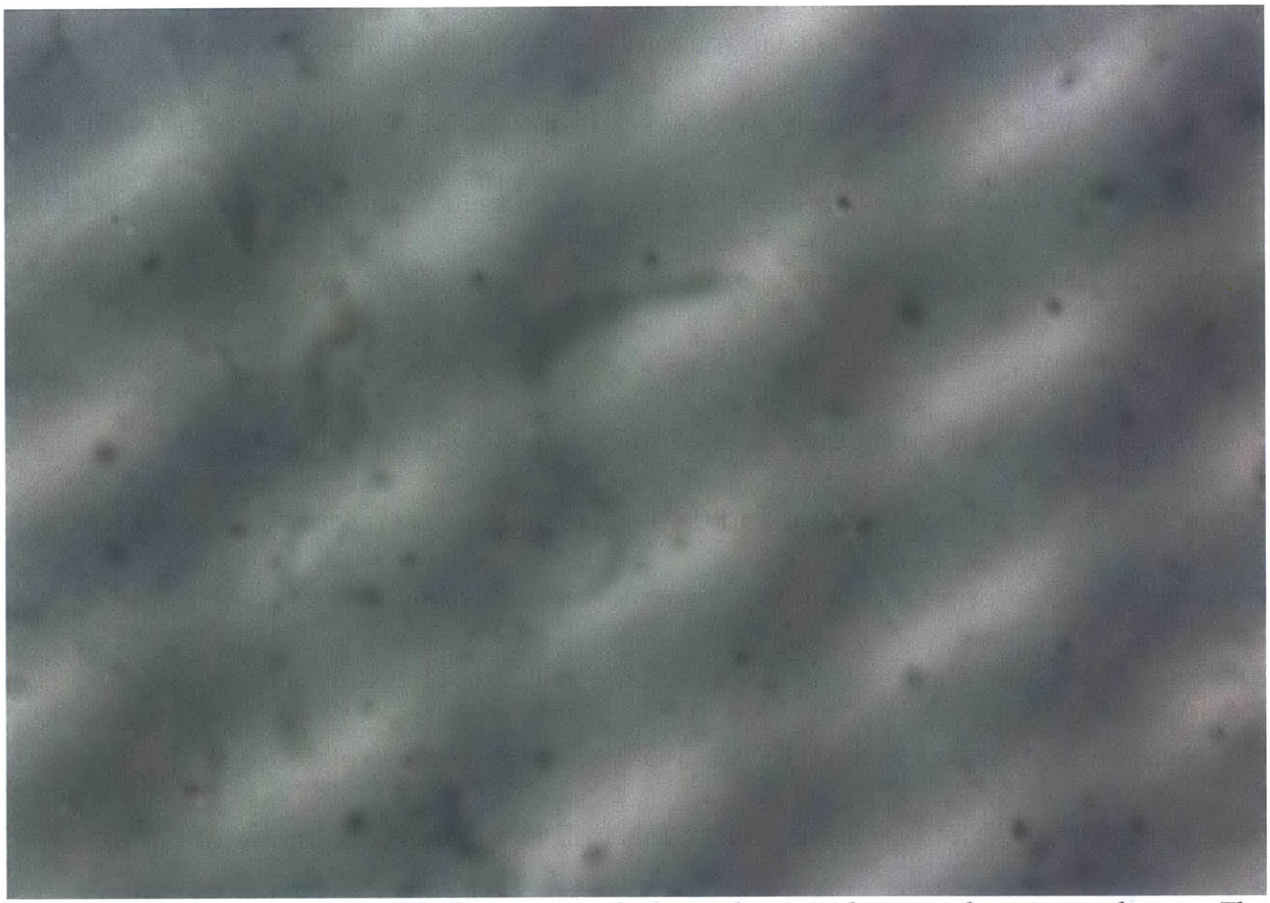

Figure 5.18 As aligned and stacked, this micrograph shows the moiré between the two membranes. The larger moiré period is 163.75 μm and the small fringe period is 107.42 μm. The membrane grid period was measured at 714.59 nm, which gives the rotation angles between membranes. The angle that corresponds to the larger period is 4.36 mRad and for the smaller period it is 6.65 mRad. The grids are not orthogonal so there was an undetermined rotation between the membranes' orientation on the screen.

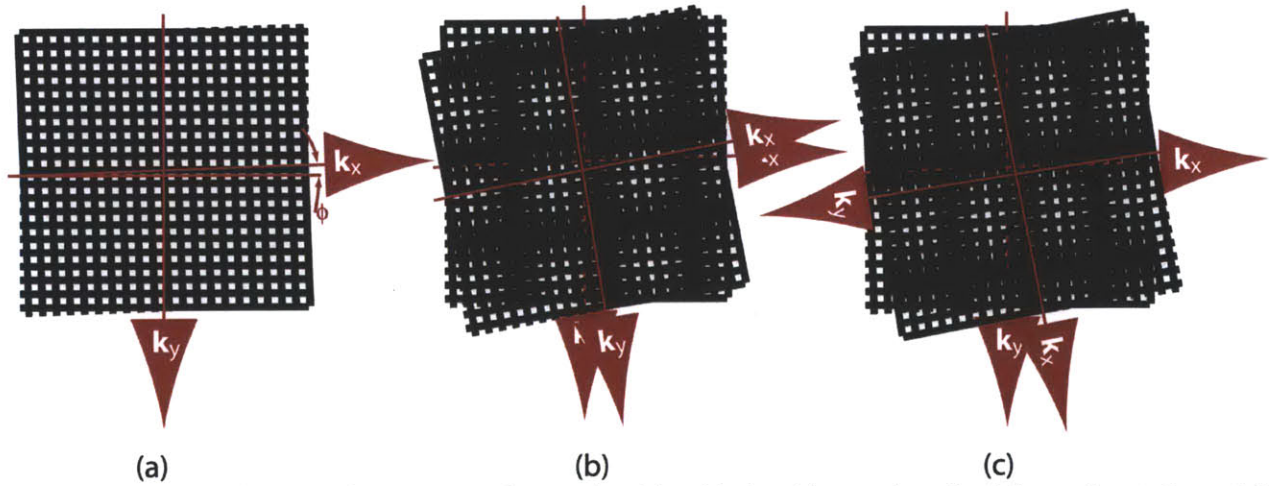


Figure 5.19 Moiré diagram for a non-orthogonal grid. (a) the fringes described by x-directed spatial frequency are rotated by $\varphi$=2° while the fringes described by the y-directed spatial frequency vector are not. Hence, $\mathbf{k_x}$ and $\mathbf{k_y}$ are rotated by 92°. (b) When two grids are rotated by 9° a moiré pattern is generated that has fringes with the same periodicity. However in (c) the rotation of the grids by 99° gives rise to different fringe periods.

Clearly, there are challenges still to be overcome before precise alignment of multiple stacked membranes is possible. Though each of the approaches outlined in this chapter were limited by the water problem, the techniques to align them should still apply. In the align-step-and-stack approach, though water leaked through the holes in the membrane, interference lithography was shown to be sufficient for generating periodic patterns that could be seen by the ISPI scopes and the translation of the stage using its native encoders was within the target alignment tolerance of 10% of the membrane pitch. In the secondary referencing approach, the registration of non-orthogonal grids further complicated the approach, however the moiré pattern between the membrane and screen was analyzed and converted into the required stage movements.

# Chapter 6. Summary and future work

Previously, techniques were presented to fabricate and manipulate free-floating membranes that were then stacked onto a receiving substrate directly from water and from carrier substrates. While studying methods to align membranes, it was discovered that while the surface tension was useful to manipulate and float membranes in some ways water was detrimental to precision stacking due in large part to oxidation of silicon. This chapter summarizes the work in chapters 1-5 and concludes these realizations by investigating changes to the membrane pattern during different stages of the aforementioned processes to further motivate the fabrication process from Chapter 1 that should be executed as future work.

a. **Summary**

Chapter 1 identified key technological limitations that could be addressed by developing the membrane stacking approach. The *element-by-element, all-in-one* and *layer-by-layer* approaches suffered from different limitations that are addressed by nanomembrane stacking paradigm. These include increased throughput and the ability to inspect damaged layers of the structures while also enabling the incorporation of arbitrarily patterned membrane layers.

Chapter 2 considered many different structures and fabrication approaches to determine how to make large-area Si membranes that could be stacked to form a 3D photonic crystal. It included comparisons between SOI and non-SOI starting substrates as well as different interferometric lithography methods, of which a new technique

called Coherent-diffraction Lithography was implemented to reproducibly replicate the pattern on a phase mask. A meshpile photonic crystal structure design was ultimately chosen and a reliable membrane fabrication process was executed that produced large-area membranes held flat to the surface of hydrofluoric acid.

Chapter 3 theorized about the mechanisms by which membranes float and observed hydrostatic fluidic effects including porosity of patterned membranes and oxidation of submerged silicon. Water-based handling techniques were embraced to transfer, move, position, store and dry membranes. These techniques enabled the free-floating membranes to be manipulated and suitably constrained for the subsequent stacking processes.

Chapter 4 addressed membrane stacking techniques. The sub-micron-thick membranes were stacked from the surface of water while surrounded by fixed and variable annuluses. However, in these they were observed to drift about and so instead stacking was attempted from a rigid glass carrier with a single hole, but water leaked through. Buckle-free membranes were stacked from a silicon nitride screen and from a vaporizable adhesive; the adhesive was also sublimed to show a clean low-stress release process.

Chapter 5 described the alignment problem and described two techniques that circumvent it. The direct-referencing alignment approach with a glass carrier was attempted and evidence that every step is feasible was shown except, upon stacking, water permeated the membrane pores precluding its adhesion to the receiving substrate. The secondary-referencing alignment approach based-on a nitride screen

was implemented but was limited by water re-releasing the first stacked membrane. Moreover the orthogonality error of the membrane and nitride patterns challenged the requisite complicating this approach.

In these approaches, for the first time interference lithography generated the checkerboard patterns that were used within the ISPI alignment scheme. The target periodicity of the IL-made $P_2$ mark deviated from the target 1-μm-pitch checkerboard which led to different frequency fringe patterns and reduced the alignment accuracy; however this was not a fundamental limitation. These alignment approaches were not extended to the sublimable glue because the alignment apparatus was not designed to accommodate hazardous materials or elevated temperatures. In the next section on future work, the secondary-referencing aligned stacking scheme using a sublimable adhesive is revisited after data is presented about membrane distortion during the water-based stacking experiments.

b. **Future work**

Mechanical stress within the membranes changed throughout the creation of the SOI wafers through the stacked membranes[8]. In the flowchart of Figure 6.1 are the

[8] During their manufacture, the SOI wafers cooled more than 1000 °C. Silicon has a larger coefficient of thermal expansion than $SiO_2$ which caused the silicon device layer to try to contract more than the $SiO_2$ interlayer allows. Thus before touching the SOI wafers, the silicon membrane layer developed compressive stress from their manufacture. Then the patterned silicon was bonded at ~400 °C to borosilicate substrates and the thick handle wafer was etched away. When a membrane was released from the borosilicate to float on water surface tension pulled the membrane flat. Then transferred, either to the water-based stacking apparatuses on a Teflon screen or to the carrier-based apparatuses on a cover slip, the membranes patterns could have deformed as a result of transfer. Finally, stacking the membranes could also have distorted their patterns.

various stages of membrane fabrication and stacking steps where the periodicity of the membranes could be measured.

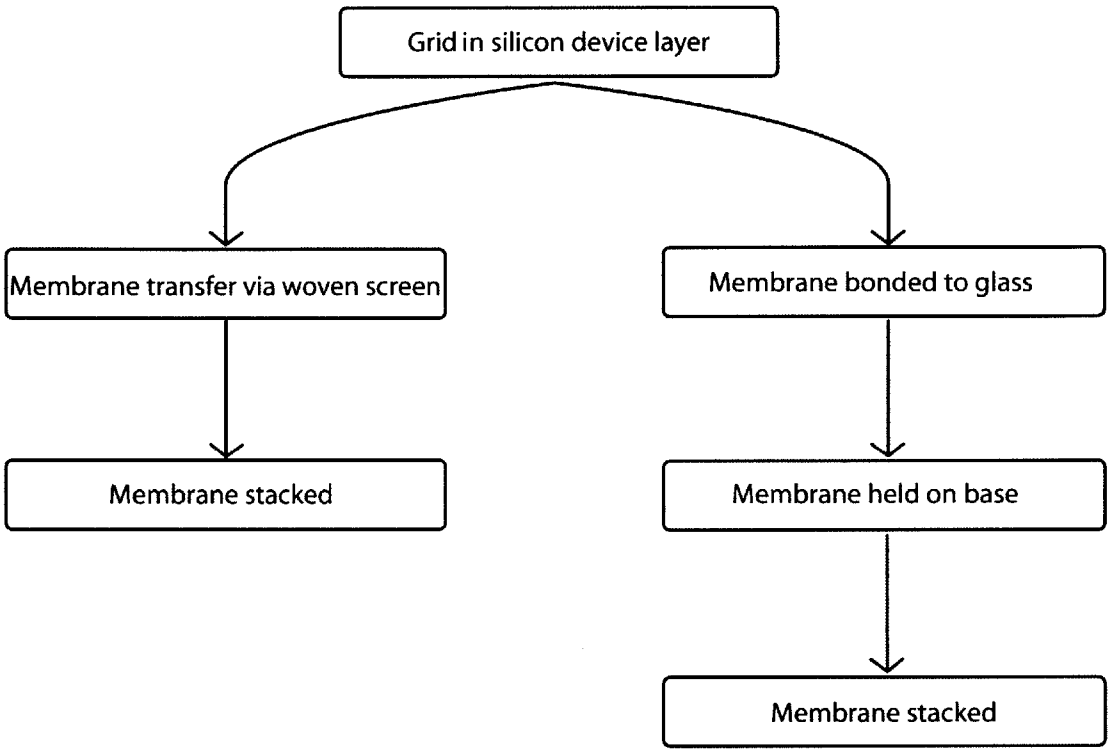


Figure 6.1 Process stages for the different stacking approaches. Initially, the grid pattern exists in the silicon device layer of the SOI wafer. Then along the left branch, describing the water/annulus stacking of Chapter 4, the membranes were released directly from the SOI wafer (at a yield of 16%), then carried to the stacking apparatus on a woven screen where they were stacked. Along the right branch, the membranes were bonded to a glass handle (yield ~100%) after which they released and floated until being dried onto the base of the stacking apparatus (either a silicon nitride screen or glass cover slip). Once they were on the base, the membranes were stacked.

For samples within each of these stages a set of five 100X microscope images were analyzed in the Fourier domain to calculate the membrane pattern's periodicity and orthogonality. Figure 6.2 shows an example 100X microscope image of the patterned SOI wafer and the superposition of the (five) Fourier transforms for the images taken for the SOI sample. For this grid pattern, as described previously, the diffraction of 325-nm-light indicated that it had a pitch of 714.59-nm. Its Fourier transform contained the spatial frequencies for the grid pattern and these could be

compared to determine the orthogonality of the grid. Moreover, superposition of the Fourier transforms of the microscope images taken for a given sample would indicate, to some extent, if there were any distortions in the membrane patterns.

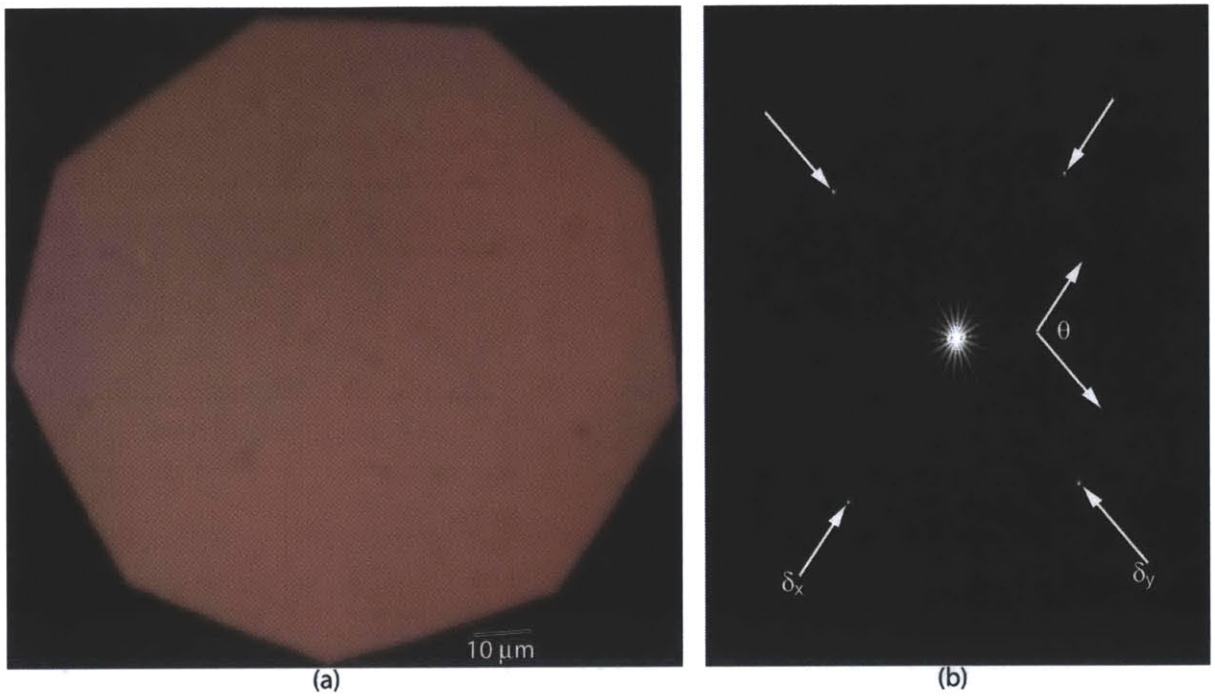


Figure 6.2 Measurement approach. 100x optical micrographs of the patterned grids in silicon were captured for samples in each of the steps described in Figure 6.1. One such image is shown (a). Then for each step of Figure 6.1, each micrograph was transformed to its frequency domain and then the resulting amplitudes were superimposed (b) to identify changes in the patterns over several samples within each step. In the Fourier domain, each image was analyzed to provide the orthogonality $\theta$ of the grid and the distances $\delta_x$ and $\delta_y$ between spatial frequencies of each periodic component of the grid pattern.

Initially, the pitch of the membrane was targeted to ~660 nm as this would lead to a photonic crystal operating over the telecomm wavelength and these membranes were stacked from water. As the work progressed to consider alignment techniques the membrane pitch was adjusted to interfere with the ISPI marks, i.e. to ~707 nm. In the following tables, the measured values of the membrane pitch and orthogonality are presented for these two design periodicities. The measurement error, based on mis-

measuring the peaks in the Fourier domain of Figure 6.2b by 1 pixel, corresponded to a change in the pitch of 0.28% and a change in the angle by 0.4%.

| Step | X-directed pitch (nm) | Y-directed pitch (nm) | Orthogonality error (mRad) |
|---|---|---|---|
| Grid in silicon | 645.54 | 645.10 | -2.035 |
| Membrane on Teflon | 99.834% | 99.832% | 362.494% |
| Sacked, fixed corral | 99.869% | 99.778% | 78.0365% |
| Stacked, variable corral | 100.094% | 100.001% | 80.5759% |

Table 6.1 The pitch and orthogonality errors for steps along left path of Figure 6.1. The orthogonality error describes the grid's deviation from perfect orthogonality.

| Step | X-directed pitch (nm) | Y-directed pitch (nm) | Orthogonality error (mRad) |
|---|---|---|---|
| Grid in silicon | 714.59 | 714.59 | -2.38 |
| Membrane bonded to glass | 99.2570% | 99.0012% | -0.0003% |
| Membrane on glass base | 99.5741% | 99.1500% | -0.0004% |
| Membrane stacked from $SiN_x$ | 99.6280% | 99.2574% | -0.0003% |
| Membrane stacked from $SiO_2$ | - | - | - |

Table 6.2 The pitch and orthogonality of the grid changed as the right path of Figure 6.1 was executed. Clearly, the change in orthogonality is negligible.

These results show that in addition to water being a problem from the stacking perspective, the change in the membrane pattern is non-negligible when they are transferred to and stacked from carrier substrate. Also, the process of drying the membrane onto a carrier affected the membrane periodicity less than the compressive stress from the manufacture of the SOI wafers. The orthogonality error for the membrane on Teflon is large because the membrane was strongly affected by the undulation of the woven mesh. This is contrasted by the carrier-based approach in which the orthogonality error did not change.

With an appropriate adhesive, perhaps pentacene, it may be possible to entirely circumvent these issues as described in the following figures. First, in Figure 6.3 the

wafer that will become membranes is glued – via a vaporizable bonding agent - to a carrier at relatively low (<400 °C) temperatures.

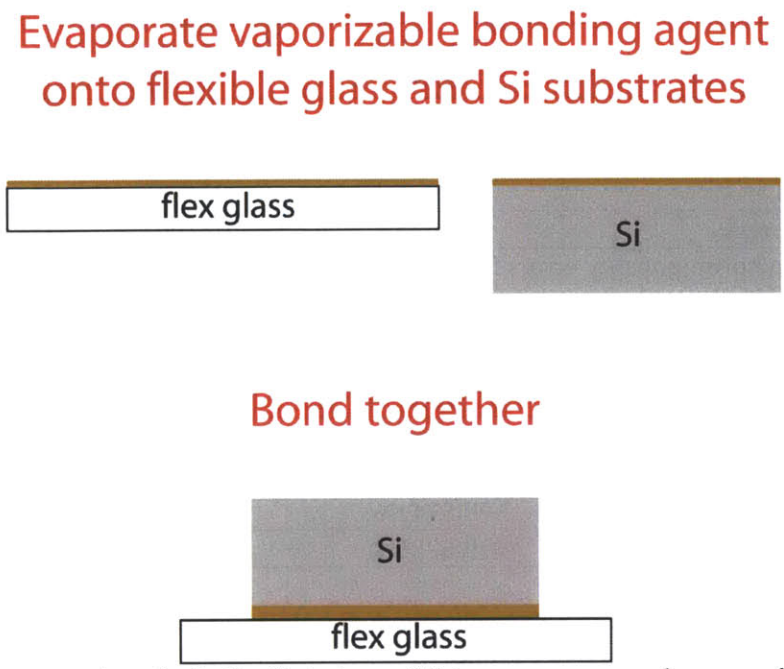


Figure 6.3 Refined process stage 1. In the first stage of this process, a membrane wafer and carrier wafer are each coated with an adhesive and then bonded together.

Then, in Figure 6.4 the membrane layer would be defined. The thick silicon wafer is first thinned by grinding, polishing and possibly etching to the appropriate thickness after which planar fabrication steps would pattern the requisite features in the (potentially disjoined) membrane alongside the secondary-referencing alignment marks. There are several virtues to this process so far. First the membrane layer would be formed without the need for high temperature processes. Though silicon membranes are described in the figure the membrane layer can be any material as long as the glue withstands the thinning process. Finally, because the patterning process creates the alignment features alongside the rigidly-held membrane pattern no realignment should be necessary.

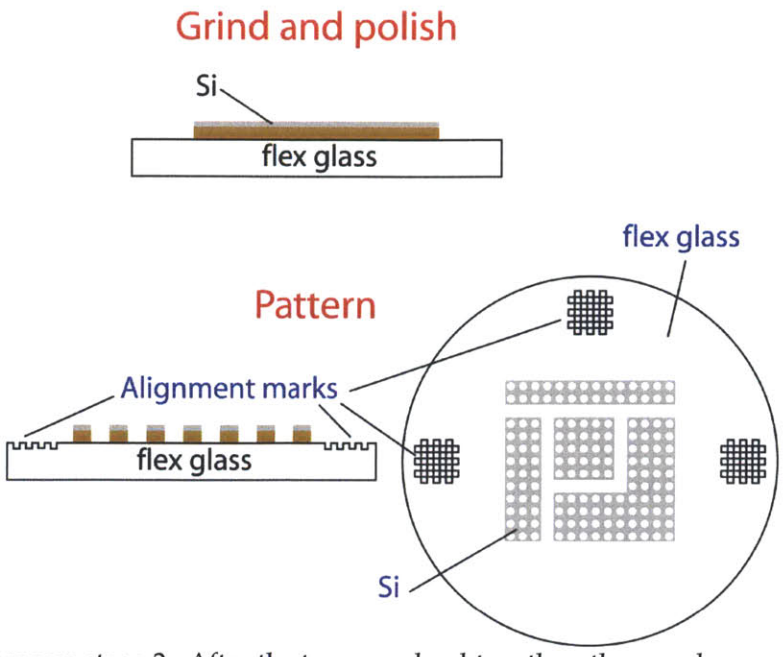


Figure 6.4 Refined process stage 2. After the two are glued together, the membrane wafer is ground and polished and/or appropriately thinned by additional etching to form the plain membrane sheet. Subsequent processing would define the requisite patterns in the membrane sheet and create a set of secondary-referencing marks on the carrier substrate.

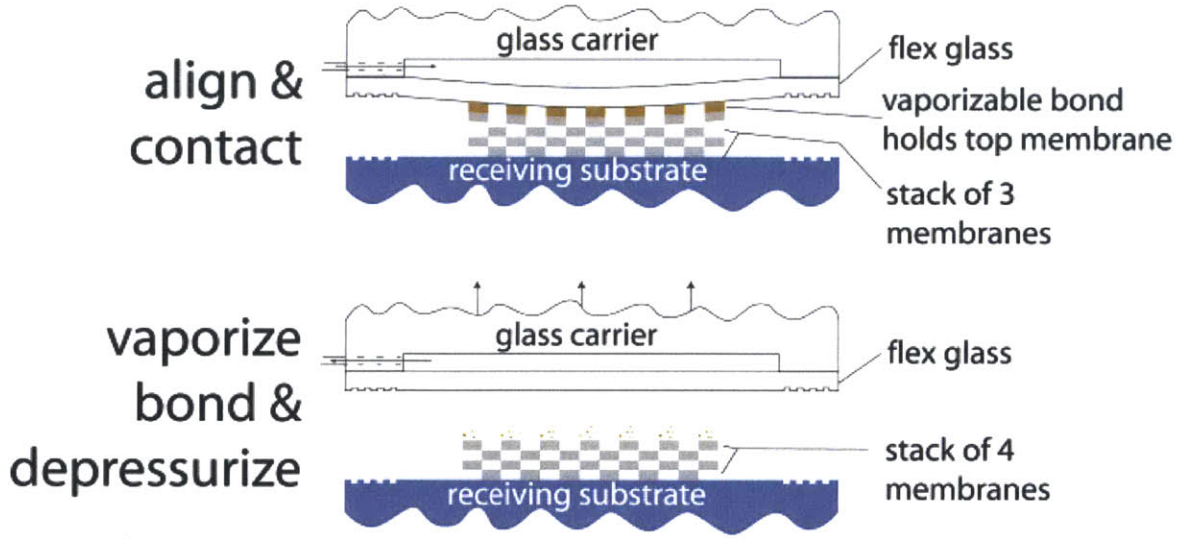


Figure 6.5 Refined process stage 3. The flexible glass is mounted to a carrier and after it is aligned to the receiving substrate the flexible glass is bulged to contact the membrane to the underlying stack of membranes on the receiving substrate. Once in intimate contact, the bond is sublimated to eliminate the membrane's adhesion to the flex glass.

As described in Figure 6.5, the flex glass and carrier would be interferometrically aligned to the receiving substrate. Similar to the contact and imprint lithography, pressure applied to the flex glass would bulge it to cause intimate contact between the

membrane and receiving substrate. At elevated temperatures, or potentially using light [45], the sublimable (or photodegradable) glue would dissipate to release the membrane from the carrier to the receiving substrate. Once the membrane is stacked, the pressure is released and another membrane would follow.

There are several intriguing possibilities with this approach that should be investigated further. Furthermore, many of the technological requirements exist: grinding/polishing, wet/dry etching and/or oxidation have been used to thin a wafer considerably. Moreover, the planar process is flexible enough that it should be possible to pattern the membrane and alignment marks while maintaining their registration. Also, the aligned contact process exists in a slightly different form as imprint lithography. Unfortunately, shown in Figure 6.6, naphthalene has a higher vapor pressure than its more resilient counterparts, which makes it insufficiently unstable as an adhesive for planar processing- at 0 °C the vapor pressure is 2.6 mTorr.

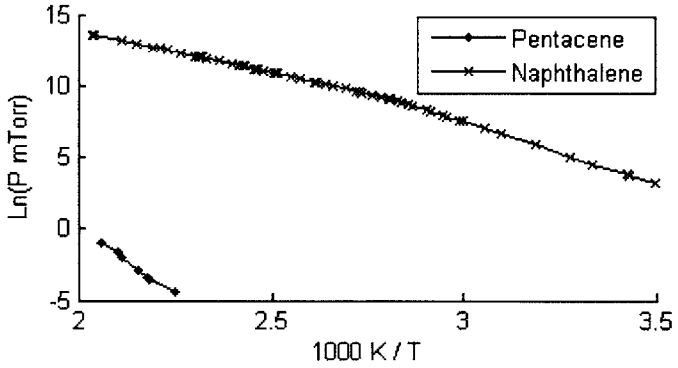


Figure 6.6 The vapor pressure of Pentacene as function of temperature. At RIE process pressures, naphthalene fails, however as long as the temperature remained less than ~170 °C or pentacene would not sublimate. (pentacene data was obtained from [46] and naphthalene data obtained from the Dortmund data bank)

Pentacene could replace naphthalene but the bonding process remains to be demonstrates. This is an attractive thrust for future work.

# Appendix

## a. Fabrication of photonic structures

### i Rod-Hole membrane

Table 6.4summarizes the fabrication steps used to prepare, pattern and transfer a pattern of holes into the device layer of an SOI wafer. The SOI wafers were first cleaned in a bath of piranha and RCA to remove any metallic contaminants or organic films. A steam nucleation test then confirmed that they were clean. The substrates were prepared for lithography with a stack of oxide, ARC, oxide and PS4 photoresist. Then, two orthogonal IL exposures, the subsequent post-bake and development in CD-26 created an array of holes in PS4, which was then transferred through the silicon device layer using reactive-ion etching steps.

| | **Initial substrate: 500 µm Si : 400 nm $SiO_2$ : 350 nm Si** | |
|---|---|---|
| **Process Station** | **Process Description** | **Targets Parameters** |
| Wet Bench | Piranha Clean | 20 min in (4) $H_2SO_4$ : (1) $H_2O_2$ |
| Wet Bench | RCA Clean | 15 min @ 75°C – 85 °C in (4) $H_20$ : (1) $NH_4OH$ : (1) $H_2O_2$ |
| Spinner & RTP | Layer 1: FOX-25 | 500 nm (5 krpm)* |
| Spinner & Oven | Layer 2: Barli | 250 nm (4.10 krpm) |
| Evaporator | Layer 3: $SiO_x$ | 25 nm (0.5 nm / min) |
| Spinner | Deposit HMDS | puddle: wait 1 min, spin 5 s at 3.8 krpm, wait 5 min |
| Spinner & Oven | Layer 4: PS4 | 180 nm (3.8 krpm) |
| Lloyd's*, PEB & dev. | Pattern PS4 | 15.6 mJ/Area, 325 nm, ~660 nm pitch ~0.173 mW/A** |
| RIE NSL | RIE $SiO_x$ | 2 min |
| RIE NSL | RIE Barli | 6 min |
| RIE NSL | RIE FOX-25 | 15 min |
| RIE SNL | RIE Si | 600 s, 10 mTorr, 100W*** |
| (optional) Wet Bench | HF release Si | 15 min in 49.9 % hydrofluoric acid |

Table 6.3 The fabrication steps for fabricating a membrane with a layer of holes. * The FOX-25 was expired and spun thicker than expected. ** The power detector was placed perpendicular to the optical axis of the beam at the center of the Lloyd's mirror stage and the power at the wafer was different on different days so the time was adjusted accordingly. *** The plasma therm etcher underwent a rewire and software upgrade and the 10 mTorr, 100W process conditions were abnormally high for this step.

After patterning and pattern transfer processes the samples were cleaned and prepared for the second lithography step to produce the rods pattern described in Table 6.4. ARC was spun (and baked) twice to planarize the surface above for lithography. Then $SiO_x$ was evaporated, HMDS applied and positive-tone PFI-88 spun in preparation for lithography. The Lloyd's mirror generated a pattern of rods that was

slightly different pitch than the holes. Then this pattern was transferred by a series of RIE steps into the silicon.

| Initial substrate: 500 μm Si : 400 nm $SiO_2$ : 350 nm Si (Patterned) : 175 nm residual HSQ mask | | |
|---|---|---|
| **Process Station** | **Process Description** | **Targets Parameters** |
| Wet Bench | Piranha Clean | 20 min in (4) $H_2SO_4$ : (1) $H_2O_2$ |
| Spinner & Oven | Spin Barli | 225 nm (5.75 krpm) |
| Spinner & Oven | Spin Barli | 225 nm (5.75 krpm) |
| Evaporator | Evap. $SiO_x$ | 25 (0.5 nm / min) |
| Spinner | Deposit HMDS | 1 min wait, 5 sec spin; 3.8 krpm |
| Spinner & Oven | Spin PFI-88 | 180 nm (3.8 krpm) |
| Lloyd's Mir. & dev. | Expose PFI-88 | 34.7 mJ/ Area, $\lambda$= 325 nm, $p$~660 nm x2 0.193 mW/ A |
| RIE NSL | RIE $SiO_x$ | 2 min |
| RIE NSL | RIE Barli | 8 min |
| RIE NSL | RIE FOX-25 | 4¾ min |
| RIE SNL | RIE Si | 600 s, 2mTorr, 40W |
| Wet Bench | HF release Si | 15 min in 49.9 % hydrofluoric acid |

Table 6.4 The fabrication steps for fabricating the layer of rods overlaid onto the layer of holes. *The power detector was placed perpendicular to the optical axis of the beam at the center of the Lloyd's mirror stage and the power at the wafer differed day-to-day.

**ii** CDL Mask fabrication

The pattern of ISPI marks was written in PMMA on a Cr-coated fused silica optical flat. The PMMA on 25 nm Cr was exposed at a dose of 600 μC $cm^{-2}$, developed in a mixture of 3 parts Methyl Isobutyl Ketone (MIBK) to 2 parts isopropanol (IPA) at room temperature for 1 minute, rinsed in deionized water and then dried with $N_2$. The result was hard baked at 180°C for 30 min, wet-etched in chrome etchant, Cr-7 (perchloric acid and ceric ammonium nitrate) until the pattern cleared, then rinsed in DI water and again dried with $N_2$. This mask then was used to pattern conformable daughter masks.

The 0211-glass conformable masks had 25 nm of Cr coated with a trilayer stack consisting of 180 nm PFI-88, 50 nm $SiO_x$ and 225 nm Barli. A trilayer stack was chosen because the combination of $SiO_x$:Barli had a better selectivity during subsequent pattern transfer steps. Each was patterned in the Tamarack (exposed for ~17 seconds using a mercury lamp), and reactive-ion-etched using the trilayer etching process described previously. The pattern was transferred into chrome using a mixture of $Cl_2$ (20sccm) and $O_2$ (10sccm) at 5 mTorr, 100 W and a bias between 319 V to 346 V for 600s (etch rate

~3nm/min). Once the $SiO_x$ and Barli were stripped these were then used to pattern the borosilicate masks prepared and processed according to Table 6.5

| Initial substrate: 5 mm thick, 5 cm diameter Borosilicate glass | | |
|---|---|---|
| **Process Station** | **Process Description** | **Target Parameters** |
| Wet Bench | RCA Clean | 15 min @ 75°C – 85 °C in (4) $H_20$ : (1) $NH_4OH$ : (1) $H_2O_2$ |
| Spinner & Oven | Spin Barli on Front | 200 nm (7.28 krpm) |
| Spinner & Oven | Spin Barli on Back | 300 nm (3.0 krpm) |
| Spinner & Oven | Spin Barli on Back | 300 nm (3.0 krpm) |
| Evaporator | Evap. $SiO_x$ | 25 nm (0.5 nm / min) |
| Spinner | Deposit HMDS | 60 s wait, 5 s spin; 3.8 krpm |
| Spinner | Spin PFI88 | 180 nm (3.8 krpm) |
| Tamarack & dev. | Expose PFI88 | 31.0 mJ/A, UV, 1000 nm pitch |
| RIE | $SiO_x$ | 2 min |
| RIE | Barli | 5 min |
| RIE | $SiO_2$ | 10 min |
| Wet Bench | RCA Clean | 15 min @ 75°C – 85 °C in (4) $H_20$ : (1) $NH_4OH$ : (1) $H_2O_2$ |
| Spinner & Oven | Spin Barli on Front | 200 nm (7.28 krpm) |
| Spinner & Oven | Spin Barli on Back | 300 nm (3.0 krpm) |
| Spinner & Oven | Spin Barli on Back | 300 nm (3.0 krpm) |
| Evaporator | Evap. $SiO_x$ | 25 nm (0.5 nm / min) |
| Spinner | Deposit HMDS | 1 min wait, 5 sec spin; 3.8 krpm |
| Spinner | Spin PFI88 | 180 nm (3.8 krpm) |
| Lloyd's mir. & dev. | Expose PFI-88 | 28.4mJ/A, $\lambda$=325nm, $p$~660nm, 0.18 mW/A |
| RIE | $SiO_x$ | 2 min |
| RIE | Barli | 5 min |
| Protect ISPI marks | Paint Barli | Oven Bake 30 min at 175C |
| RIE | $SiO_2$ | 3 min |

Table 6.5 The fabrication steps to create the phase mask for use in CDL. A '~' is used to denote approximate values.

The borosilicate was contact printed with the flexible daughter mask to transfer the pattern into its PFI-88, which was then transferred into the Barli using the trilayer etching process followed by the $CHF_3$ for 10 minutes to transfer the ISPI marks into the borosilicate. The borosilicate was then cleaned, prepared for IL (again with a thick backside ARC) and patterned using the Lloyd's mirror. After development and another trilayer etch, ARC was painted over the ISPI markers (and subsequently baked) to protect them. Then, the pattern was transferred into the borosilicate, again using $CHF_3$ for 10 minutes. Table 6.5 of the Appendix contains details; etch rates had to be adjusted from the typical values because thicker substrates etch more slowly.

**iii** CDL Patterning

To demonstrate pattern replication using a CDL mask, a substrate was prepared with a standard trilayer stack following Table 6.6 and then exposed at a Talbot distance from the CDL mask.

| Initial substrate: 500 um thick, 100 mm diameter Silicon wafer | | |
|---|---|---|
| **Process Station** | **Process Description** | **Target Parameters** |
| Wet Bench | RCA Clean | 15 min @ 75°C – 85 °C in (4) $H_20$ : (1) $NH_4OH$ : (1) $H_2O_2$ |
| Wet Bench | Piranha Clean | 20 min in (4) $H_2SO_4$ : (1) $H_2O_2$ |
| Spinner & Hotplate | Spin Barli | 200 nm (7.28 krpm) |
| Evaporator | Evap. $SiO_x$ | 25 nm (0.5 nm / min) |
| Spinner | Deposit HMDS | 1 min wait, 5 sec spin; 3.8 krpm |
| Spinner | Spin PFI88 | 180 nm (3.8 krpm) |
| CDL and develop | Expose PFI-88 | 108 mJ/A, $\lambda$=405 nm, $p$=660 nm, 5.4mW/A |

Table 6.6 The fabrication steps to prepare a substrate for coherent diffraction lithography.

**iv** Meshpile Patterning of SOI wafers

To create 1-cm-diameter meshpile structures an SOI wafer was prepared with a hard $SiO_x$ mask followed by a trilayer stack and patterned then with the Mach Zehnder according to Table 6.7.

| Initial substrate: 500 μm Si : 1000 nm $SiO_2$ : 340 nm Si | | |
|---|---|---|
| **Process Station** | **Process Description** | **Target Parameters** |
| Wet Bench | RCA Clean | 15 min; 75°C – 85 °C in (4) $H_20$ : (1) $NH_4OH$ : (1) $H_2O_2$ |
| Evaporator | Evap. $SiO_x$ | 100 nm (0.5 nm / min) |
| Spinner & oven | Spin Barli | 297 nm; (2.95 krpm) |
| Evaporator | Evap. $SiO_x$ | 25 nm (0.5 nm / min) |
| Spinner | Deposit HMDS | 1 min wait, 5 sec spin; 3.8 krpm |
| Spinner & oven | Spin PS4 | 180 nm (3.8 krpm) |
| Mach Z., PEB & dev. | Expose PS4 | 14 mJ/A, $\lambda$=325nm, $p$=707nm, ~0.1mW/A x2*, ** |

Table 6.7 process for preparing an SOI wafer for IL. Wafers are first cleaned, then a layer of $SiO_x$ 100 nm thick is deposited, followed by an antireflection (ARC) layer 297 nm thick, another layer of $SiO_x$ and finally a layer of negative-tone (i-line) chemically amplified resist PS4 at 180 nm thick. *Each beam's power was brought to within 5% of the other and then the power was measured with the detector parallel to the stage with the room lights on (the power density decreases by 10 μW/area with the lights off). **The periodicity was changed to 707 nm to allow the fine grid to be seen directly with the ISPI microscopes.

After development of the photoresist, the wafers were quartered to optimize the pattern transfer and bonding steps. The pattern transfer process is similar to that presented before - i.e., trilayer etching steps followed by transfer through the oxide with $CHF_3$ and finally thorough the silicon with HBr. A final $CHF_3$ etch step was used to strip the 100 nm $SiO_x$ mask from the front side of the device layer silicon. Next the

samples were next prepared for contact lithography to define the membranes by spinning Shipley 1813 resist at 1.0 krpm (i.e. 3 μm thick) and baking them at 110 °C on the hotplate for 90 seconds. Contact lithography at this length-scale is fairly forgiving, so a 90s exposure followed by 60 seconds in MF-321 developer and 60 second DI rinse was sufficient to clear the patterns. The cleared silicon was etched away in $CF_4$ at 300V for 15 minutes.

v $SiN_x$ screen

To fabricate the screen, the x-ray masks were first stripped in a combination of piranha, gold etchant and chrome etchant until only the nitride remained. Next, ~20 nm of XHRiC (Brewer Science) antireflection coating was spun on the backside of the silicon nitride membrane at 6.5 krpm and proximity baked at 180 °C (backside up) on a hotplate for 90 seconds. Following that, PS4 was spun onto the front side of the nitride and baked at 90 °C for 90 seconds also on the hotplate. The nitride membrane was patterned twice with interference lithography at ~12.6 mJ/area for each exposure. The pattern was developed by immersion in CD-26 for 60 seconds and then the pattern was reactive-ion etched into the nitride using $CF_4$ at 20 mTorr, 20 sccm for ten minutes. After IL, the nitride was cleaned again in piranha to remove the patterned photoresist and backside ARC. Then to form the holes in the screen, Shipley 1813 was spun onto the front side at 1.0 krpm (~3 μm thick) and baked on the hotplate at 110 °C for 90 seconds. Contact lithography was used to record the pattern of holes on a chrome mask into the Shipley resist. Exposures were carried out for 90 s at 3.1 mW/area and developed for 60 seconds in MF321. The thick layer of Shipley masked the subsequent, touchy, RIE step. The membrane was intermittently inspected as it was repeatedly etched and for 5 to 10 minutes at 20 mTorr, 200W in $CF_4$. By looking at the backside, it was obvious when the holes punched through.

This process was not a high yield process despite employing several tricks to improve it. The nitride can easily shatter with forces applied in the plane of the nitride and also if enough pressure out of the plane is applied to the entire membrane. In the first step of applying ARC the membrane had to be flipped upside down so the ARC

was up in order that the film remained continuous. If the nitride was placed right-side up the ARC would contract forming an incomplete film that introduced non-uniform in-plane stress. Also, the mounting process that was developed for the interference lithography step circumvented the standard vacuum chuck mounting scheme so that the membrane surface did not deflect (and potentially pop) during an exposure. The glass ring was affixed to an ARC-coated silicon wafer with Unibond wax; Unibond is a liquid at 70 °C and as it cooled it condensed, so an air gap was maintained beneath the glass ring to guarantee that no back pressure deflected the membrane as the wax dried. Also, when immersed in a fluid – water, piranha, developer, etc. – the nitride was always inserted vertically to mitigate any drag force on the membrane. In the contact lithography step, to protect the nitride, three 30 μm thick spacers were placed between the chrome mask and the nitride-on-silicon rim of the membrane. Finally, during the RIE step, the glass ring was placed on cover slips to provide spacers for the vacuum.

| Initial substrate: 1 μm $SiN_x$ mounted to 76.2 mm Pyrex ring | | |
|---|---|---|
| **Process Station** | **Process Description** | **Target Parameters** |
| Wet Bench | Gold strip | 5 min; gold etchant * |
| Wet Bench | Titanium strip | 5 min; ceric ammonium nitrate and perchloric acid* |
| Wet Bench | Piranha | 20 min; 75°C – 85 °C in (4) $H_2SO_4$ : (1) $H_2O_2$ * |
| Spinner & oven | Spin XHRiC-16 | 20 nm; (6.5 krpm) Thinned by Tim Savas; backside |
| Spinner & oven | Spin PS4 | 180 nm; (3 krpm); front side |
| Mach Z., PEB & dev. | Expose PS4 | 12.6 mJ/A, $\lambda$=325nm, $p$=707nm, ~0.1mW/A x2**, *** |
| RIE | $SiN_x$ | 10 min |
| Wet Bench | Piranha | 20 min; 75°C – 85 °C in (4) $H_2SO_4$ : (1) $H_2O_2$ |
| Spinner & oven | Spin Shipley 1813 | 1 um; (3 krpm); front side |
| Tamarack & dev. | Expose S.1813 | ~250 mJ/A, UV |
| RIE | $SiN_x$ | 10 min* |

Table 6.8 Process for preparing a $SiN_x$ screen * repeated as necessary. **Each beam's power was brought to within 5% of the other and then the power was measured with the detector parallel to the stage with the room lights on (the power density decreases by 10 μW/area with the lights off). ***The periodicity was changed to 707 nm to allow the fine grid to be seen directly with the ISPI microscopes.

### b. Derivation of the Talbot effect

$$
\begin{aligned}
I \sim\ & E_{-1}e^{j\left(\omega t-\overline{k_{-1}}\cdot\overline{r}\right)}E_{-1}e^{-j\left(\omega t-\overline{k_{-1}}\cdot\overline{r}\right)} + E_{-1}e^{j\left(\omega t-\overline{k_{-1}}\cdot\overline{r}\right)}E_{0}e^{-j\left(\omega t-\overline{k_{0}}\cdot\overline{r}\right)} + E_{-1}e^{j\left(\omega t-\overline{k_{-1}}\cdot\overline{r}\right)}E_{+1}e^{-j\left(\omega t-\overline{k_{+1}}\cdot\overline{r}\right)} + \\
& E_{0}e^{j\left(\omega t-\overline{k_{0}}\cdot\overline{r}\right)}E_{-1}e^{-j\left(\omega t-\overline{k_{-1}}\cdot\overline{r}\right)} + E_{0}e^{j\left(\omega t-\overline{k_{0}}\cdot\overline{r}\right)}E_{0}e^{-j\left(\omega t-\overline{k_{0}}\cdot\overline{r}\right)} + E_{0}e^{j\left(\omega t-\overline{k_{0}}\cdot\overline{r}\right)}E_{+1}e^{-j\left(\omega t-\overline{k_{+1}}\cdot\overline{r}\right)} + \\
& E_{+1}e^{j\left(\omega t-\overline{k_{+1}}\cdot\overline{r}\right)}E_{-1}e^{-j\left(\omega t-\overline{k_{-1}}\cdot\overline{r}\right)} + E_{+1}e^{j\left(\omega t-\overline{k_{+1}}\cdot\overline{r}\right)}E_{0}e^{-j\left(\omega t-\overline{k_{0}}\cdot\overline{r}\right)} + E_{+1}e^{j\left(\omega t-\overline{k_{+1}}\cdot\overline{r}\right)}E_{+1}e^{-j\left(\omega t-\overline{k_{+1}}\cdot\overline{r}\right)}
\end{aligned}
$$

$$I \sim E_{-1}^2 + E_0^2 + E_{+1}^2 +$$
$$E_0 E_{-1}\left(e^{j\left(\overline{k_0}\cdot\bar{r}-\overline{k_{-1}}\cdot\bar{r}\right)} + e^{-j\left(\overline{k_0}\cdot\bar{r}-\overline{k_{-1}}\cdot\bar{r}\right)}\right) + E_{-1}E_{+1}\left(e^{j\left(\overline{k_{+1}}\cdot\bar{r}-\overline{k_{-1}}\cdot\bar{r}\right)} + e^{-j\left(\overline{k_{+1}}\cdot\bar{r}-\overline{k_{-1}}\cdot\bar{r}\right)}\right) + E_0 E_{+1}\left(e^{j\left(\overline{k_0}\cdot\bar{r}-\overline{k_{+1}}\cdot\bar{r}\right)} + e^{-j\left(\overline{k_0}\cdot\bar{r}-\overline{k_{+1}}\cdot\bar{r}\right)}\right)$$

The intensity is related to the diffracted orders as:

$$I \sim E_{-1}^2 + E_0^2 + E_{+1}^2 + 2E_0E_{-1}\cos\left(\left[\overline{k_0}-\overline{k_{-1}}\right]\cdot\bar{r}\right) + 2E_{-1}E_{+1}\cos\left(\left[\overline{k_{-1}}-\overline{k_{+1}}\right]\cdot\bar{r}\right) + 2E_0E_{+1}\cos\left(\left[\overline{k_0}-\overline{k_{+1}}\right]\cdot\bar{r}\right)$$

Then making use of the relationships between the electric field amplitudes, the intensity simplifies:

$$I \sim \alpha^2E_0^2 + E_0^2 + \alpha^2E_0^2 + 2\alpha E_0^2\cos\left(\left[\overline{k_0}-\overline{k_{-1}}\right]\cdot\bar{r}\right) + 2\alpha^2E_0^2\cos\left(\left[\overline{k_{-1}}-\overline{k_{+1}}\right]\cdot\bar{r}\right) + 2\alpha E_0^2\cos\left(\left[\overline{k_0}-\overline{k_{+1}}\right]\cdot\bar{r}\right)$$

Normalized by the squared electric field amplitude of the zero order, this becomes:

$$\frac{I}{I_0} \sim 1 + 2\alpha\left(\alpha\left[1+\cos\left(\left[\overline{k_{-1}}-\overline{k_{+1}}\right]\cdot\bar{r}\right)\right] + \cos\left(\left[\overline{k_0}-\overline{k_{-1}}\right]\cdot\bar{r}\right) + \cos\left(\left[\overline{k_0}-\overline{k_{+1}}\right]\cdot\bar{r}\right)\right)$$

This can be further simplified by including a coordinate system in which the optical axis is along the z-direction and the m=+1 order diffracts at an angle $\theta$. This causes the dot-products to simplify and highlights which terms in the intensity contribute to specific features of the intensity pattern beyond the phase mask. With a little work, the arguments to the cosines become:

$$\because \sin\theta = -\sin\theta_{-1} = \sin\theta_{+1} \text{ and } \cos\theta = \cos\theta_{-1} = \cos\theta_{+1}$$
$$\overline{k_{-1}}\cdot\bar{r} = kx\sin\theta_{-1} + kz\cos\theta_{-1} = -kx\sin\theta + kz\cos\theta$$
$$\overline{k_0}\cdot\bar{r} = kz$$
$$\overline{k_{+1}}\cdot\bar{r} = kx\sin\theta_{+1} + kz\cos\theta_{+1} = kx\sin\theta + kz\cos\theta$$
$$\left[\overline{k_0}-\overline{k_{-1}}\right]\cdot\bar{r} = x\left[k\sin\theta\right] + z\left[k\left(1-\cos\theta\right)\right] = a(x,z)$$
$$\left[\overline{k_{-1}}-\overline{k_{+1}}\right]\cdot\bar{r} = -x\left[2k\sin\theta\right]$$
$$\left[\overline{k_0}-\overline{k_{+1}}\right]\cdot\bar{r} = -x\left[k\sin\theta\right] + z\left[k\left(1-\cos\theta\right)\right] = b(x,z)$$

Then the normalized intensity becomes:

$$\frac{I}{I_0} \sim 1 + 2\alpha\left(\alpha\left[1+\cos\left(x\left[2k\sin\theta\right]\right)\right] + \cos\left(a(x,z)\right) + \cos\left(b(x,z)\right)\right)$$

Recognizing that

$$\cos(a) + \cos(b) = 2\cos\left(\frac{a+b}{2}\right)\cos\left(\frac{a-b}{2}\right) = 2\cos\left(kz\left(1-\cos\theta\right)\right)\cos\left(kx\sin\theta\right)$$

The normalized intensity becomes:

$$\frac{I}{I_0} \sim 1 + 2\alpha\left(\alpha\left[1+\cos\left(x\left[2k\sin\theta\right]\right)\right] + 2\cos\left(kz\left(1-\cos\theta\right)\right)\cos\left(kx\sin\theta\right)\right)$$

The above equation is simplified if the grating equation is applied: $\sin\theta_m = \frac{m\lambda}{p}$. It is also useful to define $\kappa = \frac{2\pi}{p}$

$$\frac{I}{I_0} \sim 1 + 2\alpha^2 + 2\alpha^2 \cos(2\kappa x) + 4\alpha \cos(\kappa x) \cos\left( kz \left( 1 - \cos\sin^{-1}\left( \frac{\lambda}{p} \right) \right) \right)$$

Notice that the argument to the final cosine is the only term that has a z-dependence.

$$\frac{I}{I_0} \sim 1 + 2\alpha^2 + 2\alpha^2 \cos(2\kappa x) + 4\alpha \cos(\kappa x) \cos\left( kz \left( 1 - \sqrt{1 - \frac{\lambda^2}{p^2}} \right) \right)$$

This term reaches maximum values every half-cycle, i.e.

$$\pi = kz\left( 1 - \sqrt{1 - \frac{\lambda^2}{p^2}} \right) \Rightarrow z = \frac{\lambda}{1 - \sqrt{1 - \frac{\lambda^2}{p^2}}} = \lambda \frac{\left( 1 + \sqrt{1 - \frac{\lambda^2}{p^2}} \right)}{\left( 1 - \sqrt{1 - \frac{\lambda^2}{p^2}} \right)\left( 1 + \sqrt{1 - \frac{\lambda^2}{p^2}} \right)} = \frac{p^2}{\lambda}\left( 1 + \sqrt{1 - \frac{\lambda^2}{p^2}} \right)$$

c. **Membrane stiction to the handle during HF release**

There is a physical reason that membranes when undercut in HF do not release to float away that is grounded in the convective-diffusion equations (see [47] pg 45-48). Wherein the convective derivative of chemical species $C_i$ is related to its laplacian and volume reactions as:

$$\frac{\partial C_i}{\partial t} + \left( \bar{v} \cdot \nabla \right) C_i = D_i \nabla^2 C_i + R^{volume} \tag{16}$$

Also, the chemical flux $\mathbf{J}_i$ of the species is the chemical gradient scaled by the diffusivity:

$$\overline{J_i} = -D_i \nabla C_i \tag{17}$$

In essence the reaction of hydrofluoric acid with the buried oxide is a heterogeneous surface reaction - at the $SiO_2$ surface, the ion flux is governed by the adsorption of reactant, desorption of products and the surface reaction rate (in units of $mol \cdot cm^{-2} \cdot s^{-1}$):

$$\overline{J_i} \cdot \hat{n}\left( \bar{r} \right) + R_{ij}^{surface} = \overline{J_j} \cdot \hat{n}\left( \bar{r} \right) \tag{18}$$

In equations 16, 17 and 1 8, for chemical species 'i', $C_i$ is its concentration in mols, $D_i$ is its diffusivity in $m^2 \cdot s^{-1}$ and $J_i$ is its (diffusive) flux in $mol \cdot cm^{-2} \cdot s^{-1}$. Also, **v** is the velocity of the bulk fluid and n(**r**) is the unit normal pointing from the surface of the $SiO_2$ into the hydrofluoric acid solution.

In [48], the authors describe the etch of $SiO_2$ in hydrofluoric acid as a surface reaction, wherein the hydrogen bifluoride reactant, $C_{HF_2^-}$, adsorbs to the surface of the $SiO_2$ and reacts to release the silicon hexafluoride gaseous species, i.e.

$$SiO_2 + 3HF_2^- + H^+ \xrightarrow[R_{ij}^{surface}]{} SiF_6^{--} + 2H_2O \tag{19}$$

If in equation 19, when $R^{surface}$ becomes zero due to complete removal of $SiO_2$, then silicon hexafluoride stops being produced (and hydrogen bifluoride stops being consumed), so their fluxes from (and to) the surface vanish and thus the left side of equation 17 is zero. Also, for all chemical species in equation 19, the concentrations are no longer are changing in time because no reaction is occurring. Moreover, in regions where the device layer and handle silicon are not in contact, some of the gradients in concentration are negligible because the flux of reactants toward the surface is substantially along the surface normal. Geometrically, only one concentration gradient, along the direction perpendicular to the surface of the handle silicon, will be varying in that direction i.e.,

$$0 = \left(\bar{v} \cdot \nabla\right) C_i = v_x \cancel{\frac{\partial C_i}{\partial x}} + v_y \cancel{\frac{\partial C_i}{\partial y}} + v_z \frac{\partial C_i}{\partial z} \tag{20}$$

With this simple argument it appears that $v_z$, the component of the velocity that would help the membrane separate from the handle must be zero when the reaction concludes.

# Bibliography


[1] E. Yablonovitch, T. J. Gmitter, and K. M. Leung, "Photonic band structure: The face-centered-cubic case employing nonspherical atoms," *Phys. Rev. Lett.*, vol. 67, no. 17, p. 2295, Oct. 1991.

[2] A. Yariv, Y. Xu, R. K. Lee, and A. Scherer, "Coupled-resonator optical waveguide: a proposal and analysis," *Opt. Lett.*, vol. 24, no. 11, pp. 711–713, Jun. 1999.

[3] M. Qi, private communication.

[4] Y. Tanaka, J. Upham, T. Nagashima, T. Sugiya, T. Asano, and S. Noda, "Dynamic control of the Q factor in a photonic crystal nanocavity," *Nat Mater*, vol. 6, no. 11, pp. 862–865, Nov. 2007.

[5] C. C. Cheng, V. Arbet-Engels, A. Scherer, and E. Yablonovitch, "Nanofabricated three dimensional photonic crystals operating at optical wavelengths," *Phys. Scr.*, vol. T68, pp. 17–20, Jan. 1996.

[6] F. García-Santamaría, H. T. Miyazaki, A. Urquía, M. Ibisate, M. Belmonte, N. Shinya, F. Meseguer, and C. López, "Nanorobotic Manipulation of Microspheres for On-Chip Diamond Architectures," *Adv. Mater.*, vol. 14, no. 16, p. 1144, Aug. 2002.

[7] R. Saeidpourazar, R. Li, Y. Li, M. D. Sangid, C. Lu, Y. Huang, J. A. Rogers, and P. M. Ferreira, "Laser-Driven Micro Transfer Placement of Prefabricated Microstructures," *Journal of Microelectromechanical Systems*, vol. 21, no. 5, pp. 1049–1058, 2012.

[8] J. Scrimgeour, D. N. Sharp, C. F. Blanford, O. M. Roche, R. G. Denning, and A. J. Turberfield, "Three-Dimensional Optical Lithography for Photonic Microstructures," *Adv. Mater.*, vol. 18, no. 12, pp. 1557–1560, Jun. 2006.

[9] A. K. Raub and S. R. J. Brueck, "Large area three-dimensional photonic crystals with embedded waveguides," *J. Vac. Sci. Technol. B*, vol. 28, no. 6, p. C6O38, 2010.

[10] A. P. Philipse, "Solid opaline packings of colloidal silica spheres," *J Mater Sci Lett*, vol. 8, no. 12, pp. 1371–1373, Dec. 1989.

[11] A. Blanco, E. Chomski, S. Grabtchak, M. Ibisate, S. John, S. W. Leonard, C. Lopez, F. Meseguer, H. Miguez, J. P. Mondia, G. A. Ozin, O. Toader, and H. M. van Driel, "Large-scale synthesis of a silicon photonic crystal with a complete three-dimensional bandgap near 1.5 micrometres," *Nature*, vol. 405, no. 6785, pp. 437–440, May 2000.

[12] S. A. Rinne, F. Garcia-Santamaria, and P. V. Braun, "Embedded cavities and waveguides in three-dimensional silicon photonic crystals," *Nat Photon*, vol. 2, no. 1, pp. 52–56, Jan. 2008.

[13] E. Palacios-Lidón, J. F. Galisteo-López, B. H. Juárez, and C. López, "Engineered Planar Defects Embedded in Opals," *Adv. Mater.*, vol. 16, no. 4, pp. 341–345, Feb. 2004.

[14] N. Tétreault, A. Mihi, H. Míguez, I. Rodríguez, G. A. Ozin, F. Meseguer, and V. Kitaev, "Dielectric Planar Defects in Colloidal Photonic Crystal Films," *Adv. Mater.*, vol. 16, no. 4, pp. 346–349, Feb. 2004.
[15] J. K. W. Yang, Y. S. Jung, J.-B. Chang, MickiewiczR. A., Alexander-KatzA., RossC. A., and K. K. Berggren, "Complex self-assembled patterns using sparse commensurate templates with locally varying motifs," *Nat Nano*, vol. 5, no. 4, pp. 256–260, Apr. 2010.
[16] C. A. Ross, Y. S. Jung, V. P. Chuang, F. Ilievski, J. K. W. Yang, I. Bita, E. L. Thomas, H. I. Smith, K. K. Berggren, G. J. Vancso, and J. Y. Cheng, "Si-containing block copolymers for self-assembled nanolithography," *J. Vac. Sci. Technol. B*, vol. 26, no. 6, p. 2489, 2008.
[17] M. Qi, E. Lidorikis, P. T. Rakich, S. G. Johnson, J. D. Joannopoulos, E. P. Ippen, and H. I. Smith, "A three-dimensional optical photonic crystal with designed point defects," *Nature*, vol. 429, no. 6991, pp. 538–542, Jun. 2004.
[18] S. Noda, N. Yamamoto, M. Imada, H. Kobayashi, and M. Okano, "Alignment and stacking of semiconductor photonic bandgaps by wafer-fusion," *Lightwave Technology, Journal of*, vol. 17, no. 11, pp. 1948–1955, 1999.
[19] S.-H. Hur, D.-Y. Khang, C. Kocabas, and J. A. Rogers, "Nanotransfer printing by use of noncovalent surface forces: Applications to thin-film transistors that use single-walled carbon nanotube networks and semiconducting polymers," *Applied Physics Letters*, vol. 85, p. 5730, 2004.
[20] A. Murarka, S. Paydavosi, T. Andrew, A. Wang, J. Lang, and V. Bulovic, "Printed MEMS membranes on silicon," in *2012 IEEE 25th International Conference on Micro Electro Mechanical Systems (MEMS)*, 2012, pp. 309–312.
[21] H. Yang, D. Zhao, J.-H. Seo, S. Chuwongin, S. Kim, J. A. Rogers, Z. Ma, and W. Zhou, "Broadband Membrane Reflectors on Glass," *IEEE Photonics Technology Letters*, vol. 24, no. 6, pp. 476–478, 2012.
[22] K. Zhang, J.-H. Seo, W. Zhou, and Z. Ma, "Fast flexible electronics using transferrable silicon nanomembranes," *J. Phys. D: Appl. Phys.*, vol. 45, no. 14, p. 143001, Apr. 2012.
[23] W.-H. Yeo, Y.-S. Kim, J. Lee, A. Ameen, L. Shi, M. Li, S. Wang, R. Ma, S. H. Jin, Z. Kang, Y. Huang, and J. A. Rogers, "Multifunctional Epidermal Electronics Printed Directly Onto the Skin," *Advanced Materials*, vol. 25, no. 20, pp. 2773–2778, 2013.
[24] S. A. Scott and M. G. Lagally, "Elastically strain-sharing nanomembranes: flexible and transferable strained silicon and silicon–germanium alloys," *Journal of Physics D: Applied Physics*, vol. 40, pp. R75–R92, Feb. 2007.
[25] A. A. Patel, "Membrane technology for the fabrication of three-dimensional photonic crystals." [Online]. Available: http://dspace.mit.edu/handle/1721.1/60175. [Accessed: 14-Mar-2011].
[26] E. E. (Euclid E. Moon, "Interferometric-spatial-phase imaging for sub-nanometer three-dimensional positioning," 2004. [Online]. Available: http://dspace.mit.edu/handle/1721.1/34563. [Accessed: 05-Dec-2011].

[27] M. Bruel, "Silicon on insulator material technology," *Electronics Letters*, vol. 31, no. 14, pp. 1201–1202, Jul. 1995.
[28] M. E. (Michael E. Walsh, "On the design of lithographic interferometers and their application." [Online]. Available: http://dspace.mit.edu/handle/1721.1/28741. [Accessed: 04-Apr-2011].
[29] M. L. Schattenburg, "Optically matched trilevel resist process for nanostructure fabrication," *Journal of Vacuum Science & Technology B: Microelectronics and Nanometer Structures*, vol. 13, p. 3007, Nov. 1995.
[30] C. P. Fucetola, H. Korre, and K. K. Berggren, "Low-cost interference lithography," *J. Vac. Sci. Technol. B*, vol. 27, no. 6, p. 2958, 2009.
[31] C. P. Fucetola, A. A. Patel, E. E. Moon, T. B. O'Reilly, and H. I. Smith, "Coherent diffraction lithography: Periodic patterns via mask-based interference lithography," *J. Vac. Sci. Technol. B*, vol. 27, no. 6, p. 2947, 2009.
[32] H. F. Talbot, "LXXVI. Facts relating to optical science. No. IV," *Philosophical Magazine Series 3*, vol. 9, pp. 401–407, Dec. 1836.
[33] E. E. Moon, L. Chen, P. N. Everett, M. K. Mondol, and H. I. Smith, "Interferometric-spatial-phase imaging for six-axis mask control," *Journal of Vacuum Science & Technology B: Microelectronics and Nanometer Structures*, vol. 21, no. 6, p. 3112, 2003.
[34] L. Lu, L. L. Cheong, H. I. Smith, S. G. Johnson, J. D. Joannopoulos, and M. Solja?i?, "Three-dimensional photonic crystals by large-area membrane stacking," *Opt. Lett.*, vol. 37, no. 22, pp. 4726–4728, Nov. 2012.
[35] E. Anderson, L. Peekskill, H. I. Smith, and M. L. Schartenburg, "Holographic Lithography," 5 142 385,25-Aug-1992.
[36] J. Hermanowski, "Thin wafer handling - Study of temporary wafer bonding materials and processes," in *IEEE International Conference on 3D System Integration, 2009. 3DIC 2009*, 2009, pp. 1–5.
[37] Ranjith John, "Low Cost, Room Temperature Debondable Spin on Temporary Bonding Solution: A Key Enabler for 2.5D/3D IC Packaging," May-2013.
[38] X. G. Zhang, *Electrochemistry of Silicon and its Oxide*. Springer, 2001.
[39] K. Hermansson, U. Lindberg, B. Hok, and G. Palmskog, "Wetting properties of silicon surfaces," in , *1991 International Conference on Solid-State Sensors and Actuators, 1991. Digest of Technical Papers, TRANSDUCERS '91*, 1991, pp. 193–196.
[40] C. W. Extrand and S. I. Moon, "Critical Meniscus Height of Liquids at the Circular Edge of Cylindrical Rods and Disks," *Langmuir*, vol. 25, no. 2, pp. 992–996, Jan. 2009.
[41] T. I. Hesla and D. D. Joseph, "The maximum contact angle at the rim of a heavy floating disk," *Journal of Colloid and Interface Science*, vol. 279, no. 1, pp. 186–191, Nov. 2004.
[42] Rayleigh, "Interference Bands and their Applications," *Nature*, vol. 48, no. 1235, pp. 212–214, Jun. 1893.
[43] A. Çolak, H. Wormeester, H. J. W. Zandvliet, and B. Poelsema, "Surface adhesion and its dependence on surface roughness and humidity measured with a flat tip," *Applied Surface Science*, vol. 258, no. 18, pp. 6938–6942, Jul. 2012.

[44] J. Theurich, D. W. Bahnemann, R. Vogel, F. E. Ehamed, G. Alhakimi, and I. Rajab, "Photocatalytic degradation of naphthalene and anthracene: GC-MS analysis of the degradation pathway," *Res. Chem. Intermed.*, vol. 23, no. 3, pp. 247–274, Mar. 1997.
[45] Y. Matsumoto, H. Koinuma, and T. Ohsawa, "Photodecomposition of Pentacene Films on Atomically Controlled SrTiO3(001) Surfaces," *J. Phys. Chem. C*, vol. 111, no. 28, pp. 10523–10527, Jul. 2007.
[46] V. Oja and E. M. Suuberg, "Vapor Pressures and Enthalpies of Sublimation of Polycyclic Aromatic Hydrocarbons and Their Derivatives," *J. Chem. Eng. Data*, vol. 43, no. 3, pp. 486–492, May 1998.
[47] W. M. Deen, *Analysis of transport phenomena*. New York, NY [u.a.]: Oxford Univ. Press, 1998.
[48] H. Kikyuama, N. Miki, K. Saka, J. Takano, I. Kawanabe, M. Miyashita, and T. Ohmi, "Principles of wet chemical processing in ULSI microfabrication," *IEEE Transactions on Semiconductor Manufacturing*, vol. 4, no. 1, pp. 26–35, Feb. 1991.